Ph. D. DISSERTATION

Structural and Electrical Properties of Low-*k* SiOC(-H) Thin Films Deposited by Using Plasma-Enhanced Chemical-Vapor Deposition

Department of Physics

Graduate School

Jeju National University

Chang Young Kim

February 2011

PECVD 方法에 의해 蒸着된 Low-k SiOC(-H) 薄膜의 構造的 및 電氣的 特性

指導敎授 崔 致 圭

金 昶 英

이 論文을 理學 博士學位 論文으로 提出함

2010 年 12 月

金昶英의 理學 博士學位 論文을 認准함

審査委員長 _____

委 員 _____

委 員 _____

委 員 _____

委 員 _____

濟州大學校 大學院

2010 年 12 月

Structural and Electrical Properties of Low-*k* SiOC(-H) Thin Films Deposited by Using Plasma-Enhanced Chemical-Vapor Deposition

Chang Young Kim

(Supervised by Professor Chi Kyu Choi)

A thesis submitted in partial fulfillment of the requirement for the degree of Doctor of Science.

2010. 12.

This thesis has been examined and approved.

_____

_____

_____

_____

_____

_____

Date

Department of Physics

GRADUATE SCHOOL

JEJU NATIONAL UNIVERSITY

Table of Content

List of Tables

List of Figures

ABSTRACT

In this work, the focus is on the exploration of the bonding structure, the mechanical and electrical properties of SiOC(-H) thin films deposited by using plasma-enhanced chemical-vapor deposition (PECVD) with dimethyl-dimethoxy-silane (DMDMS, $C_4H_{12}O_2Si$) and oxygen gas as various deposition conditions. Then, we investigate the electro-physical properties, such as the charge trapping behavior, Cu atom diffusion phenomena and the electrical conduction mechanism after the application of an electric bias stress to the Cu(Al)/SiOC(-H)/*p*-Si(100) metal-insulator-semiconductor (MIS) structures. In order to obtain the optimum conditions for the bulk plasma, we investigated the electron density (N_e), electron temperature (T_e) and various emission species. As the radio frequency (rf) power was increased from 100 to 800 W, the corresponding N_e and T_e were found to increase from 6.23×10^{8} to 1.22×10^{10} cm^{-3} and from 1.57 to 2.03 eV, respectively. A complete dissociation of precursors took place for rf power greater than 500 W, in our PECVD system.

The Fourier transform infrared (FTIR) spectra of all samples were generally broad and overlapping due to the complex stoichiometry and the amorphous nature of the films. The characteristic band of all the SiOC(-H) films showed absorption bands due to Si-O-Si (around 1055 cm^{-1}), Si-O-C (around 1055 cm^{-1}), $Si-CH_3$ (around 950 and 1250 cm^{-1}), CH_n (1457 and 2955 cm^{-1}) and -OH (around 3200 to 3700 cm^{-1}) in addition to those of the Si substrate. There is a shoulder at 1150 cm^{-1} in all the absorption spectra, assigned to the broad Si-O-C peak corresponding to the Si-O-C cage-link structure and resulting in a more porous nature in the SiOC(-H) film. But the SiOC(-H) thin films deposited with a higher substrate temperature than 300 °C is attributed to the lower carbon concentration due to the $Si-CH_3$ bonds being broken at elevated substrate temperatures that give rise to the increase of dielectric constant.

X-ray photoelectron spectroscopy (XPS) narrow scan spectra of the SiOC(-H) films,

which are associated with the Si 2p electron orbital, consisted of four or five peaks, which could be assigned to the Si-C (99.4±0.1 eV), O-Si-$(CH_3)_3$ (100.4±0.1 eV), O_2-Si-$(CH_3)_2$ (101.6±0.1 eV), O_3-Si-CH_3 (102.8±0.1 eV) and Si-O_2 (103.6 eV) bonds. As the flow rate and the rf power were increased, the Si 2p electron orbital spectra shifted to a lower binding energy while the C 1s and the O 1s electron orbital remained almost constant. The C 1s electron orbital spectra of the SiOC(-H) films consisted of six peaks, which could be assigned as $C(Si)_4$ (282.5±0.1 eV), Si-C (283.4±0.1 eV), C=C (283.9±0.1 eV), C-C/C-H (284.6±0.1 eV), C-O (285.4±0.1 eV) and C=O (286.7±0.1 eV) bonds. Also the O 1s spectra consisted of four components, which were attributed to the O-C (530.5±0.1 eV), SiC_xO_y (531.8±0.1 eV), O-Si (532.6±0.1 eV) and O-Si-O (533.7±0.1 eV) bonds. The peak intensities of the Si 2p and the O 1s spectra decreased with increasing flow rate ratio and rf power whereas the intensity of the C 1s spectrum increased. However, the peak intensities of the O_2-Si-$(CH_3)_2$ and O_3-Si-CH_3 bonds of the SiOC(-H) films were increased, in case of the SiOC(-H) films deposited at a higher substrate temperature.

As-deposited MIS structures showed the two kinds of mechanism: namely, Schottky emission (SE) for midrange electric fields (0.5 to 2.25 MV/cm) and the Poole-Frenkel (PF) emission at higher electric fields (beyond 2.25 MV/cm). In contrast, the annealed MIS structures showed only SE. The Schottky barrier height decreased from 0.326 eV for the as-deposited MIS structures and to 0.145 eV for the MIS structures annealed at 450 °C. The PF barrier height for the as-deposited Cu/SiOC(-H)/*p*-Si(100) MIS structure was calculated as 0.365 eV. All samples showed a voltage breakdown after annealing at 500 °C. Also the leakage current density was found to be 3.7×10^{-9} A/cm^2 and the lowest dielectric constant of 2.21 was obtained for the SiOC(-H) films deposited with a flow rate ratio of 80% at an rf power of 700 W.

Interface charges gradually increased with both increasing annealing temperature and stressing duration. The excessive radicals such as -CH_3 or Si-CH_3 and Si-H bonds in the SiOC(-H) film showed up in more positive charges in the form of

excessive $(-CH_3)^+$ or $(Si-CH_3)^+$ and $(Si-H)^+$ ions, and interstitial defects, attributed to the flat-band voltage (V_{fb}) appear on the negative side. The drift rate of Cu^+ ions in the SiOC(-H) films with the MIS structures after annealing was evaluated by capacitance-voltage (C-V) measurements with a flat-band shift caused by a bias-temperature stress (BTS). The V_{fb} and the activation energies (E_a) corresponding to the MIS structures annealed at 250, 350 and 450 °C with a BTS time of 40 min were -15, -18 and -34 V, and 0.58, 0.26 and 0.22 eV, respectively. The flat-band voltage (V_{fb}) of the C-V curve revealed a shift due to Cu^+ ion diffusion in the SiOC(-H) layer. The series resistance (R_s) of the MIS structure strongly depended on the applied voltage for frequencies less than 50 kHz. Also, at high frequencies ($f \geq$ 100 kHz), charges at the interface states could not follow an alternating current (ac) signal. The dielectric constant (ϵ') decreased with increasing frequency whereas the dielectric loss (ϵ'') showed the trend opposite to that of ϵ'. The values of ϵ' and ϵ'' were calculated to be 2.68 and 0.07, respectively at 1 kHz. The ac electrical conductivity increased with increasing frequency.

In our study, the SiOC(-H) film deposited by using plasma-enhanced chemical-vapor deposition (PECVD) with dimethyl-dimethoxy-silane (DMDMS, $C_4H_{12}O_2Si$) and oxygen gas at an rf power of 700 W. The SiOC(-H) films produced had a cross-linked structure with nano-pores due to the combined $Si-CH_n-Si$ bond and Si-O-Si network, in which the $Si-CH_n-Si$ bond is formed due to the incorporation of $-CH_n$ groups into the Si-O-Si network. We have defined the difference in the C-V characteristics that might be caused by the positive charge carrier due to chemical bonds, such as $-CH_3$ or $Si-CH_3$ and Si-H, incorporated into the SiOC(-H) film with an annealing process. On the other hand, the decrease in inversion capacitance might be caused by the diffusion of Cu atoms, which can produce a deep donor level of 0.49 eV above the valence bond. Therefore, it is important to develop an effective diffusion barrier between the SiOC(–H) film and Cu to prevent Cu diffusion.

Chapter Ⅰ. Introduction

1. Interconnect delays & low-*k* materials

Modern computer microprocessor chips are marvels of engineering complexity. For the current 45 nm technology node, there may be nearly a billion transistors on a chip barely 1 cm^2 and more than 10,000 m of wiring connecting and powering these devices distributed over 9-10 wiring levels. Ongoing miniaturization is essential for enhancing the speed of ultra large-scale integration (ULSI) technology. However, reducing the distance between the wiring increases their capacitance, resulting in signal propagation delay. RC delay performance and RC delay circuit diagrams are shown below in Fig. 1 [1].

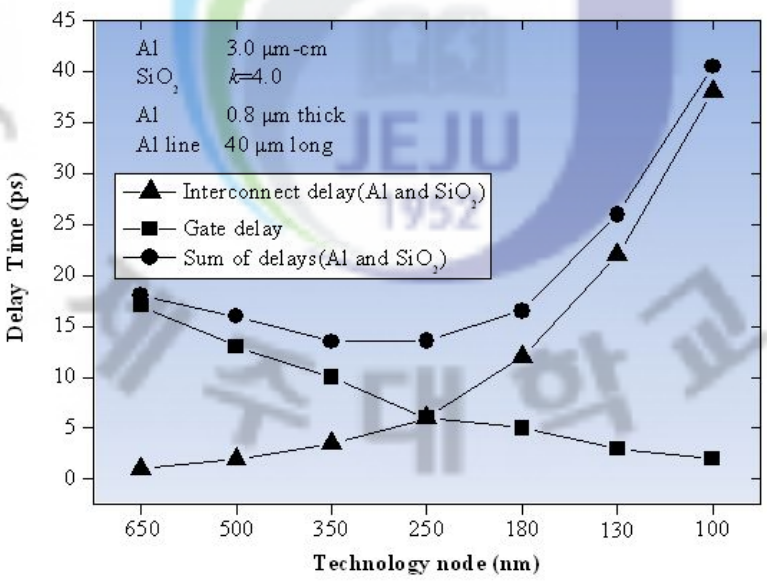

Fig. 1. Calculated gate and interconnect delay as a function of technology node cording to the National Technology Roadmap for Semiconductors (NTRS) in 1997.

Such reduced feature size has contributed adversely to the interconnect delay which is given by [2]:

$$RC \cong 2\rho k\epsilon_0\left(\frac{4L^2}{p^2}\frac{L^2}{T^2}\right) \quad (1)$$

where ρ is the metal resistivity, ϵ_0 is the vacuum permittivity, k is the relative dielectric constant of interlayer dielectric (ILD), p is the metal line pitch (sum of line width and line spacing), T is the metal thickness and L is the metal line length. This equation demonstrates that RC delay can be reduced using metals with low resistivity and dielectric materials with a low dielectric constant.

To solve this problem, low resistivity Cu metallization and low dielectric constant materials (k < 2.5) are used to replace the conventional Al/SiO_2 interconnect structure [3 - 5]. Cu has become the metal of choice for interconnects in ULSI owing to its inherent low resistance. Table 1 shows material properties of selected metals for application to interconnects [6]. The low resistivity of Cu metal compared to Al metal helps reduce the resistance and capacitance of an RC delay. Many research groups are being involved in the development of a suitable low-k material. Both spin-on and plasma enhanced chemical vapor deposition are being widely used to prepare potential candidates for low-k materials. Although a large variety of hybrid materials have been prepared, few structural characterizations have been reported so far [7-12].

Silicon dioxide (SiO_2) has been the most widely used dielectric material in the semiconductor industry. It has good thermal and mechanical properties, but too high a dielectric constant (3.9~4.5) for the future generation of integrated circuits (IC's). Initial attempts to decrease the dielectric constant of SiO_2 involved the incorporation of the fluorine or the carbon to the oxide films, and also the use of spin-on glasses or silsesquioxanes, which are similar in nature to SiO_2, but with lower dielectric constants due to the non-bridging silicon-carbon bonds in the backbone. The Si-C

bonds lower the density of the films by introducing free volume, and also exhibit lower polarizability with respect to the Si-O bonds in silicon dioxide. Over the years, a wide variety of materials have been tested for low dielectric constant applications and Table 2 summarizes some of these, along with their respective *k* values and deposition method [13-15]. The most promising among these materials are the organic polymers and the porous materials because of their lower dielectric constant. However, as stated previously, the ideal thin film dielectric material not only needs to have a low dielectric constant, but also a series of electrical, mechanical, and thermal properties required for its application into microelectronic devices.

The failure to meet one or several of these requirements has limited the use of some materials, such as Teflon AF (DuPont). This amorphous copolymer of tetrafluoriethylene (TFE) and 2,2-bis(trifluoromethyl)-4,5-difluoro dioxide has a very low dielectric constant (k=2.1), but lacks thermo-mechanical stability as it has low glass transition (T_g<300 °C) and decomposition temperatures (~360 °C) [16,17]. It also shows poor adhesion to metals.

Other organic polymers like the polymides [18,19] tend to have low dielectric constants in the range of 2.9~3.5, good mechanical properties, and planarizing capabilites. However, some types of polymides have high moisture absorption (which raises the dielectric constant), and are extremely anisotropic with high in-plane dielectric constants. Fluorinated polyimides have lower dielectric constant, higher glass transition temperature (T_g) and improved moisture resistance over the nonfluorinated ones, but they show poor adhesion and out gassing of the fluorine species is possible at elevated temperatures. Benzocylcobutenes (Dow Chemical) [18,19] are themosetting polymers that have good spin-on planarization characteristic and low moisture absorption (<0.2 wt.% at 85% relative humidity). Their low dielectric constant (k~2.6) is the result of a chemical structure that combines relatively non-polarizable aliphatic rings with aromatic rings. However, the main disadvantage with these materials is a limited thermal stability when exposed to temperatures of 150~300 °C in the presence of air, and a high coefficient of thermal expansion

(CTE=52 ppm/°C) [20]. They decompose at temperatures above 350 °C.

Polyarylene ethers [21,22] are another type of organic polymers being considered for low-*k* applications. FLARE^{TM} (Honeywell) is the commercial name for one of such polymers, and one of its formulations has shown a dielectric constant with as low a value as 2.38. This dielectric constant is isotropic and stable during thermal cycling to 450 °C. The material exhibits comparable thermal stability to polymides, but with lower moisture absorption. It also shows good mechanical stability and solvent resistance, but major concerns include adhesion and outgassing of fluorine species during subsequent processing, which can compromise the dielectric constant.

Among the most recent materials being rested for integration into IC manufaturing are SiLK (Dow Chemical) and Black Diamond (Applied Materials). SiLK is an aromatized and cross-linked polyphenylene spin-on material with a dielectric constant of 2.65, and thermal stability in excess of 450 °C [23]. It also has good adhesion to typical metals and barrier layers used in microelectronic processing, and a high glass transition temperature (T_g>490 °C). Continuing effort by IBM have demonstrated successful integration of SiLK into copper-based chips [24], making this the first report of an organic dielectric material used in IC fabrication. On the other hand, Black Diamond is a plasma-enhanced chemical-vapor deposited material with the nature of carbon-dopes silicon dioxide. It has a dielectric constant of 2.7, good thermal stability, and can withstand the stresses applied during Chemical Mechanical Polishing (CMP) processing without delaminating from the substrate [21,25]. However, etching the material without leaving residues on the sidewalls has presented some difficulties for its application.

Increasing attention has focused on the use of porous materials as interlevel dielectrics because no fully-densified material cam compare to the ultra low-*k* values obtained when air (porosity) is added to the films.

The feasibility of the porous dielectrics approach was originally demonstrated with porous silica. These materials consisted of a silicon dioxide network with a high fraction of small pores with diameters in the nanometer range [26]. The typical

preparation procedure for porous silica involves spin-coating a precursor (e.g. tetraethoxysilane) in a solvent onto the substrate, followed by gelation of the silica network under controlled conditions of temperature, pH and catalyst (acid/base) concentration [27,28]. After the gelation process, subsequent aging drying and annealing steps are necessary to move the remaining solvent and the water produced is required because the large amounts of liquid that need to be removed can lead to shrinkage and can cause high internal stress levels and cracking in the films. Porous silica has been subdivided into two classes depending on the preparation procedure and the resultant porosity. Aerogels are the materials with the highest porosity (up to 98%), attained only by supercritical drying under high pressure. The xerogels, on the other hand, show a significantly lower degree of porosity (50~90%), but are prepared using conventional solvents under moderate conditions [29]. The dielectric constant of these films has been measured in the range of 1.1~2.5 depending on the degree of porosity. Nanoglass (Honewell) is the commercial name of a spin-on nanoporous silica product, and it has a dielectric constant of 2.0 with a porosity of 70% [30].

Aerogels and xrogels (porous silica) offer advantages over other dielectric materials that induced high thermal stability, and lower dielectric constant due to variable porosity. However, the use of porous silica in microelectronic applications has been limited due to difficulties in obtaining homogeneous and reproducible pore microstructures, and also because of high moisture absorption and low mechanical strength consideration [26,31]. Jin et al. [26] and Cho et al. [32] have reported on chemical modification techniques used to reduce the surface hydroxyl (OH) groups, and therefore, the moisture uptake of the porous silica films.

A more recently developed porous material is Dow Corning XLK dielectric material [33,34]. These films are deposited via a spin on process, and the chemical formulation contains hydrogen silsesquioxane (HSQ) resin, a high boiling point solvent, and a low boiling point solvent. The preparation procedure includes a gelation reaction in the presence of the high boiling point solvent, and low boiling point solvent. The gelation process involves a controlled exposure to a wet ammonia

treatment. Therefore, analogous to the previous porous silica films, the XLK films also require a complex preparation procedure. The cured films have a dielectric constant of 2.19, and a porosity of 59.5% that is completely interconnected through the film (as determined from small angle neutron scattering). One of the major difficulties with these films is moving the solvents without collapsing the .Hydrogen silsesquioxane (HSQ) resin structure in the process.

In a similar study, A. Gill et al. [35] developed a SiOCH films using a tetramethlylcyclotetrasiloxane (TMCTS) organic materials by PECVD methode The cured films have a dielectric constant of 2.05, and a porosity of 29% that is completely interconnected through the film. The entire range of SiOCH films, with k=2.8~2.05, is characterized by low leakage currents of about 10^{-9} A/cm^2 at 1 MV/cm and relatively low coefficients of thermal expansion of about 12×10^{-6}/K. The hardness and elastic modulus of the material decrease with dielectric constant.

Even though the reduction in the dielectric constant of the insulating material is a major step forward in the development of he next generation of interconnects, there are numerous technical issues to be addressed regarding the use of porous materials as dielectric layer for microelectronic applications. Many issues deal with pore size and distribution, and control over the pore parameters, but other factors like the feasibility or the complexity of process are also major concerns, especially when the reproducibility in high volume manufacturing is at stake. Most of the previously described porous dielectrics suffer from one or several of these issues.

To assure proper device operation, a porous dielectric film would need to have a homogeneous pore distribution with size that are 10~20 precent or less of the smallest feature size [23,24]. In terms of the processing conditions, this would require tight control over the pore size and have a narrow size distribution. The pore interconnectivity is a critical material parameter that affects the electrical and mechanical parameter of the film. Large and open pores make the thin film more susceptible to metal diffusion that could adversely, as well as the adhesion to the interface. When the loading of pore generator is too high, large and interconnected

pores may obtained, resulting in high leakage current and poor mechanical strength. Clearly, the quantitative characterization and understanding of pore size and interconnectivity is important for optimizing the design of porous materials for low-*k* dielectric applications. With these limitations, the nature of the pores becomes a major concern in the development of porous materials. However, the major problem with Cu metallization is its high diffusivity in silicon, silicon dioxides and other dielectrics used in integrated circuits. Therefore, it is important to develop an effective diffusion barrier between the SiOC(–H) film and Cu to prevent Cu diffusion. Ideally, the diffusion barrier should be electronically transparent with a negligibly small voltage drop across it. At the same time, characterization of the interface states in the metal-insulator-semiconductor (MIS) structure has been the subject of intense research over the last decade, and there are a number of reports on various characterization techniques [36,37].

Table 1. Material properties of selected metals for application to interconnects.

	Ag	Cu	Au	Al
Resistivity (Ω)	1.59	1.67	2.35	2.66
Modulus (GPa)	82	65	10	2.7
Thermal conductivity (W/m k)	4.25	7～8	1.5～2.5	0.1～0.3
Melting point (℃)	962	80～160	65	45
Activation energy (eV)	2.01	2.19	1.96	1.48

Table 2. Typical low-*k* materials.

Deposition methode	Type of materials		Dielectric constant	Company
CVD	Inorganic	Air gap	< 2.0	
		SiOF	3.1～3.5	
		BN	2.6～3.0	
	Organic	SiOC(-H)	2.1	IBM[a]
		Coral	<2.4	Novellus
		a-C:F	2.1～2.5	
		Black Diamond	2.6～3.0	Applied materials
		Coral	2.6～3.0	Novellus systems
Spin on	Inorganic SOG	Nanoglass E	2.2	Allied Signal
		HPS	2.6～3.0	CCIC[b]
		FOX	2.6～3.0	Daw corning
	Organic SOG	ST-F2000	2.1～2.5	Hitachi chemical
		Type-9	2.6～3.0	TOK[c]
		T-18	2.6～3.0	Allied Signal
	Organic	*p*-Silk	2.1	Daw chemical
		XLK	2.2	Daw corning
		SilK	2.65	Daw chemical
		Cyclotene	2.6～3.0	Daw chemical

[a] International Business Machines Corporation, [b] Catalysts & Chemicals Industrial Corporation, [c] Tokyo Ohka Kogyo Corporation

2. Research objectives

In the last few years, there has been increasing research activity focused on low dielectric constant (low-*k*) materials due to their potential use in the microelectronics industry [4,7,38]. With decreasing feature size, the signal delay and noise also increase due to capacitive coupling and cross-talk noise between the metal interconnections. One way to tackle these problems is to introduce higher performance interlayer dielectric (ILD) coatings. Thus, low-*k* dielectric materials are becoming important in IC technology, especially for the fabrication of dynamic random access memories (DRAM). Some of the potential candidate materials to be used as an ILD are organic and inorganic precursors such as hydrogensilsequioxane (HSQ), silsesquioxane (SSQ), methylsilsisequioxane (MSQ) and carbon doped silicon oxide (SiOCH) [39,40,42,43], as shown in Table 2 and Fig. 2. Among these, SiOC(-H) films are widely preferred by the semiconductor industry because of their excellent properties. It has been shown that organic functional groups can dramatically decrease dielectric constant by increasing the free volume of films [44]. The incorporation of doping elements such as carbon and hydrogen can be found to play a crucial role in lowering the value of the dielectric constant of the film. In fact, the ability of these elements to modify the local structure of the silicon oxide network gives rise to a lower density material. In other words, the replacement of Si-O bonds with Si-CH_3 (methyl group) bonds causes bulk porosity due to the formation of nano-sized voids within the silicon oxide matrix [8,45]. The SiOC(-H) films can be fabricated by the use of plasma polymerization in an inexpensive way that results in homogeneous, highly cross-linked and thermally stable films for interconnect applications. However, the influence of -CH_3 groups in the SiOC(-H) film and the electrical properties of the interface between SiOC(-H) film and a Si substrate are not known with certainty. Therefore, the objective of this dissertation is to investigate the structural and electrical properties of low-*k* SiOC(-H) thin films

deposited with various deposition conditions by the use of DMDMS and oxygen as precursors.

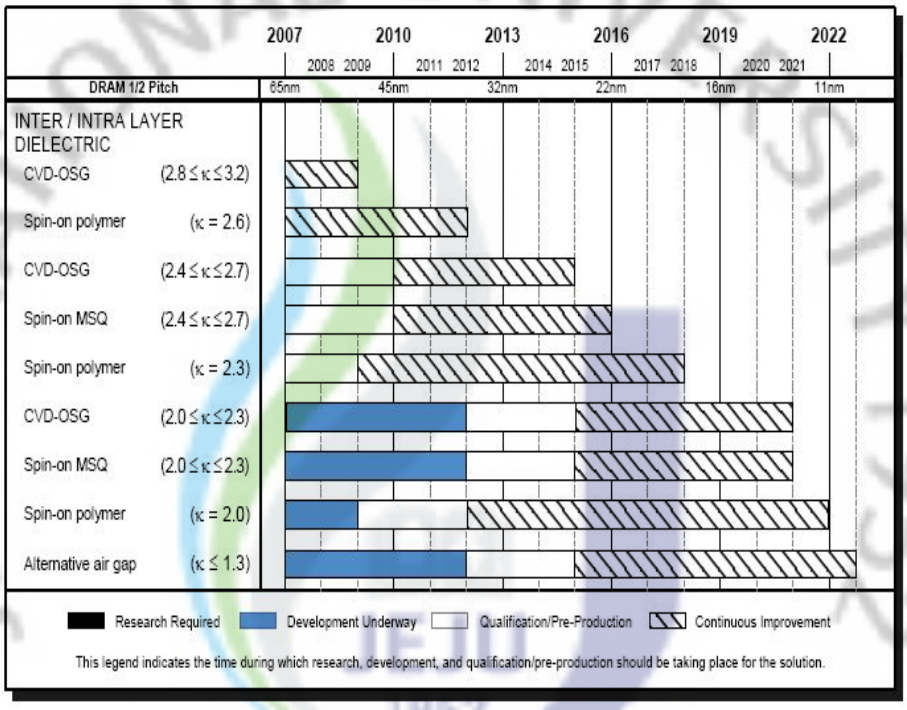

Fig. 2. Dielectric potential solutions (ITRS 2007)

3. Outline of the dissertation

This dissertation is consists of eight chapters. Chapter 1 introduces interconnect delays and low-*k* materials. In Chapter 2, the theoretical background for the analysis of SiOC(-H)/*p*-Si(100) interfaces, dielectric constant and SiOC(-H)/*p*-Si(100) interface charge is presented. The conduction mechanism and models for Cu/low-*k* interconnection are also discussed.

After the introduction and background of the dissertation, the structural and electrical properties of low-*k* SiOC(-H) films will be presented. Chapter 3 explains the experiments and analyses method in this study.

In Chapter 4, 5, 6, 7 the results of these experiments are discussed. Chapter 4 is divided into 3 part. The first section of chapter 4 concerns the in-situ plasma characteristics such as electron density (N_e), electron temperature (T_e) and various emission species during deposition of the SiOC(-H) thin films from DMDMS ($C_4H_{12}O_2Si$) and oxygen as precursors by using plasma enhanced chemical vapor deposition. Also, the influence of the rf power on the structural and the electrical properties of the SiOC(-H) films will be explained. The second part contains a presentation of the structural and the electrical properties of the SiOC(-H) films prepared with DMDMS and oxygen as precursors. The effect of the flow rate ratio on the structural and electrical properties of the films is studied systematically. The third section of chapter 4 contains an explanation of the deposition and structural characterization of low-*k* SiOC(-H) thin films deposited with different substrate temperature by the use of DMDMS and oxygen as precursors. In chapter 5, mechanical properties of the SiOC(-H) film will be explained.

Chapter 6 is also divided into 3 parts. Charge trapping of SiOC(-H)/Si interface will be studied in the first section of chapter 6. The second session of chapter 6 shows Cu atom diffusion and interfacial parameters in as-deposited and annealed Cu/SiOC(-H)/*p*-Si(100)/Al MIS structures under a BTS treatment carried out for

different time durations. In the third section of chapter 6, the electrical conduction mechanisms of Cu/SiOC(-H)/*p*-Si(100) metal-insulator-semiconductor (MIS) structures were investigated using their temperature dependent current-voltage (I-V) characteristics. Also a method to solve these problems will be discussed. Frequency dependent C-V and G/ω-V characteristics of low-dielectric constant SiOC(-H) thin films will be explained in chapter 7. In chapter 8, conclusions will be presented concerning the experimental results of this study.

Chapter Ⅱ. Background Theories

1. Dielectric constant

1) Capacitance and relative permittivity

The relative permittivity (relative dielectric constant) ϵ_r of a medium is defined as the ratio of the capacitances of a capacitor with and without the dielectric in place. The capacitance is described by its charge density σ and plate area A in Fig. 3 [38]. The charge density σ and the magnitude of the applied field E are related as

$$E = \sigma / \epsilon. \tag{2}$$

The charge on the plates arises from the polarizing medium which induces a net charge density p. The electric field between the plates can be written as

$$E = (\sigma - p)/\epsilon_0. \tag{3}$$

Since the electric field in both these equations is the same one obtains

$$p = (\frac{\epsilon - \epsilon_0}{\epsilon})\sigma = (\epsilon_r - 1)\epsilon_0 E. \tag{4}$$

The electric susceptibility χ_e is defined as

$$\chi_e = \epsilon_r - 1, \tag{5}$$

and writing the polarization and electric field as vectors, one obtains

$$\vec{P} = \chi_e \epsilon_0 \vec{E}. \tag{6}$$

The next stage is relating the polarization of the medium, $\vec{P}$, to the polarizability of its molecules. The polarization is the dipole-moment density and equals the mean dipole moment of a molecule, $\vec{p}$, in the medium, multiplied by the number density of molecules N.

The induced dipole moment is proportional to the local electric field $\vec{E}^*$. The local electric field is the total field arising from the applied field and the electric dipoles which that field stimulates in the medium. The polarization of the medium becomes

$$\vec{P} = N\vec{p} = \alpha N \vec{E}^* \tag{7}$$

with α the polarization constant (see next section).

For a continuous dielectric, the Lorentz local field can be derived from electrostatics and is given by

$$\vec{E}^* = \vec{E} + \vec{P}/3\epsilon_0. \tag{8}$$

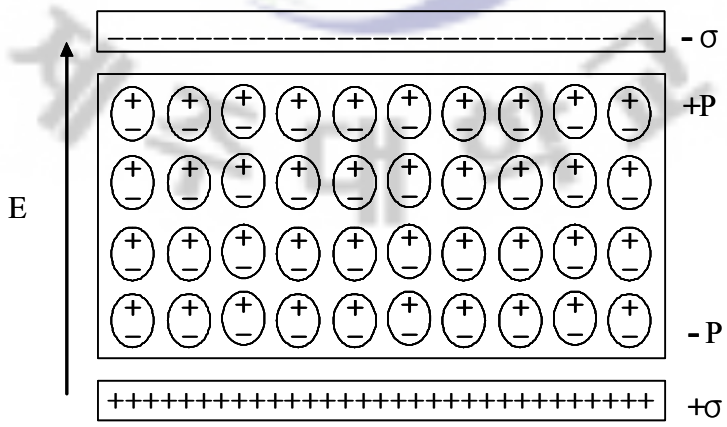

Fig. 3. Schematic cross section of two capacitor plates with surface charge density.

2) Polarization phenomena

The polarizability of a molecule is a measure of its ability to respond to an electric field and acquire an electric dipole moment $\vec{p}$. There are several microscopic mechanisms of polarization in a dielectric material [46]. Electric dipole moments can be induced by the electric field or can be permanent.

The *induced electric dipole moment* can be a result of two polarization phenomena, i.e., electronic polarization and distortion polarization.

Electronic polarization, α_e, describes the displacement of the cloud of bound electrons with reference to the nucleus under an applied electric field. The atom distorts and the center of the atom's negative charge no longer coincides with the position of the nucleus, resulting in an electric dipole moment. The electric dipole moment of each atom is described by

$$\vec{p} = \alpha_e \vec{E}^{*}. \tag{9}$$

Distortion polarization α_d (also often referred to as ionic polarization) relates to the distortion of the position of the nuclei by the applied field, thereby stretching or compressing the bond length, depending on the relative orientation between the ionic bond and the electric field. The molecule is bent and stretched by the applied field and its dipole moment changes accordingly. Nonpolar molecules may acquire an induced dipole moment in an electric field on account of the distortion the field causes in their electronic distributions and nuclear positions. A polar molecule is a molecule with a permanent electric dipole moment. The permanent dipole moment is a result of the partial charges on the atoms in the molecule that arise from the different electronegativity or other features of bonding. Polar molecules may have their existing dipole moments modified by the applied field. Orientation polarization relates to the phenomenon of a permanent dipole moment as a result of polar molecules. The total polarization of a medium, composed of polarizable polar

molecules, is therefore

$$\vec{P} = N(\alpha_e + \alpha_d + \frac{\mu^2}{3kT})\vec{E}^*, \tag{10}$$

with N the number of molecules per m^3, μ the orientation polarizability, k the Boltzmann constant, and T the temperature in K.

The terms α_e and α_d represent the electronic and distortion polarization in the molecule, while the term $\mu^2/3kT$ stems from the thermal averaging of permanent electric dipole moments in the presence of an applied field.

The quantitative relation between the relative permittivity and properties of the molecules is described by the Debye equation

$$\frac{\epsilon_r + 1}{\epsilon_r + 2} = \frac{N}{3\epsilon_0}(\alpha_e + \alpha_d + \frac{\mu^2}{3kT}). \tag{11}$$

The ϵ_r of materials is high if its molecules are polar and highly polarizable. This equation shows that the permittivity is smaller if materials do not contain polar molecules. Reduction of density N and polarizabilities α_e and α_d are also possible ways to decrease the dielectric constant. Reducing the number of ionic bonds in the material minimizes distortion polarization. The electronic polarization is minimized by lowering the electron density in the material, i.e., introducing smaller elements.

The same expression, but without the permanent dipole moment contribution, is called the Clausius–Mossotti equation

$$\frac{\epsilon_r - 1}{\epsilon_r + 2} = \frac{N}{3\epsilon_0}(\alpha_e + \alpha_d). \tag{12}$$

Although the value of the electric dipole moment is extremely important for

predicting properties of dielectric materials, their calculation is difficult. In the case of simple molecules the Stark effect is used to measure the electric dipole moment of molecules for which rotational spectra can be observed. In the case of more complicated systems, the polarizability and permanent dipole moment of molecules can be determined by measuring ϵ_r at a series of temperatures. These measurements facilitate the determination of molar polarizations and their slope and intersect versus $\frac{1}{T}$ give values of dipole moment and polarizability.

3) Film density and relative permittivity

The possibility to lower the molecular polarizability is limited. Equations (10)-(12) show that number of molecules per unit of volume (film density) plays an important role in reduction of the film permittivity. The effect of the density on the film permittivity is stronger that the effect of molecular polarizability since reducing density allows to reduce the dielectric constant to the extreme value close to unity.

Technologically, an important way to reduce the film density is introduction of pores. Generally, porous films can be considered as two-component materials where the solid skeleton has a dielectric constant close to the dense prototype and the second component (pores) has dielectric constant equal to 1. The relative permittivity of porous film ϵ_r directly depends on porosity

$$\frac{\varepsilon_r - 1}{\varepsilon_r + 2} = P\frac{(\varepsilon_1 - 1)}{(\varepsilon_1 + 2)} + (1-P)\frac{(\varepsilon_2 - 1)}{(\varepsilon_2 + 2)}$$
$$= (1-P)\frac{(\epsilon_2 - 1)}{(\epsilon_2 + 2)}. \quad (13)$$

In this equation ϵ_1 is permittivity of material inside the pores, ϵ_2 is permittivity of the film skeleton, and P is the film porosity. The term $P(\epsilon_1 - 1)/(\epsilon_1 + 2)$ is equal to 0 if the pores are empty, as experimentally demonstrated by Hrubesh and co-workers.

4) Relative permittivity and frequency

When the applied electric field is an ac field, the frequency of the signal comes into play. The polarization phenomena described above are very different for applied electric fields with different frequencies.

For an applied field

$$\vec{E} = \vec{E_0} e^{-i\omega t} \tag{14}$$

the polarization vector is of the form

$$\vec{P} = \epsilon_0 (\epsilon_r - 1) \vec{E_0} e^{-i\omega t} \tag{15}$$

and gives rise to a current density

$$\vec{J} = -i\omega \epsilon_0 (\epsilon_r - 1) \vec{E_0} e^{-i\omega t}, \tag{16}$$

which is imaginary as long as ϵ_r is real. This will not always be the case as will be discussed later.

Let us first consider the consequences for the polarization phenomena. Electronic polarization follows the electric field almost instantaneously as only the displacement of bound electrons is involved. The distortion polarization cannot respond as rapidly to fast changing fields since it involves the displacement of entire ions. Both electronic and distortion polarization are subject to a counter-active restoring force, which gives rise to a resonant frequency.

In contrast, orientation polarization requires the motion of complete molecules. For orientation polarization there is no counteractive restoring force. Therefore, it does not give rise to a resonance at a critical frequency, as distortion and electronic polarization do. The orientation polarization is, however, opposed by thermal disorder.

At low frequencies the three polarization phenomena contribute to the real part of the dielectric constant. The maximum frequency for orientation polarization is on the order of 10^9 Hz. Above this frequency distortion and electronic polarization contribute to the dielectric constant up to the resonance frequency for distortion polarization, which is typically in the order of ~10^{13} Hz, and beyond that only electronic polarization is defining the dielectric constant. The resonant frequency of the electronic polarization is typically beyond the frequency of visible light at ~10^{15} Hz.

It follows from Maxwell's equations that the refractive index (n_r) relates to the relative permittivity, beyond optical frequencies,

$$n_r = \epsilon_r^{1/2}. \tag{17}$$

Because of the relation between the relative permittivity and the molecular polarizability, one can relate n_r to the molecular properties as follows:

$$n_r = \left(\frac{1 + (2\alpha N/3\epsilon_0)}{1 - (\alpha N/3\epsilon_0)} \right)^{1/2} \approx 1 + \frac{\alpha N}{2\epsilon_0}. \tag{18}$$

This expression leads to the Lorenz–Lorentz formula

$$\frac{n_r^2 - 1}{n_r^2 + 2} = \frac{N\alpha(\omega)}{3\varepsilon_0}. \tag{19}$$

The characteristic response of the different polarization phenomena to the electric field results in a frequency dependence which has not only an impact on the real part of the dielectric constant, but the imaginary part is related to the counteractive restoring forces in case of electronic and distortion polarization, and to the thermal disorder in case of orientation polarization. The imaginary component of the dielectric

constant corresponds to a current density within the dielectric that is no longer exactly $\pi/2$ out of phase with the electric field.

From the frequency dependence one should note that orientation polarization in low-*k* dielectrics should be prevented as much as possible, not only for its contribution to the dielectric constant but more importantly for the imaginary part of the dielectric constant. Indeed orientation polarization leads to heat dissipation in a frequency range that is envisioned within the application frequencies of microelectronics systems.

5) Components of dielectric constant

Any two conducting plates separated by an insulator (dielectric) or a vacuum form a capacitor (C) when applying a voltage (V). And the charge (Q) is stored at the surface of the two plates. The dielectric constant which is degree of polarization of insulating material is a definition of the capacitance divided by vacuum's capacitance. However, the dielectric constant depends on the frequency of the electric field.

The dielectric constant of the film is composed of three polarizabilities, that is,

$$k_{total} = \alpha_{electronic} + \alpha_{ionic} + \alpha_{dipolar} \quad (20)$$

where $\alpha_{electronic}$, α_{ionic} and $\alpha_{dipolar}$ are electronic (~10^{14} Hz), ionic (~10^{12} Hz), and dipolar (~10^{9} Hz) polarizabilities, respectively, as shown **i**n Fig. 4. From experiments, we can distinguish three polarizabilities depending on the applied frequency. $\alpha_{electronic}$ and α_{ionic} can also be measured by ellipsometry (He-Ne laser: 632.8 nm) and Fourier transform infrared spectroscopy (FTIR), respectively.

$\alpha_{electronic}$ and α_{ionic} can be obtained from the square of refractive index (n^2) and from Kramers-Kronig relation analysis, respectively. Thus, we could determine α_{orient} as subtracting the two polarizations ($\alpha_{electronic}$+ $\alpha_{dipolar}$) from the total dielectric constant (k_{total}) at a frequency of 10^{6} Hz. Consequently, we can find which

component is the most important contribution to the dielectric constant and why the dielectric constant increases or decreases with deposition conditions and treatments [41].

As shown in Fig. 4, the polarization is a frequency-dependent, intrinsic material property [46,47]. In this section, dielectric constant and imaginary part of refractive index are expressed as ϵ and k, respectively, in order to clarify the difference between them. The dielectric constant, ϵ, can be divided into three components that result from electronic, ionic, and dipolar polarization. The dielectric constants measured at the region of microwave region due to electronic ($\triangle\epsilon_e$), ionic ($\triangle\epsilon_i$), and dipolar contributions ($\triangle\epsilon_d$) are as expressed in Eq. (21).

$$\epsilon_r \text{ (at 1 MHz)} = 1 + \triangle\epsilon_e + \triangle\epsilon_i + \triangle\epsilon_d \tag{21}$$

The dielectric constant of the material can also be calculated from the refractive

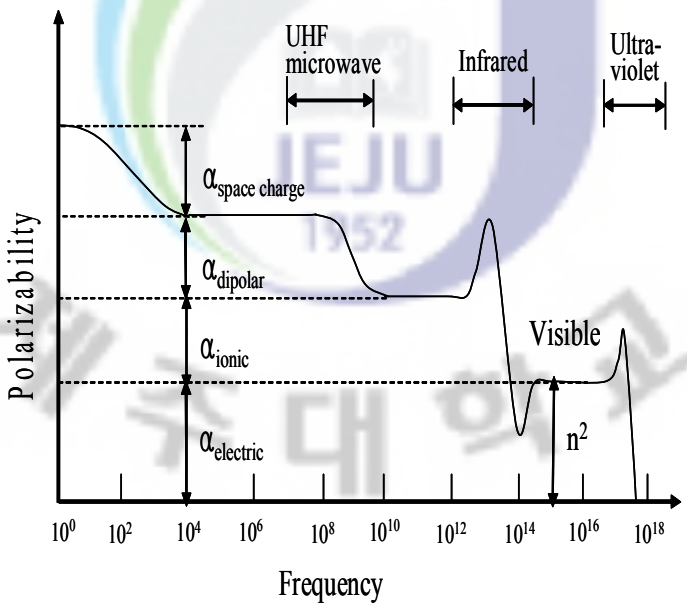

Fig. 4. Frequency dependence of the several contributions to the polarizability.

index, as expressed in Eq. (22).

$$\epsilon_r(\lambda) = n^2(\lambda) + k^2(\lambda) \tag{22}$$

where n is a real part of refractive index, k is the imaginary part of a refractive index, and λ is the wavelength of a light source.

The pure electronic contribution to the dielectric constant ($\triangle\epsilon_e$) was calculated from the refractive index obtained in the visible-ultraviolet (vis-UV) region. Since the extinction coefficient, k, of SiO_2-based materials is normally negligible in this region, the relative dielectric constant in Eq. (22) can be simply expressed as n^2.

The ionic contribution to the dielectric constant ($\triangle\epsilon_i$) was calculated by subtracting the dielectric constant at 632.8 nm, $1+\epsilon_e$, from the dielectric constant the IR region, $1+\triangle\epsilon_i+\triangle\epsilon_e$. To obtain the dielectric constant in the IR region, the refractive index was calculated from the Kramers-Kronig dispersion relation. The original Kramers-Kroing relation is expressed as in Eq.(23).

$$n_i = 1 + \frac{\pi}{2} P \int_0^{\infty} \frac{v\,k(v)}{v^2 - v_i^1} dv \tag{23}$$

where n_i is the real part of the refractive index at the i^{th} wave number at i, and k is the imaginary part of the refractive index (extinction coefficient).

The integration in Eq. (23) cannot be performed from zero to infinity since the infra-red (IR) spectrum is obtained only in a finite region (650~4000 cm^{-1}). By introducing the refractive index at 632.8 nm (n_e at v of 15,800 cm^{-1}), the above integration is approximated in a finite region of the IR spectrum as is shown in Eq. (24). The dielectric constant in the range from 4000 cm^{-1} to infinity is approximated as the dielectric constant at 632.8 nm calculated from the refractive index by ellipsometery, as explained in Eq. (22).

$$n_i = n_e + \frac{\pi}{2}\left[\int_{650}^{v} \frac{v\,k(v)}{v^2 - v_1^2}\,dv - \int_{v_i}^{4000} \frac{v\,k(v)}{v^2 - 15800^2}\,dv\right], \tag{24}$$

where n_e is the refractive index at 632.8 nm (15,800 cm^{-1}). The IR region dielectric constants were calculated by Eq. (22) and (24).

The dipolar polarization was qualitatively estimated by the Clausius-Mossotti relation in Eq. (25) [21].

$$\left[\frac{(\epsilon_r - 1)}{(\epsilon_r + 2)}\right] = \frac{\rho}{M} \times \frac{N_A}{3\epsilon_0}(\alpha_{ie} + \alpha_d) \tag{25}$$

$$\alpha_d = \frac{p^2}{3kT} \text{ (dipolar polarizability) ,}$$

where M is molecular weight, ρ is density, ϵ_r is the dielectric constant at 1 MHz, ϵ_0 is the vacuum dielectric constant, α_d is the dipolar polarizability, p is the dipole moment, k is the Boltzmann constant, and is absolute temperature.

Unlike electronic and ionic polarizabilities, dipolar polarizability is inversely proportional to temperature, as is shown by Eq. (25). Therefore, the temperature dependence of the polarizability per unit volume can imply that a dipole moment exists in the film.

2. SiOC(-H)/*p*-Si(100) interface charge

Metal-oxide-semiconductor (MOS) transistors were first produced on a commercial basis in the 1963-1964 time period. At the same time, various charges associated with the thermally oxidized silicon structure were observed to cause serious yield and reliability problems. Subsequently, a number of investigations concerned with oxide charges were started in various laboratories and many have continued to the present time [48].

The meal-insulator-semiconductor (MIS) structure is by far the most important. But, the exact nature of the Si-SiOC(-H) interface is not yet fully understood. An appealing picture of the interface is that the chemical composition of the interfacial region, as a consequence of thermal oxidation, is a single-crystal silicon followed by a monolayer of $SiO_{2-x}C_{x/2}$, that is, incompletely oxidized silicon, then a strained region of the SiOC(-H) film roughly 10～40 Å deep, and the remainder stoichiometric, strain-free, amorphous SiOC(-H) film. For a practical MIS structure, interface traps and oxide charge exist that will, in one way or another, affect the ideal MIS characteristics [49]. The basic classifications of these traps and charges are shown in Fig. 5.

1) Fixed charge (density): Q_f (N_f)

Positive charge, due primarily to structural defects (ionized silicon) in the oxide layer less than 25 Å a from the Si-SiOC(-H) interface. The density of this charge, whose origin is related to the oxidation process, depends on oxidation ambient and temperature, cooling conditions, and on silicon orientation. Since fixed charge density cannot be determined unambiguously in the presence of moderate densities of interface trapped charge, it is only measured after a low-temperature (～450 °C) hydrogen treatment which minimizes interface trap density. Fixed charge is not in electrical communication with the underlying silicon.

The fixed charge densities, which are assumed to be located at the insulator-substrate interface, were calculated from the expressions:

$$N_f = \frac{C_i}{qA}(V_{fb} + \phi_{ms}). \tag{26}$$

where C_i is the insulator capacitance, ϕ_{ms} is the metal-semiconductor work function, A is the area of the capacitor, q is the electronic charge and V_{fb} is the flat-band voltage of that C-V curve.

2) Mobile ionic charge (density): Q_m (N_m)

Primarily due to ionic impurities such as Cu^+, Li^+, Na^+, K^+, and possibly H^+. This type of charge is located either at the metal-SiOC interface, where it originally entered the oxide layer, or at the Si-SiOC interface, where it has drifted under an applied field. Drift can occur because such ions are mobile in SiOC film at relatively low temperatures. Immobile oxide charge can be distinguished from mobile ionic charge by a bias-temperature aging experiment. Gate bias is applied for a given length of time while the sample is held at a moderately elevated temperature. The density of oxide fixed charge may change under this treatment, but the centers responsible for this charge do not move. However, the mobile ionic charge can be cycled back and forth between the metal-SiOC interface and the Si-SiOC interface by this treatment without discharge, and the resulting ionic current can be detected.

3) Interface trapped charge (density): Q_{it} (N_{it})

Positive or negative charges, due to (ⅰ) structural, oxidation-induced defects, (ⅱ) metal impurities, or (ⅲ) other defects caused by radiation or similar bond breaking processes. They are located at the Si-SiOC(-H) interface. Unlike fixed charge or trapped charge, interface trapped charge is in electrical communication with the underlying silicon and can thus be charged or discharged, depending on the surface

potential. Most of the interface trapped charge can be neutralized by low-temperature (450 °C) hydrogen annealing. This charge type in the past has been called surface states, fast states, interface states, etc. In one particular case, that of interface trapped charge, it is common to express its density in terms of unit area and energy in the silicon band-gap. Also, It is well known that the D_{it} distribution is U-shaped: D_{it} is the relatively constant and as low as some 10^{10} $cm^{-2}eV^{-1}$ for the commonly used (100) silicon surface (some 10^{11} $cm^{-2}eV^{-1}$ for (111) case) around the mid-gap for state-of-the-art gate SiO_2, while it increases toward the band edges to be as large as $\cong$ 10^{13} $cm^{-2}eV^{-1}$ inside the conduction and valance bands. Here, the interface state densities of the MIS structures are determined by comparing the quasi-static C-V characteristics to the ideal C-V characteristics, allowing the absolute value of the interface state density to be determined.

D_{it} values of the MIS structures are calculated by using the following expression. The MIS capacitance at high frequencies, C_{HF}, is the series capacitance of the surface capacitance, C_s, and the dielectric layer capacitance, C_{ox} :

$$C_{HF} = \frac{C_{ox} C_s}{(C_{ox} + C_s)}, \tag{27}$$

The MIS capacitance at low frequencies, C_{LF}, is given by

$$\frac{1}{C_{LF}} = \frac{1}{C_{ox}} + \frac{1}{(C_s + C_{it})}, \tag{28}$$

where Cit is the interface trap capacitance. With Eqs. (27) and (28), the interface trap capacitance is calculated as

$$C_{it} = \left(\frac{1}{C_{LF}} - \frac{1}{C_{ox}}\right)^{-1} - \left(\frac{1}{C_{HF}} - \frac{1}{C_{ox}}\right)^{-1}. \tag{29}$$

The interface state density, D_{it}, is then given by

$$D_{it} = \frac{C_{it}}{qA}, \tag{30}$$

where q is the electronic charge while A is the area of the electrode. Then

$$D_{it} = \frac{1}{qA}\frac{C_{LF}\,C_{HF}}{C_{ox} - C_{LF}} - \frac{C_{HF}\,C_{ox}}{C_{ox} - C_{HF}}. \tag{31}$$

4) Trapped charge (density): Q_{ot} (N_{ot})

May be positive or negative due to holes or electrons trapped in the bulk of the oxide. Trapping may result from ionizing radiation, avalanche injection, or other similar processes. Unlike fixed charge, trapped charge is generally annealed out by low-temperature (<500 °C) treatment, although neutral traps may remain. In general, the densities of all of the charges except interface trapped charge may be determined using the high-frequency capacitance-voltage (C-V) technique. More elaborate measurement procedures such as "quasi-static C-V analysis" are required for interface trap charge. The trapped charge densities, which were assumed to be located at the dielectric/semiconductor interface, were calculated for the MIS structures. V_{fb} is attributed to trapping of charges by the gate dielectric film.

The equation $\triangle Q_{ot} = \triangle V_{fb}\, C_{ox}/qA$ was used to calculate the change of oxide trapped charges between the first and the second C-V measurements. Where $\triangle Q_{ot}$ is the change in the trapped charge, C_{ox} is the capacitance of SiOC(−H) dielectric film, and $\triangle V_{fb}$ is the change in flat-band voltage.

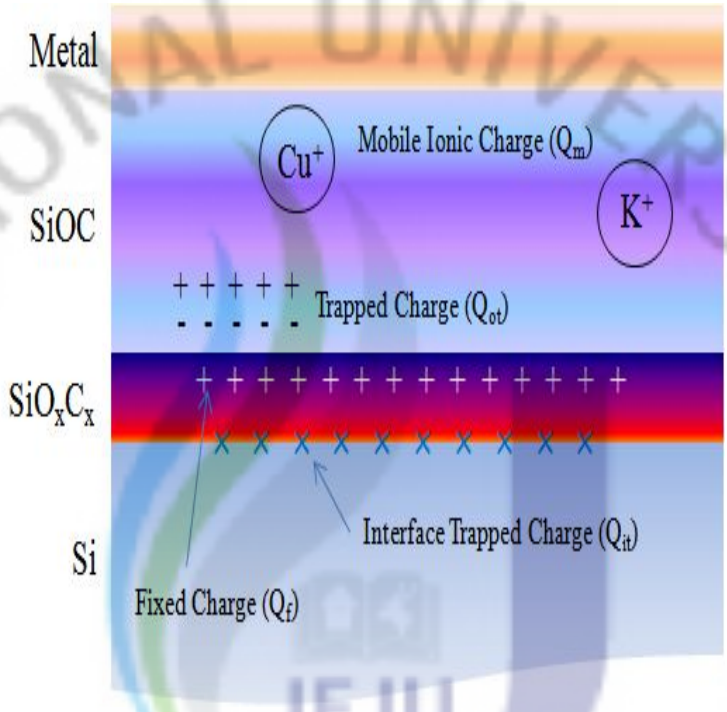

Fig. 5. Charges associated with SiOC(-H) film.

3. Defect models of the Si-SiO_2 interface

Defects within or near the interfacial region cause interface trap levels. Such defects range from stacking faults and micro-pores to various atomic or molecular fragments left as a residue of imperfect oxidation. A problem with modeling interface traps is that the structure and the chemical composition of the interfacial layer are not known. However, the results of several workers indicate the presence of non-stoichiometry at the interface and the electrically active centers [48].

Several specific defects may be responsible for interface traps produced by thermal oxidation. Four different types of defect that could exist at or near the Si-SiO_2 interface that might produce interface trap are (ⅰ) excess silicon (trivalent silicon), (ⅱ) excess oxygen (non-bridging oxygen), (ⅲ) impurities, and (ⅳ) states in oxide charge induced potential wells.

As a consequence of oxidation, there may be trivalent silicon atoms or silicon in excess of the stoichiometric amount in the SiO_2 at the interface, probably related to incomplete oxidation of the silicon or to generation of vacancies in the silicon during oxidation. In this type of defect the silicon atom shares three of its four valence electrons with neighboring silicon atoms. Its fourth unsatisfied valence bond acts as a hole and remaining neutral when empty.

In the normal SiO_2 lattice, oxygen atoms share electrons with adjacent silicon atoms, forming a "bridge" between the two silicon atoms. When one of the Si-O bonds is broken, the formerly bridging oxygen atom is now called a non-bridging oxygen. It shares one of its two valence electrons with the remaining silicon atom, and its unsatisfied valence bond acts as an electron trap becoming negatively charged by electron capture and remaining neutral when empty.

Non-bridging oxygen, oxygen in excess of the stoichiometric amount in the oxide, may be present near the interface for three reason: (ⅰ) excess oxygen associated oxygen defects; (ⅱ) the strain in the region near the interface might be relieved by formation of this defect; and (ⅲ) there are water-related electron traps near the

Si-SiO_2 interface that might be related to non-bridging oxygen defects.

Both trivalent silicon and non-bridging oxygen centers are known to react with hydrogen. In this reaction the unsatisfied valence bond is satisfied for both types of defect; hence such a reaction is likely to render these defects electrically inactive. For non-bridging oxygen centers, reaction with water seems to render them neutral. Thus both types of center are consistent with the observation that interface traps are annihilated by annealing in hydrogen or water vapor.

There is some tentative experimental evidence that trivalent silicon exists in SiO_2 and may act as interface traps. Nishi and Poindexter et. al. interpret their electron spin resonance signals is found to increase or decrease in the same manner as mid-gap interface trap level density under oxidation or annealing variations. Thus the spin resonance signal appears to be related to mid-gap interface trap level density. They conclude that the most likely source of the spin resonance signal observed in their samples is trivalent silicon. However, conclusive evidence for the species responsible for the observed spin resonance signal awaits the detection of hyperfine structure which is a difficult measurement. The trivalent silicon defect is consistent with a bond disorder model.

The third type of defect is an impurity atom at the interface. Because strain at the interface creates a potential minimum for impurities, the interface can accommodate many of the impurities incorporated in the relatively open SiO_2 lattice. There is also a strained region at the metal-SiO_2 interface. Strained regions at either interface are likely to act as sinks for impurities incorporated in the oxide.

The fourth type of defect is an oxide charge near the interface that induces an attractive coulombic potential well in the silicon. The interface trap model based in this defect has been discussed earlier in this section. There is evidence from low temperature measurements that sodium ions drifted to the Si-SiO_2 interface induce an interface trap band near the conduction band edge.

Using conductance measurements on thin oxides, Kar and Dahlke [50] obtained evidence that metal impurities can cause interface traps. These workers diffused the

metal evaporated onto the thin oxide surface all the way to the Si-SiO_2 interface by heating the sample. Avalanche injection experiments, display interface trap buildup. These interface traps appear to be donor type. The exact mechanism of their formation is unknown. Another defect, associated with the cleavage of strained Si-O bonds, is the E' center. This center consists of a non-bridging oxygen and a trivalent silicon atom formed when an Si-O bond is broken. Such a defect is likely to result from radiation damage.

The above-mentioned defect models, however, may predict that each kind of defect has a single separate energy level and cannot explain the shaped continuous energy distribution which is characteristic of the interface states. A bond model has been proposed by taking account of bond distortions with a distribution of the bond length or angle, which may be caused by local strain at the Si-SiO_2 interface. As shown in Fig. 6, the calculation reproduces the continuous energy distribution in the upper and lower halves of the band-gap by assuming a distributed bond length x for Si-O and Si-Si weak bonds, respectively. It may be worth noting that the interface state energy distribution extends toward inside the valence and conduction bands. At present, all the above models remain qualitative and speculative since there seems no independent experimental support.

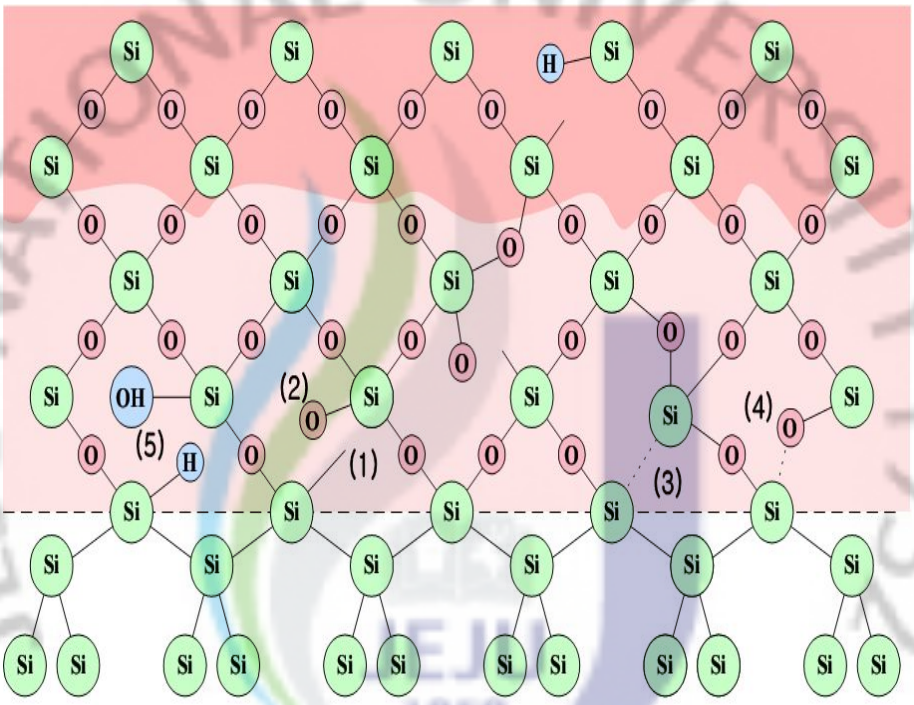

Fig. 6. Atomic configurations and defects near the Si-SiO_2 interface.

4. Electrical conduction mechanism of insulator

Electronic conduction through thin insulating films has been the subject of intensive theoretical and experimental investigation. This study is important both in understanding transport phenomena and in the operation of practical devices. A summary of the large number of theoretical and experimental work can be found in several excellent references [51,52]. The primary concern of the conduction mechanisms in thin insulating films is at high electrical field, since applied bias as low as a few volts will induce electrical fields of order 104 to 106 V/cm in thin films of 100 Å to 1,000 Å thick. Usually, the current passing through the insulating layer could be due to ionic conduction or electronic conduction. For ionic conduction, ions move through the insulating film under the influence of a large electric field, for electronic conduction in a large field, the mechanisms could be classified as follows [49,53,54]:

Table 3. Basic conduction processes in insulators [49].

Process			Expression of the current [a]	Voltage and temperature dependence [b]
Electronic conduction	Electrode limited current	Schottky emission	$J = A^{*}T^{2}\exp(\frac{-q(\phi_B - \sqrt{q\epsilon/4\pi\epsilon_i}}{kT})$	$\sim T^{2}\exp(+a\sqrt{V}/T - q\phi_B/kT$
		Frenkel-Pool emission	$J \sim E\exp(\frac{-q(\phi_B - \sqrt{qE/4\pi\epsilon_i}}{kT})$	$\sim V\exp(+2a\sqrt{V}/T - q\phi_B/kT$
	Bulk limited current	Tunnel or field emission	$J \sim E^{2}\exp(-\frac{4\sqrt{2m^{*}}(q\phi_B)^{3/2}}{3q\hbar E})$	$\sim V^{2}\exp(-b/V)$
		Space-charge-limited	$J = \frac{9\epsilon_i \mu V^{2}}{8d^{3}}$	$\sim V^{2}$
Ionic conduction			$J \sim \frac{E}{T}\exp(-\triangle E_{ai}/kT)$	$\sim \frac{V}{T}\exp(-d/T)$

[a] A^{*}=effective Richardson constant, ϕ_b=barrier height, E=electric field, ϵ_i=insulator dynamic permitivity, m*=effective mass, d=insulator thickness, $\triangle E_{ae}$=activation energy of electrons, $\triangle E_{ai}$=activation energy of ions, and $a \equiv \sqrt{q/4\pi\varepsilon_i d}$. [b] $V=Ed$. Positive constants independent of V or T are b, c, and d'.

1) Electrode limited mechanisms.

These mechanism including, tunneling and Schottky emission processed, are operative in the vicinity of the contact/insulator interface. In this case, the current -voltage (I-V) characteristics will be virtually thickness independent, because essentially all the applied voltage appears across the metal-dielectric contact and very little across the bulk. Conduction is limited by the transfer of charge from the contact to the insulator, once charge is injected it has little difficulty migrating to the other electrode.

(1) Schottky emission

The electrode-limited Schottky emission mechanisms can be understood as follows. At the metal-dielectric constant, there is a potential barrier due to the work function or electronic affinity difference between the metal and the insulator. an electron in the metal may pass into the conduction band of the dielectric in two extreme way: (ⅰ) tunneling from the metal through the forbidden band of the dielectric, and (ⅱ) jump over the Schottky barrier height.

The Schottky effect is due to the image-force lowering of the barrier height when an electric field is applied. This can be seen by referring to Fig. 7. The line C and B represents the bottom of insulator conduction band, the dotted line A and B represents potential barrier $\Phi(x)$, the dotted line C and D represents the potential due to applied field, which when added to the barrier potential $\Phi(x)$ produces the potential step shown by the line AD, which is seen to be $\Delta\Phi$ in the barrier height due to the interaction of the applied field (E) with the image potential is given by

$$\Delta\Phi = \left(\frac{q^3}{4\pi K^* \epsilon_0}\right)^{1/2} E^{1/2} = \beta_S E^{1/2}, \tag{32}$$

$$\text{where } \beta_S = \left(\frac{q^3}{4\pi K^* \epsilon_0}\right)^{1/2} \tag{33}$$

and $K^* = n^2$, is optical (high frequency) dielectric constant, n is the refractive index. Because of the image-force lowering of the barrier, the electrode-limited current obeys the Schottky-Richardson relation:

$$J_S = AT^2 \exp(-\frac{q\Phi_B}{kT}) \exp\frac{\beta_S}{kT} E^{1/2}, \tag{34}$$

$$\text{where } A = \frac{2qm^* k^2}{(2\pi)^2 h^3} \tag{35}$$

In Eqs. (32)~(35), A is called the Richardson-Dushman constant(equal to $120\times(m_0/m^*)$A(cm · deg.)$^{-2}$ where the temperature in °C and m_0 denotes the mass of an electron at rest, m^* is the effective mass of the carriers in the insulator), β_S is the Schottky slope, Φ_B represents a barrier height, E is the applied electric field, k is Boltzmann's constant, h is the Planck's constant, q denotes the electronic charge, ϵ_0 is the permittivity of free space.

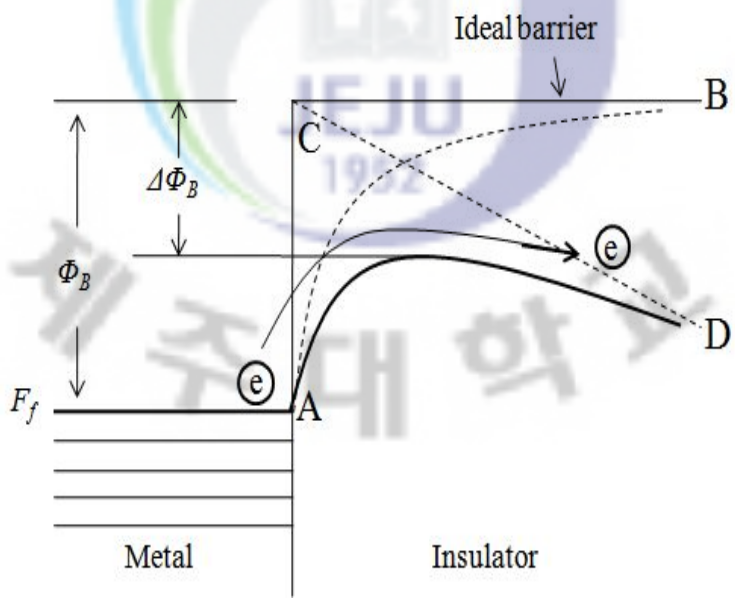

Fig. 7. The electrode-limited Schottky emission mechanism.

(2) Fowler-Nordheim tunneling

In metal-insulator-metal (MIM) structure, a potential barrier becomes narrow as the electric field increases. The width of potential barrier is about 10 nm. In this case, the electron penetrates the potential barrier and transports to the opposite electrode. This is called tunneling effect, and phenomenon of electron emission due to tunneling effect is called high-field emission. Figure 8 shows a phenomenon of field emission due to tunneling effect. Tunneling conduction mechanism is dependent on the electric field and energy barrier, but is independent on temperature. Tunneling conduction mechanism can be explained by Fowler-Nordheim analysis. That is,

$$J_{FN} = E^2 \exp[-\frac{4\sqrt{2m^*}(q\Phi_B)^{3/2}}{3q\hbar E}]. \quad (36)$$

where m^* is the effective mass and $\hbar$ is the reduced Planck's constant.

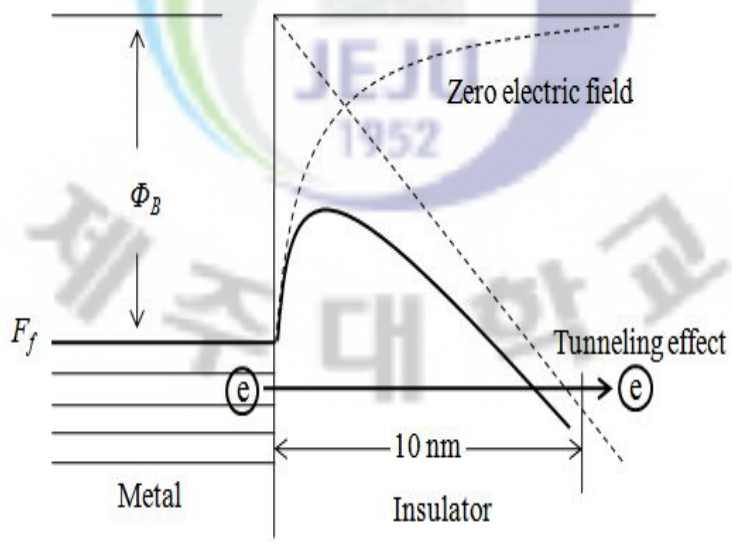

Fig. 8. The electrode-limited Fowler-Nordheim tunneling mechanism.

2) Bulk limited mechanisms

In this case sufficient numbers of charge carriers are injected into the insulator conduction band by Schottky emission or tunneling. However, it is difficult for the carriers to reach the other electrode because of bulk transport limitations. Bulk limited mechanisms include space charge-limited, intrinsic, and Pool-Frenkel conduction mechanisms.

(1) Space charge limited conduction model and ionic conduction

The magnitude and nature of the current flow changes markedly when the situation is one in which a dominant trap or set of traps exists in the material. In this case, the equilibrium concentration of mobile carriers is greatly reduced, since many of the electrons in the system now occupy trap states. The space charge limited conduction results from a carrier injected into the insulator, where no compensating charge is present. Low electric field in the insulator, there are more thermally generated carriers than the injected carriers. In this case, the thermally generated carriers are dominant in the insulator. Then, the current density follows Ohm's law, which can be expressed by [41]:

$$J_{Ohm} = e\, n_0 \mu \frac{V}{d} \tag{37}$$

where, e is an electronic charge, n_0 a thermally generated carrier density, μ a carrier mobility, V an applied voltage, d a thickness of insulator. Region 1 in Fig. 9 obeys Ohm's law. When an applied voltage across the insulator increases, there are more injected carriers than the thermally generated carriers. Assuming I_{ins} to be a total current of insulator inside and I_{inj} to be an injection current from cathode into insulator, the injection current is greater than the total current inside the insulator. In this case, the carriers injected from cathode to lowest unoccupied molecular orbital (LUMO) of insulator form a space charge, and the current is limited by the space charge layer. Let us assume that $F(x)$ is the electric field at x along the normal direction from metal surface to insulator inside and $n(x)$ is the number of free

electrons per unit volume. If there is no trap state in the insulator, then the space charge limited current density (J_{SCLC}) is given by:

$$J_{SCLC} = ne\,\mu F - De\left(\frac{dn}{dx}\right), \tag{38}$$

where μ is a carrier mobility and D is a diffusion coefficient.

In Eq.(38), Poisson's equation is defined as

$$\frac{dF}{dx} = \frac{ne}{\epsilon}, \tag{39}$$

where $\epsilon(=\epsilon_0\epsilon_r)$ is a dielectric constant. In Eq. (39), n is

$$n = \frac{\epsilon}{e}\frac{dF}{dx}, \tag{40}$$

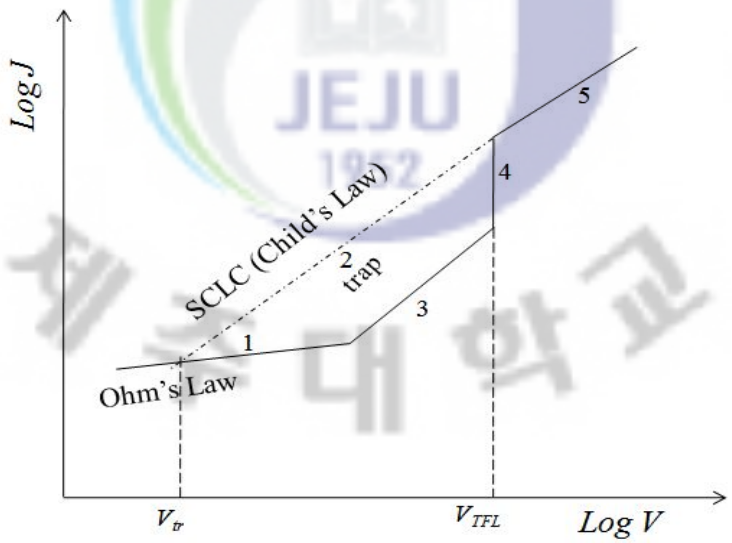

Fig. 9. Current-voltage characteristics of insulator (V_{tr}: transition voltage, V_{TFL}: trap-filled limit voltage).

Substitution of Eq.(38) into Eq. (40) gives

$$J_{SCLC} = \frac{\epsilon}{e} e \frac{dF}{dx} \mu F - D e \frac{d^2F}{dx^2} \frac{\epsilon}{e}, \tag{41}$$

when Einstein's relation, $\mu/D = e/kT$, is substituted

$$J_{SCLC} = \epsilon \mu F \frac{dF}{dx} - \mu kT \frac{d^2F}{dx^2} \frac{\epsilon}{e}. \tag{42}$$

where k is Boltzmann constant. In Eq. (42), after ignoring the last diffusion term in the right-hand side, and integration of the equation becomes,

$$J_{SCLC}\, dx = \epsilon \mu F\, dF, \tag{43}$$

$$\int_0^{x+x_0} J_{SCLC}\, dx = \epsilon \mu \int F\, dF, \tag{44}$$

$$J_{SCLC}(x + x_0) = \epsilon \mu \frac{1}{2} F^2, \tag{45}$$

$$F^2 = \frac{2J_{SCLC}(x + x_0)}{\epsilon \mu} = \frac{2J_{SCLC}}{\epsilon \mu}(x + x_0), \tag{46}$$

$$F = \sqrt{\frac{2J_{SCLC}}{\epsilon \mu}(x + x_0)}. \tag{47}$$

And the voltage drop across the insulator can be expressed as

$$V = \int_0^d F\, dx \tag{48}$$

Replacement of Eq. (47) becomes

$$V = \int_0^d \sqrt{\frac{2J_{SCLC}}{\epsilon\mu}(x+x_0)}\ dx,$$

$$= \sqrt{\frac{2J_{SCLC}}{\epsilon\mu}} \int_0^d \sqrt{(x+x_0)}\, dx,$$

$$= \frac{2}{3}\sqrt{\frac{2J_{SCLC}}{\epsilon\mu}}\,[(d+x_0)^{3/2} - x_0^{3/2}]. \tag{49}$$

If $x_0 \ll d$, one obtains

$$V = \frac{2}{3}\sqrt{\frac{2J_{SCLC}}{\epsilon\mu}d^3}\,, \tag{50}$$

$$\frac{V^2}{d^3} = (\frac{8}{9})\frac{J_{SCLC}}{\epsilon\mu}, \tag{51}$$

$$J_{SCLC} = \frac{9}{8}\epsilon\mu\frac{V^2}{d^3}. \tag{52}$$

where, Eq. (52) is referred to Mott and Gurney equation. Region 2 in Fig. 9 can be explained by Mott and Gurney equation. At low voltage and high temperature, current is carried by thermally excited electrons hopping from one isolated state to the next. this mechanism yields an ohmic characteristic exponentially dependent on the temperature.

The ionic conduction is similar to a diffusion process. Generally, the direct current (dc) ionic conductivity decreases during the time the electric field is applied. because ions cannot be readily injected into or extracted from the insulator. After an initial current flow, positive and negative space charges will build up near the metal-insulator and the semiconductor-insulator interfaces, causing a distortion of the potential distribution. When the applied field is removed, large internal fields remain which cause some, but not all, ions to flow back toward their equilibrium position.

(2) Poole-Frenkel emission

The Poole-Frenkel effect is the lowering of a Coulomb potential barrier when it interacts with an electric field and is usually associated with the lowering of a trap barrier in the bulk of an insulator. To experience the Poole-Frenkel effect, a trap is required to be positively charged. That is, it must be positively charged when empty and uncharged when filled, the interaction between the positively charged trap and the electron giving rise to the Coulomb barrier, as shown in Fig. 10.

This process is the bulk analog of the Schottky effect at an interfacial barrier. The difference is that Poole-Frenkel lowering of a Coulomb barrier $\Delta\Phi_{PF}$ is now given by:

$$\Delta\Phi_{PF} = \left(\frac{q^3}{\pi K^* \epsilon_0}\right)^{1/2} E^{1/2} = \beta_{PF} E^{1/2}, \tag{53}$$

$$\text{where } \beta_{PF} = \left(\frac{q^3}{\pi K^* \epsilon_0}\right)^{1/2} \tag{54}$$

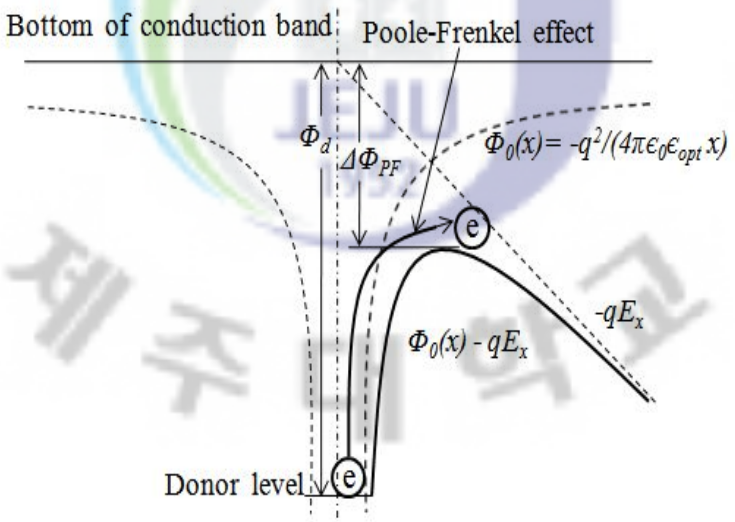

Fig. 10. The bulk-limited Poole-Frenkel emission mechanism.

is Poole-Frenkel coefficient, Note that $\beta_{PF} = 2\beta_S$.

Therefore, Poole-Frenkel effect can be written in the form:

$$J_{PF} = C E \exp(-\frac{q\Phi_d}{kT})\exp[\frac{\beta_{PF} E^{1/2}}{r kT}]. \quad (55)$$

where C is a constant, which is proportional to the density of trapping centers, Φ_d is the depth of the donor level, r is a parameter, $1 \leq r \leq 2$, which takes into account the trapping sites in insulator, β_{PF} is the Poole-Frenkel constant. On plotting $\ln(J/E)$ vs. $(1/kT)$, the resulting slope will be $-\Phi_d + \beta_{PF} E^{1/2}$, from which the Coulomb potential barrier height Φ_d can be obtained.

Chapter Ⅲ. Experimental and Analyses

1. Experimental procedures and deposition conditions

1) Experimental procedures

SiOC(-H) thin films were deposited on *p*-Si(100) substrates using a mixture of dimethyl-dimethoxy-silane (DMDMS, $C_4H_{12}O_2Si$) precursor and oxygen gas in a plasma-enhanced chemical-vapor deposition (PECVD) system. Figure 11 show the precursors of DMDMS. The DMDMS precursor is a nontoxic, colorless transparent liquid with a purity of 99%; density of 0.865 g/cm^3; a boiling point of 82 °C at standard atmospheric pressure and the molecular weight 120.22 g/mol. It was vaporized and carried by inert argon gas from a thermostatic bubbler to the reaction chamber. Figure 12 shows the schematic of PECVD system, which the antenna is an inductively coupled plasma (ICP) type. The plasma was generated using a radio frequency (RF) power supply with a frequency of 13.56 MHz applied between the two electrodes. To improve the SiOC(-H)/*p*-Si(100) interfaces, the silicon wafer was cleaned using the RCA cleaning process and rinsed in deionized water before depositing the SiOC(-H) thin films. To prevent recondensation of the DMDMS precursor, we heated the bubbler and all the gas delivery lines, and kept them at a constant temperature of 40 °C. Before depositing the SiOC(-H) thin films, the chamber was evacuated to a pressure of less than 10^{-3} Torr and the working pressure was fixed at 100～700 mTorr. After the deposition, had been deposited 750, 500, and 250-μm circular patterns of high-purity Al and Cu metals with a thickness of 300 nm were thermally evaporated by using a shadow mask. To form Ohmic contacts, we evaporated the Al metal with a thickness of 200 nm onto the whole back surface of the *p*-Si(100) wafer. To improve the electrical properties of the MIS structure, the post-metallization was performed at 250 °C.

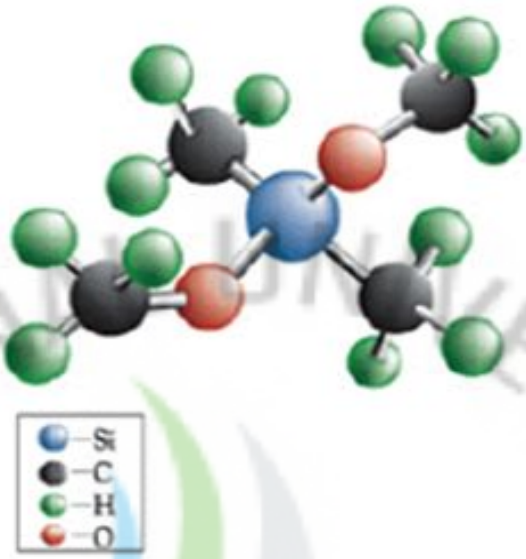

Fig. 11. Schematic diagram of DMDMS precursor.

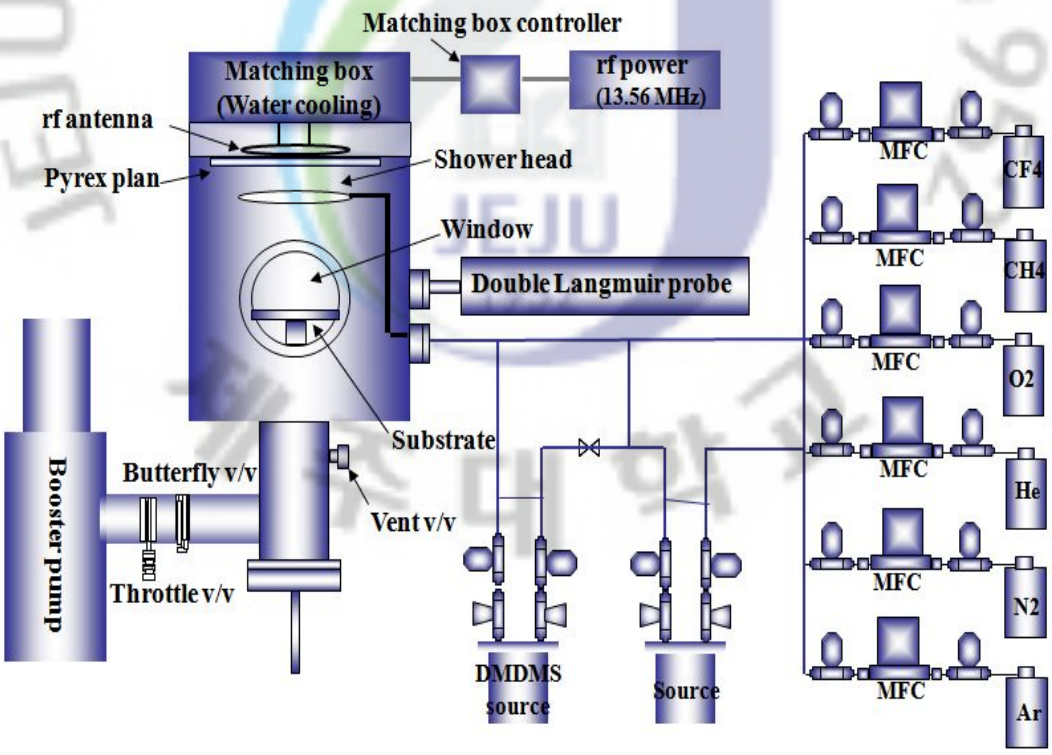

Fig. 12. Schematic of PECVD (ICP type) system.

2) Deposition conditions

In order to investigate the structural and electrical properties of the SiOC(-H) films, we had fabricated three kinds of the deposition conditions such as, rf powers, flow rate ratios and substrate temperatures as following:

(1) SiOC(-H) films deposited with various rf powers.

The SiOC(-H) films for various rf powers were deposited at room temperature, which the rf powers were varied from 400 to 800 W. The total flow rate of the precursors was maintained as 50 sccm, and flow rate ratio of R (%)=[DMDMS/(O_2+DMDMS)]×100 was fixed at 80%.

(2) SiOC(-H) films deposited with various flow rate ratios.

The SiOC(-H) films for various flow rate ratios were deposited at room temperature and 700 W of an rf power. The total flow rate of the precursors were maintained as 50 sccm, and the flow rate ratio of R (%) = [DMDMS/(O_2+ DMDMS)]×100 was varied from 50 to 100%.

(3) SiOC(-H) films deposited at various substrate temperature.

The SiOC(-H) films were deposited at room temperature, 100, 200 and 300 °C. the rf power was fixed at 700 W, which the flow rate ratio of R (%) = [DMDMS/(O_2+ DMDMS)]×100 was fixed 50%, and the total flow rate of the precursors were maintained as 50 sccm.

3) Fabrication of the Cu(Al)/SiOC(-H)/*p*-Si(100) MIS structures

The SiOC(-H) films for electrical properties of the Cu(Al)/SiOC(-H)/*p*-Si(100) MIS structures were deposited at room temperature, and the RF power was 700 W. The total flow rate of the precursors was maintained at 40 sccm, and the flow rate ratio, R(%) = [DMDMS/(O_2+DMDMS)]×100, was fixed at 80%. The deposited SiOC(-H) films were annealed at a temperature from 250 to 450 °C in a vacuum. After annealing the films, top electrodes of the Al or the Cu metallization were deposited by thermal evaporation, and the MIS capacitors were fabricated by lithography and

the wet-etch technique, which the thickness of electrode is about 300 nm.

4) Experiments for the electro-physical properties

The charge trapping behavior of the Cu/SiOC(-H)/*p*-Si(100)/Al and Al/SiOC(-H)/*p*-Si(100)/Al samples was studied using applied electric bias stress. The Cu capacitors concurrently underwent bias temperature stress (BTS) at 175-275 °C with a constant dc gate bias of +30 V corresponding to an initial electric field of 2 MV/cm in the SiOC(-H). The samples were heated to the test temperature while a bias was then applied for durations ranging from 10 to 40 min. The gate current was monitored during the BTS treatment. When the stress period was over, the capacitors were quenched immediately to room temperature to prevent the Cu^{+} ions from back drifting. High frequency (1 MHz) sweeps from inversion to accumulation were obtained at 20 °C before and after stressing. During the tests, the MIS structures were vacuum tightened to a water cooled chuck. The current-voltage (I-V) characteristics of the Cu/SiOC(-H)/*p*-Si(100) MIS structure were measured at various temperatures from 15 to 200 °C by using a semiconductor parameter analyzer. The capacitance-voltage (C-V) characteristics were measured for the MIS structure Al/SiOC(-H)/*p*-Si(100)/Al at various frequencies ranging from 1 to 5 MHz by using semiconductor parameter analyzer.

Table 4. Experimental condition.

Plasma Source	ICP
rf power	100～800 W
Total flow rate	40 sccm
O_2 gas flow rate	6～22 sccm
DMDMS (Ar gas) flow rate	18～34 sccm
Initial pressure	～10^{-3}
Working pressure	300, 700, 100 mTorr
Deposition time	2～5 min
Annealing temperature	250～450 °C
Substrate temperature	100～300 °C
Wafer	*p*-type Si(100)

2. Analysis of the SiOC(-H) films

1) Plasma diagnostics

The plasma parameters were measured by using Langmuir (wise probe 2000, P&A Solution) technique. A wise probe that can measure plasma densities and the electron temperatures in real-time was installed on the chamber wall. A wise probe for comparison was made of a stainless tip, 1 mm in diameter and 10 mm in length. The probe current is measured through the current sensing resister. Optical emission spectroscopy (OES) was performed by an optical fiber and a monochromator (Triax series 320) equipped with a photomultiplier. Emission spectra measured the intensity of light of various wavelengths emitted from the plasma chemical reaction. The light emitted from the micro-plasma was collected by optical fiber and transferred to a spectrometer. These spectra were measured using a calibrated spectrometer with a resolution of 0.3 nm

2) Fourier transform infrared spectroscopy

The properties of the SiOC(-H) film such as bonding mode, spectrum of the full width at half maximum (FWHM), peak position, related carbon concentration, peak area ratio, have been characterized by Fourier transform infrared (FTIR) spectra. FTIR spectroscopy (IFS-120HR/FRA-106S Bruker) was used to determine the related Si-O-C bonding configurations in the film. All FTIR absorption spectra were acquired with a resolution of 2 cm^{-1} by using a Si wafer as a reference. The number of scans was automatically chosen and averaged for each spectrum in order to ensure an optimal signal to noise ratio. To compare the spectra, we subtracted a proper baseline from all the recorded FTIR spectra.

3) X-ray photoelectron spectroscopy

Chemical state of the element, bonding energy and transition of each elements

bonding energy according to carbon concentration distribution and annealing condition, initial forming procedure and reaction mechanism are investigated by X-ray photoelectron spectroscopy (XPS, ESCA 2000-Lab). The X-ray source was a monochromatic Al ka (1486.6 eV) anode kept at 14 kV and 20 mA. Survey scan spectra and narrow scan spectra of each element are proceeded at the pass energy of 100 eV and 20 eV, respectively. The base pressure in the analysis chamber was 5×10^{-9} Torr.

4) Measurements of electrical properties

The electrical properties of the SiOC(-H) films, such as dielectric constant, leakage current and breakdown voltage, are measured by C-V and I-V measurements. The applied voltages for C-V and I-V measurements are -60 V to 30 V and 0 V to 100 V, respectively. The dielectric breakdown is the dc voltage at which permanent dielectric breakdown occurred and then the one is divided by film thickness. The dielectric constant at 1 MHz and current-voltage (I-V) characteristics were measured by a HP4280A(Agilent B1500) C-V meter and HP4140 B meter, respectively.

5) Measurements of mechanical properties

Nano-indentations were made using a Nanoindenter XP system (MTS, USA) with a continuous stiffness measurement (CSM) and Berkovich diamond indenter with a tip radius of approximately 80 nm. The nano-indentation system was fully calibrated before the measurements by using fused silica as a standard sample. The Nanoindentation experiments were carried out by loading to a maximum depth of 150 nm, unloading to 5% of the maximum load and holding for 20 s to correct for thermal drift; and then completing the unloading. To obtain reliable data, we made a minimum of nine indents on each sample. The elastic modulus (E) and the hardness (H) of each sample were averaged with respect to the indentation depth.

6) Measurements of thickness and refractive index

The thickness and the refractive index, deposition rate as a function of flow rate, rf power, substrate temperature and annealed condition of the SiOC(-H) films were measured by an spectroscopic ellipsometery (ST4000) at a wavelength of 632.8 nm. And the relationship between film morphology and deposition, annealed condition could be seen from the field emission scanning electron microscopy (FE-SEM, JSM-6700F) images.

7) High resolution transmission electron microscope

The diffusion behavior of Cu atoms and the interface structural morphology of Cu/SiOC(-H)/*p*-Si(100) was characterized by high resolution transmission electron microscope (HR-TEM, JEOL JEM 3010).

8) Auger electron spectroscopy

Atomic compositional depth profile analysis was performed by Auger electron spectroscopy (AES, ULVAC PHI 700) with 5 keV Ar ion sputtering. The sample stage was titled 15° while the sputtering rate for depth profiling was 0.6 Å/s.

Chapter Ⅳ. Structural and Electrical Properties of the SiOC(-H) films

1. SiOC(-H) films deposited with various rf powers

Figure 13 shows the electron density and electron temperature of the DMDMS+O_2 bulk plasma as a function of the rf power measured by the Langmuir probe. The N_e and T_e increased monotonically with rf power. As the rf power increased from 100 to 800 W, the corresponding N_e and T_e were found to be increased from 6.23×10^{8} to 1.22×10^{10} cm^{-3} and from 1.57 to 2.03 eV, respectively. It was observed that N_e gradually increases with increasing rf power up to 400 W, and then rapidly increases for an rf power of 500 W and reaches a maximum value (1.22×10^{10} cm^{-3}) for an rf power of 800 W. On the other hand, T_e also linearly increases with increasing of rf power up to 400 W and then drops suddenly for the rf power of 500 W, afterwards, again increases gradually for rf powers up to 800 W. This rapid transition of the plasma parameters are as shown in the Fig. 13. From these results, we clearly see that the applied rf power in the PECVD chamber with DMDMS+O_2 precursors will exhibit a rapid transition between electrostatic (*E*) and electromagnetic (*H*) modes of the plasma discharge following the application of an rf power around 500 W. Mode transition is determined by a sudden and huge change in the luminance [55]. The *H* mode is characterized by a much higher luminance and plasma density, so this transition may be connected with the dynamics of the atoms and the direct ionization of the atoms by the electron impact [56]. At the *H* mode, many ionic and atomic spectra are observed compared to the *E* mode. During the generation of the plasma, free electrons gain kinetic energy from the applied rf power and lose it in collisions with neutral molecules and atoms. As the rf power is increased beyond 500 W, which results in a full discharge of bulk plasma in the chamber, the internal

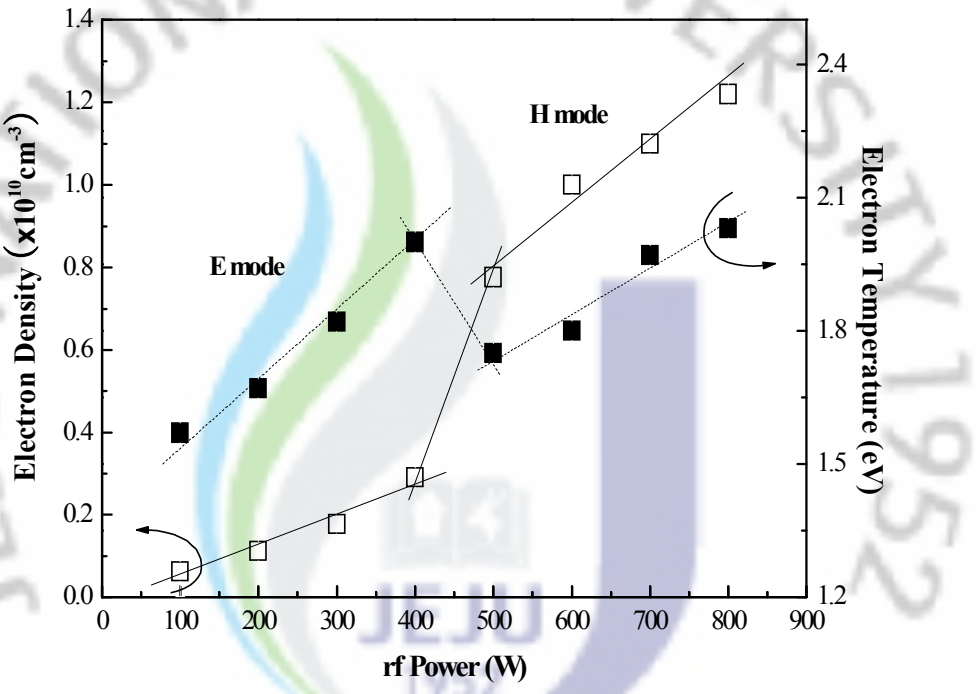

Fig. 13. Electron density (N_e) and electron temperature (T_e) as a function rf power.

energy of the gas molecules becomes high and the molecules can then be excited, dissociated and ionized. Thus, a complete dissociation of the precursor take place, leading to a greater abundance of reactive radicals and ions in the chamber.

Figure 14 shows the deposition rate of the SiOC(-H) as a function of rf power. The deposition rate of the SiOC(-H) film increased rapidly with the rf power. We performed the SiOC(-H) deposition process from a starting rf power of 400 W since the film deposition did not occur at an rf power of 300 W. As shown in Fig. 14, there are three different steps found during the deposition of the SiOC(-H) films involving different rf powers. In this case, the deposition rate is almost proportional to the N_e and T_e which is directly evidenced by the different regimes as shown in Fig. 18. The deposition rate is increased about 14 times for films deposited with an rf power of 800 W (140 nm/min) compared with the rate for films prepared with an rf power of 400 W (10 nm/min). Normally, the deposition rate of the SiOC(-H) films depends on the plasma parameters, as the rf power increases, consequently, the electron density increases rapidly which resulted in a higher deposition rate (see Fig. 13).

Figure 15 shows typical optical emission spectra of the DMDMS+O_2+Ar bulk plasma with different rf powers. During the plasma polymerization, the reactive species first dissociated and then were deposited on the Si substrate to form the SiOC(-H) film. From the emission spectra, the detected species were identified as C_3, CH, CO, H_α, C_2, O, H_2, H_β, Si and Ar. All the peaks appearing in the emission spectra are labeled as shown in Fig. 15. These reactive species come from the DMDMS precursor in which the -CH_3 radicals were dissociated by the rf power. This is an effect associated with increasing electron density or electron temperature but the most important reason is probably the complete discharge of the DMDMS precursor. All the emission lines increase with increasing rf power, above 500 W. Their behavior for lower rf powers (<400 W) is questionable due to the very low signals. However, a small deposition of the SiOC(-H) film could be possible with an rf power of 400 W as is shown in Fig. 14.

Figure 16 shows the normalized emission intensity (I_x/I_{Ar}) of each species as a

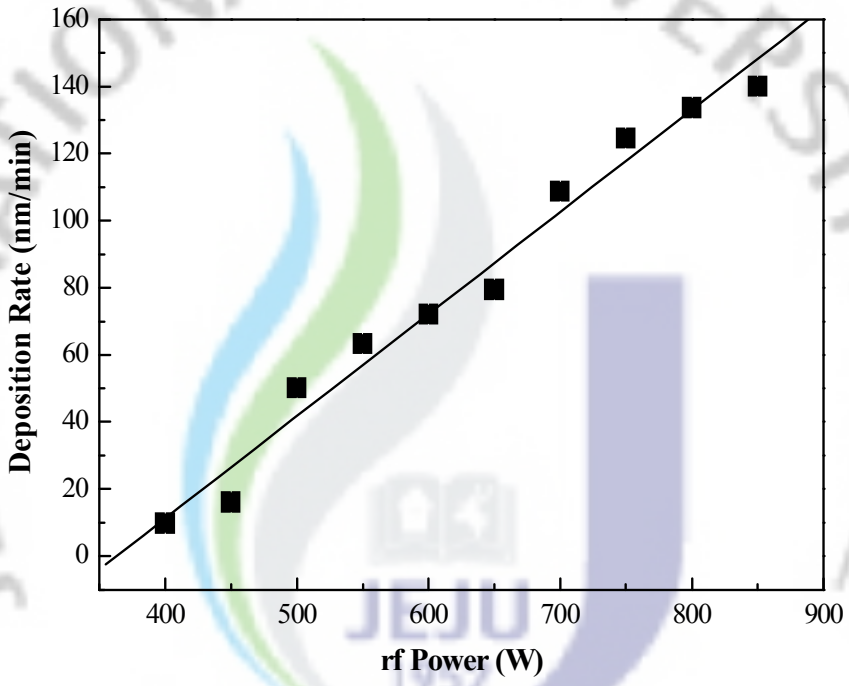

Fig.14. Deposition rate of the SiOC(-H) films as a function of rf power.

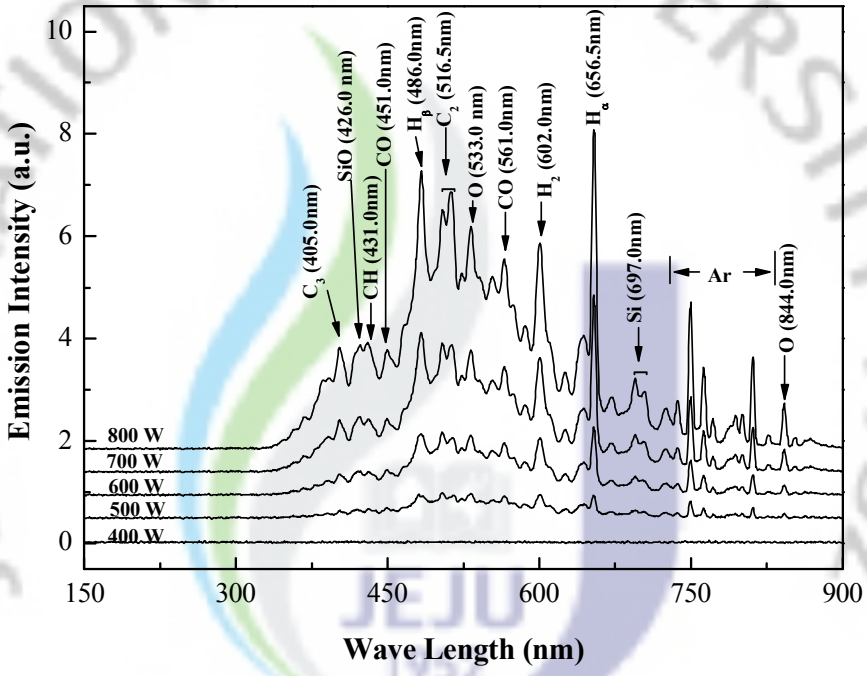

Fig. 15. Optical emission spectra from the DMDMS+O_2+Ar plasmas for different rf powers.

function of different rf powers, where I_x in the emission intensities of each species. The changes in the relative intensities of the CH, C_3, C_2, O, CO species and other species are found to be linearly increased with rf power. This result means that the methyl groups in the DMDMS precursor decomposed by releasing of one H_α or H_β ions. However, the relative intensities of the Si and SiO species remain almost unchanged with variations in applied rf power. This is because, the molecular ions with energies above 100 eV generally dissociate when striking the substrate surface, the dissociation is considered only in terms of atomic ions [57]. Due to the greater mass difference with H ions (H_α or H_β) one can expect the relative emission intensities of the Si and SiO species to be unchanged. The dissociation of SiO, Si and O taking place is due to the break up of the Si-O network chain by the application of rf power. The broken Si-O chain is much easier, because the thermal stability of the Si-O-Si bond in organosilicon compounds is lower than that of the Si-O bond in SiO_2 [58].

Figure 17 shows the FTIR absorption spectra from 700 to 4000 cm^{-1} of the SiOC(-H) film deposited with various rf powers. The spectrum consists of several bands or groups of bands occurring along the overall spectral range. The characteristic band of the SiOC(-H) film showed absorption bands due to Si-O-Si (at around 1055 cm^{-1}), Si-O-C (at around 1105 cm^{-1}), $Si-CH_3$ (at around 950 and 1250 cm^{-1}) and -OH (at around 3200-3700 cm^{-1}) in addition to those of the Si substrate. The Si-O-Si asymmetric stretching frequency of the SiOC(-H) film shows a very strong infrared absorption band in the region of 1000-1250 cm^{-1}. This Si-O-Si absorption band becomes broader or more complex, showing three or four overlapping bands. There is a shoulder at about 1150 cm^{-1} in all the absorption spectra, assigned to the broad Si-O-C peak, which corresponds to the Si-O-C cage-link structure. This structure produces a more porous nature in the SiOC(-H) film [40,43].

Figure 18 shows the deconvoluted bonding configurations of the Si-O-Si, Si-O-C, $Si-CH_3$, $-CH_3$ and $-CH_n$ related structures of the SiOC(-H) films deposited with different rf power levels. Figure 18(a) shows the deconvoluted FTIR spectra of the

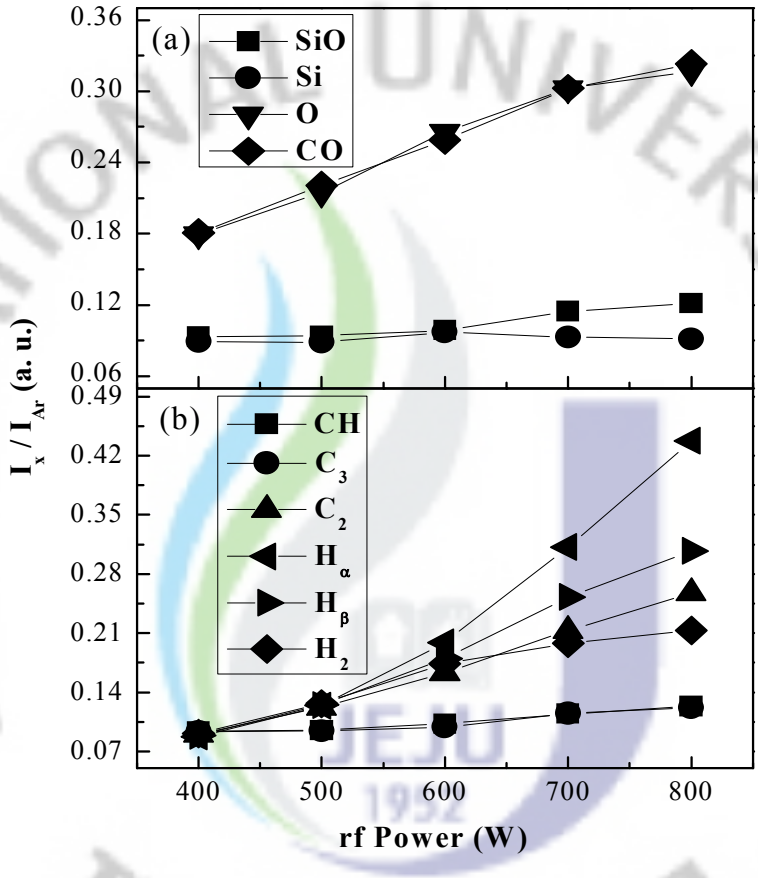

Fig. 16. Normalized emission line intensities as a function of rf power, (a) for the species SiO, Si, O and CO, and (b) for the species CH, C_3, C_2, H_α, H_β and H_2.

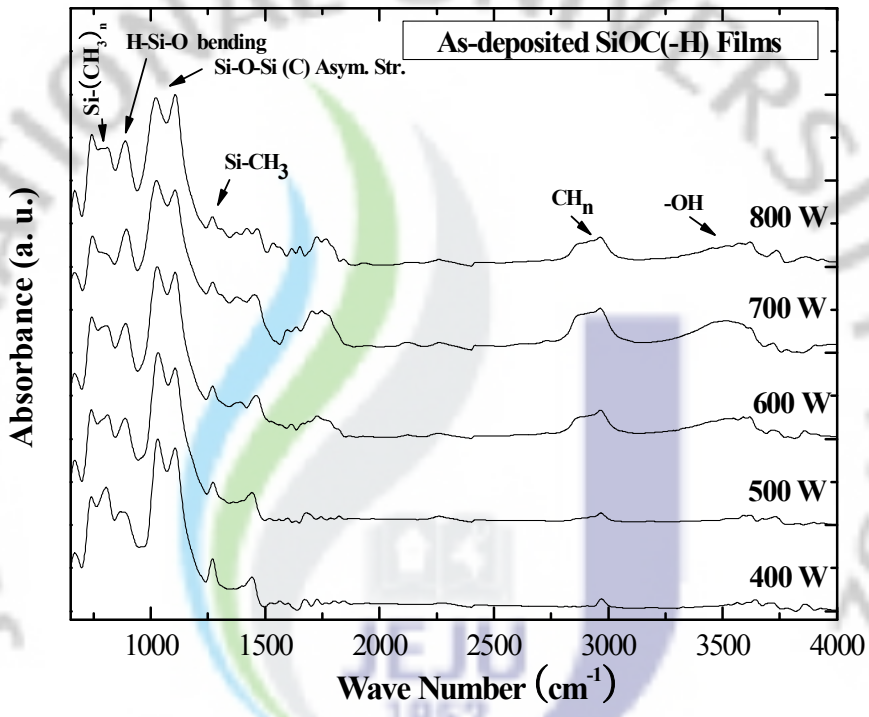

Fig. 17. FTIR spectra of the SiOC(-H) films deposited with different rf powers.

Si-O asymmetric stretching and the -CH_n bond in the wavelength region from 950 to 1250 cm^{-1} and 2800 to 3050 cm^{-1}, respectively for the SiOC(-H) film deposited with various rf powers. The broad Si-O-Si band between 950 and 1250 cm^{-1} can be resolved into four peaks. These peaks provide information about the composition of the Si-O-Si structure. The peaks at 1060, 1082, 1124 and 1170 cm^{-1} can be assigned to the Si-O-Si stretching mode, and ring, open and cage link stricture of the Si-O-C bonding modes, respectively. The presence of the cage link structure, which can generally be recognized in FTIR spectra by an absorbance peak around 1170 cm^{-1}, which is associated with the large angle Si-O-Si asymmetric stretch band, produces a lower film density [59]. As the rf power increases, the -CH_n peak area increases which is an indication of more carbon content in the SiOC(-H) film (see Fig. 18(a)). The -CH_n stretching band from 2800 to 3050 cm^{-1} consists of two or four components. The four peaks at 2850, 2877, 2910 and 2970 cm^{-1} can be assigned to $\nu^{s}C\text{-}H_2$, $\nu^{s}C\text{-}H_3$, $\nu^{a}C\text{-}H_2$ and $\nu^{a}C\text{-}H_3$, respectively. These peaks provide direct evidence of the presence of methyl groups in the Si-O-Si network [60]. The intensity of these peaks appear to become more pronounced with increasing rf power, indicating the higher carbon content of the SiOC(-H) film. Figure 18(b) shows the deconvoluted broad band structures from 700 to 900 cm^{-1} and the Si-CH_3 symmetrical bending band from 1240 to 1300 cm^{-1}. As shown in Fig. 18(b), at least five peaks are necessary to get a good deconvolution of the band. The peaks at 730, 773, 810, 861 and 897 cm^{-1}can be assigned to the coupling of the Si-C stretching and the CH_3 rocking modes in the Si-O-Si, Si-$(CH_3)_1$, Si-$(CH_3)_2$, Si-$(CH_3)_3$ and H-Si-O structures [60], respectively. The single peak at 1272 cm^{-1} over the region between 1240 and 1300 cm^{-1} corresponds to the Si-CH_3 rocking mode. As the rf power increases the absorption intensity of this peak is decreased. It is one of the characteristic peaks in the FTIR spectra for this DMDMS precursor. This decreasing trend of the Si-CH_3 bending mode with increasing rf power is different from that of our previously reported results [61].

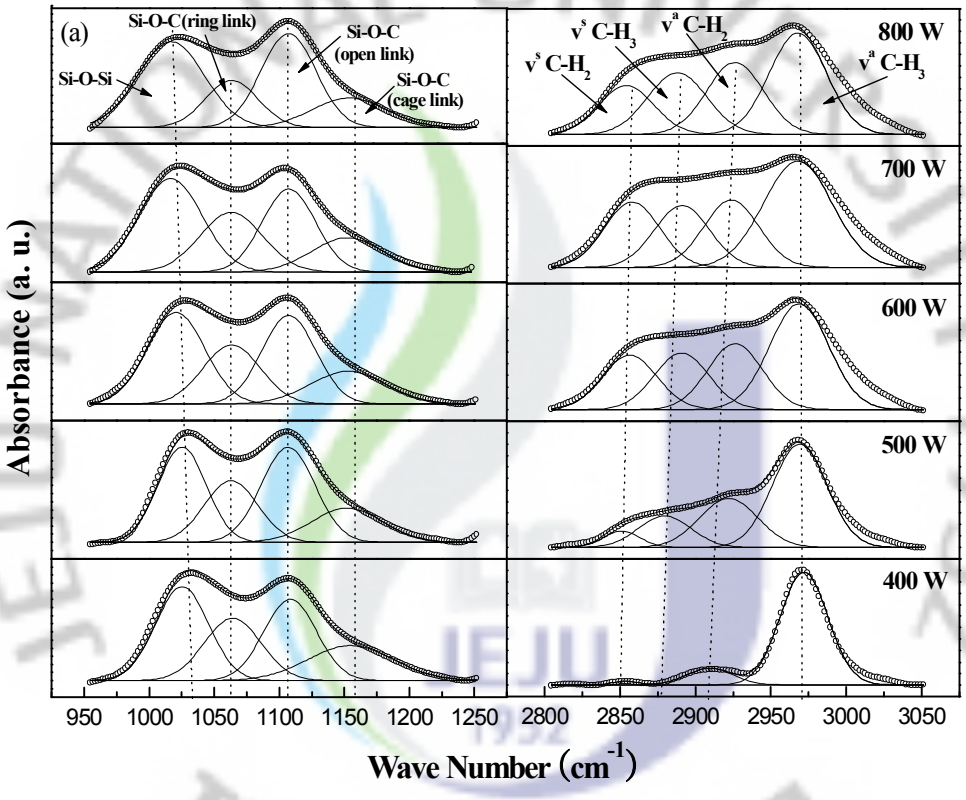

Fig. 18. Deconvoluted FTIR spectra of the SiOC(-H) films: (a) in the ranges from 950 to 1250 cm^{-1} and 2800 to 3050 cm^{-1}, and (b) in the ranges from 690 to 950 cm^{-1} and 1250 to 1300 cm^{-1}.

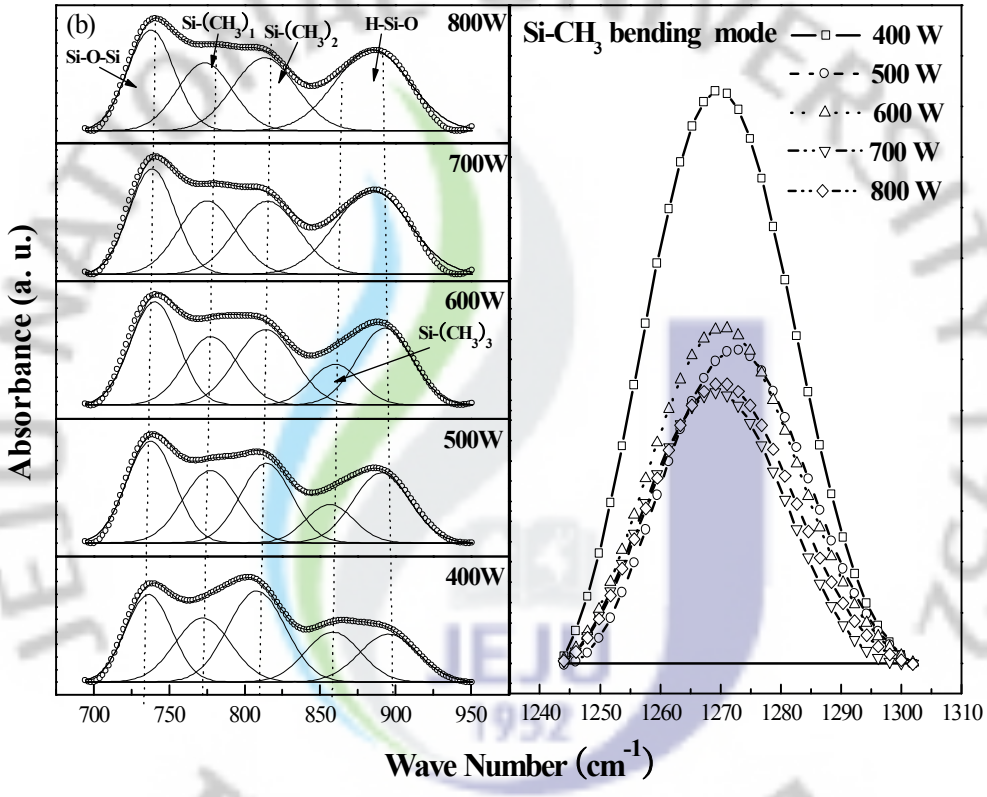

Figure 19 shows the relative carbon content due to the Si-CH_3 and -CH_n bands of the SiOC(-H) films as a function of rf power. The carbon content is deduced from the deconvoluted FTIR data [see Fig. 18(b)] in the wavelength regions from 690 to 950 cm^{-1} and 1250 to 1300 cm^{-1}. However, the absorption band corresponding to the region from 690 to 950 cm^{-1} remains almost similar for all the films deposited with different rf powers. On the other hand, for the region from 1250 to 1300 cm^{-1}, the absorption peak of the Si-CH_3 band decreased gradually with increasing rf power. The relative carbon content in the SiOC(-H) film decreases sharply with increasing rf power up to 700 W and then suddenly increase again for at an rf power of 800 W. Concurrently, the -CH_n stretching absorption increases rapidly up to an rf power of 700 W and then it decrease slightly for an rf power of 800 W. We can infer that the rf power strongly influences the bonding configuration of the SiOC(-H) film. The relative absorption area (%) of the Si-CH_3 group was found to decrease from 41 to 33% with an increase of rf power from 400 to 700 W. On the other hand, the absorption area (%) of the -CH_n related group was found to increase from 5 to 45% with an increase of rf power from 400 to 700 W. As a result of that, the apparent carbon content of the SiOC(-H) film remains to be increased with increasing rf power.

Further, we observed that the SiOC(-H) film deposited at higher rf powers (>700 W), the deposition rate is reduced and at the same time the relative carbon content is much lower compared to that of others. One likely reason for this phenomenon is that at powers higher than the power (700 W) at which the DMDMS precursor can be dissociated fully, it may be possible for CH_4, CO and CO_2 molecules due to break up of methyl radicals and diffused out the structure. There is clear evidence of this result in the FTIR data shown in Figs. 18(a) and (b).

Figure 20 shows the Si 2p, C 1s and O 1s electron orbital spectra of the SiOC(-H) film obtained with various rf power levels. The XPS narrow scan spectra were recorded and then deconvoluted by using Gaussian peaks, as shown in the figure. Figure 20(a) shows the Si 2p electron orbital spectra of each film. The Si 2p spectra

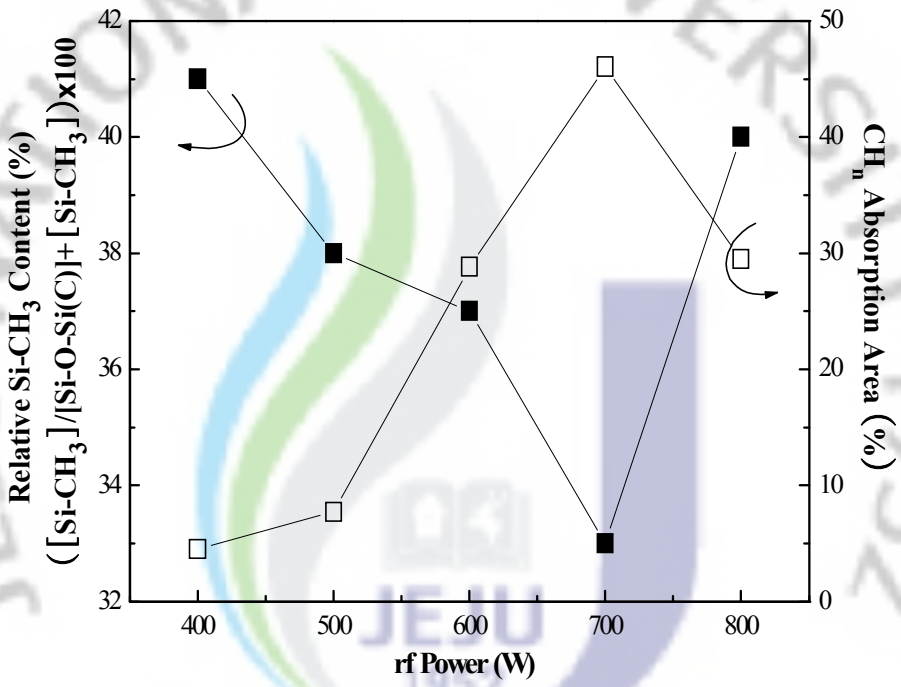

Fig. 19. Absorption area of Si-CH_3 and -CH_n bonds as a function of rf power.

can be deconvoluted into five peaks such as Si-C (99.6±0.1 eV), O-Si-CH_3 (100.5±0.1 eV eV), O_2-Si-$(CH_3)_2$ (101.6±0.1 eV), O_3-Si-$(CH_3)_3$ (102.7±0.1 eV) and Si-O_2 (103.6 eV) bonds [62,63]. As the rf power increases the integrated peak intensities of each bonding configuration becomes more prominent. This result conforms to the abundant presence of C atoms in the SiOC(-H) films. Figure 20(b) shows the C 1s electron orbital spectra for the SiOC(-H) films with different rf power levels. These C 1s spectra can be deconvoluted into six peaks. The results are assigned as follows: C(Si)4 (282.4±0.1 eV), Si-C (283.2±0.1 eV), C=C (283.8±0.1 eV), C-C/C-H (284.7±0.1 eV), C-O (285.6±0.1 eV), and C=O (286.8±0.1 eV) [64,65]. As the rf power increased, the precursor dissociated into smaller reactive species. Through this effect more -CH_3 and Si-CH_3 related groups become incorporated into the Si-O-Si network. These groups can have the ability to form different C bonding configurations such as Si-C, C-O, C-C, C-H, C=C and C=O during the polymerization process.

Figure 20(c) shows the O 1s electron orbital spectra of the SiOC(-H) films deposited at different rf power levels. These spectra can be decomposed into four components, namely, O-C (530.5±0.1 eV), SiC_xO_y (531.8±0.1 eV), O-Si (532.6±0.1 eV) and O-Si-O (533.7±0.1 eV) [62]. This result means that more carbon atoms are attached to the Si-O chain, thus forming an SiOC(-H) film. The XPS data is in good agreement with OES data, which is proof of the incorporation of carbon into the SiOC(-H) film.

Figure 21 shows the relative emission intensity ratios as a function of rf power. It is observed that the intensity ratio of $CH/(CH+H_\alpha+H_\beta)$ increases with increasing rf power whilst the intensity ratio of $(H_\alpha+H_\beta)/(CH+H_\alpha+H_\beta)$ decreases. This result means that the bulk plasma can be completely dissociated when the rf power is increased, giving rise to more Si-C related bonds in the SiOC(-H) film.

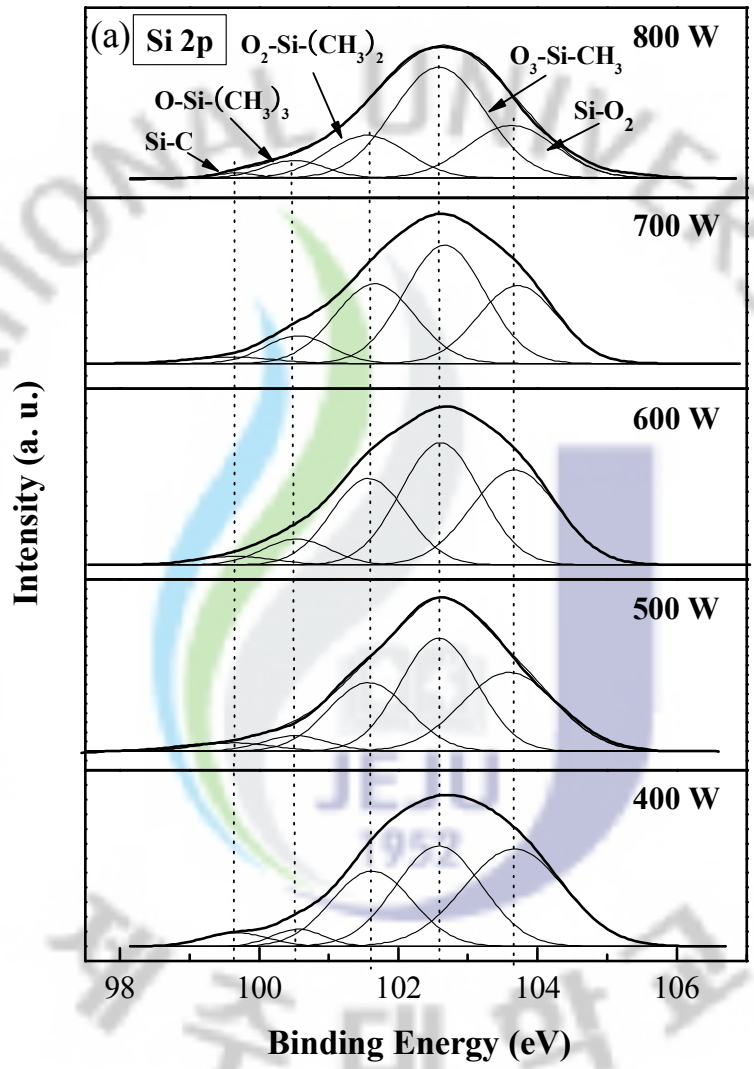

Fig. 20. XPS spectra of the SiOC(-H) films deposited with different rf powers: (a) Si 2p electron orbital, (b) C 1s electron orbital and (c) O 1s electron orbital.

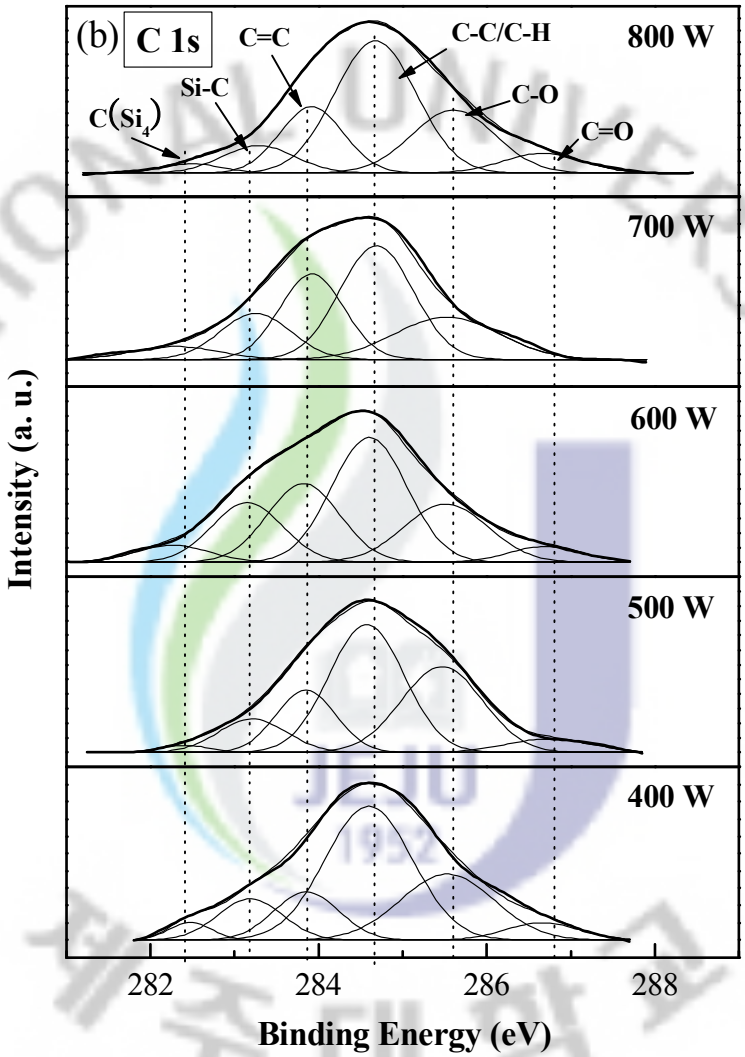

(continue)

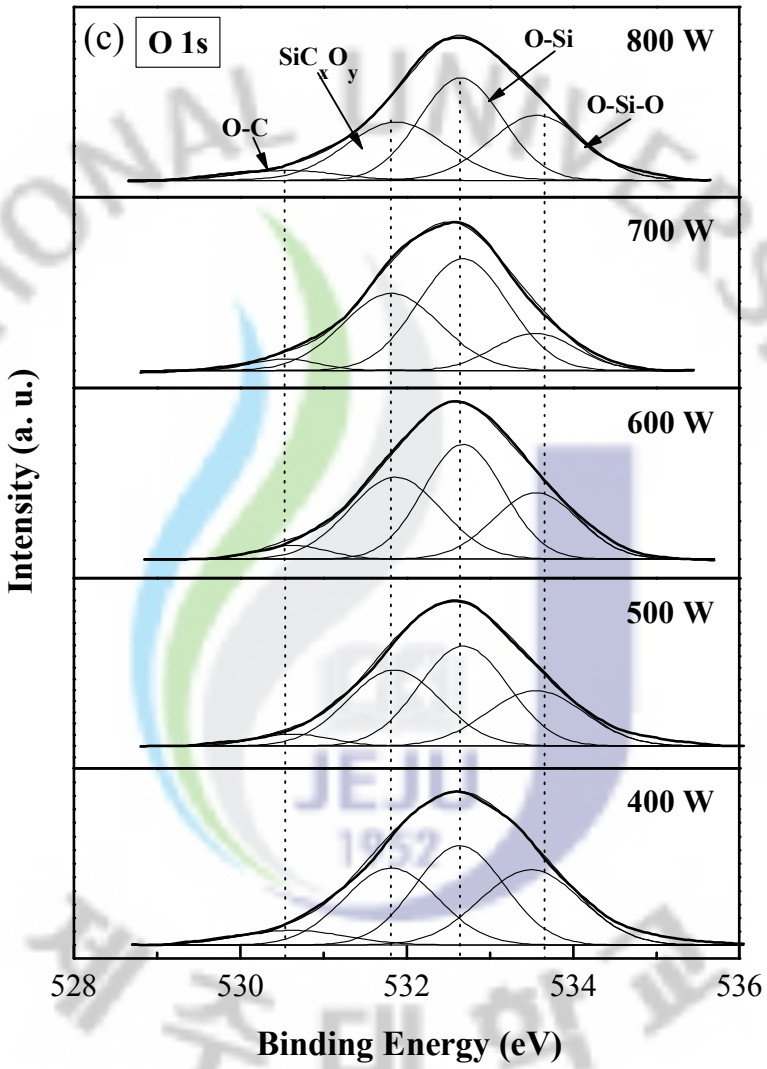

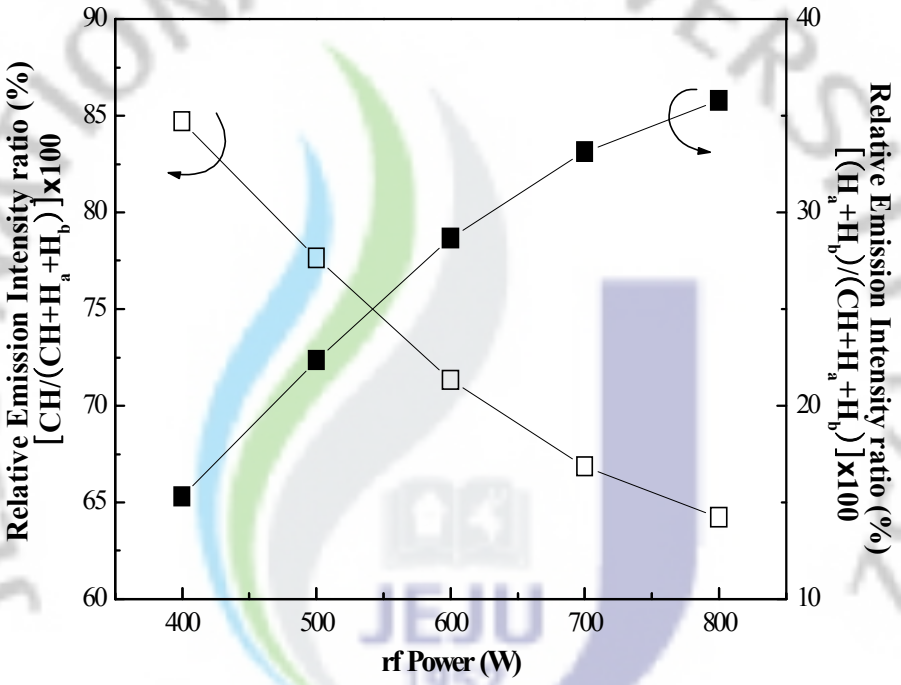

Fig. 21. Emission intensity ratios as a function of rf power.

Dielectric properties of the SiOC(-H) film depends on the bonding angle, the dipole moment and the polarizability. The dipole moment can be calculated from charge and bonding length, as expressed in equation

$$\mu = Qd = \delta e d. \tag{56}$$

where μ is dipole moment, Q is charge, d is bonding length, δ is ionic percent and e is elementary quantum of electricity. In order to investigate the dipole moment of the Si-O-C chain structure as a function of the bonding angle between Si-O and Si-C bonds, we used the following expression,

$$\mu_{Si-O-C} = \mu_{Si-O} + \mu_{Si-C}. \tag{57}$$

where μ_{Si-O} and μ_{Si-C} are the induced dipole moments of the Si-O and Si-C bonding molecules. The bonding lengths of Si-O of SiO_2 structure and Si-C bonds of SiC structure are 1.60 Å [66]. In carbon incorporated SiOC structure, the bonding length of Si-O bond increased to average 1.90 Å, the bonding length of Si-C bond decreased to average 1.85 Å. The ionic percent of Si-O and Si-C bonds are 0.08 and 0.07, respectively [67]. And then, the dipole moment of Si-O and Si-C bonds are 2.5×10^{-30} Cm and 2.0×10^{-30} Cm, respectively. The dipole moment usually reflects the difference between the electronegativities of the carbon and the oxygen atoms because the dipole moment of Si-O bond is large than that of Si-C bond. The bonding angle can be calculated from Eq. (58).

$$\bar{\nu} = \bar{\nu_0} \sin\left(\frac{\theta}{2}\right). \tag{58}$$

where θ is the bonding angle between the Si-O and the Si-C bonds. $\bar{\upsilon}$ is the wave

number for the thermal oxide (SiO_2), and $\overline{\upsilon_0}$ is experimentally obtained as the wave number of Si-O-C open link. Figure 22 shows the dipole moment of the SiOC(-H) films as a function of rf power. It is observed that the dipole moments is linearly decreased from 1.13×10^{-30} to 1.10×10^{-30} C·m as the rf power increased from 400 to 700 W. To compared with FTIR and XPS data, the dipole moment of the SiOC(-H) film was smaller than that of SiO_2 film and gradually decreased with increasing carbon content incorporated in the film [68]. Because the dipole moment of polyatomic molecules is the vector sum of bond moments, high-symmetry molecules can have a zero dipole moment because the vector sum of their bond moment is zero, even though they have very polar bonds (Si-O bonds). Since the structure of SiO_2 film and [SiO_4] tetrahedron is nearly symmetrical, its dipole moment was about zero. If one of oxygen atom in the [SiO_4] tetrahedral molecule is replaced by carbon, the vector sum of the bond moments will then be non-zero. This is because the dipole moment of SiOC is larger than that of SiO_2. However, the dipole moment of the [SiO_2C_2] tetrahedral molecule, which is formed by the substitution of two carbon atoms for two oxygen atoms in [SiO_4] tetrahedral molecule, is lower than that of the [SiO_3C] tetrahedral molecule. This result is explained by the difference in bond moments. Since the bond moment usually reflects the difference between the electronegativities of the two atoms, the bond moment of Si-O is larger than that of Si-CH_n. The increased number of Si-O bond replacements for Si-C bonds results in the reduction of the sum of bond moments in the molecular unit. Therefore, the drastic decrease in the dipolar polarization of the SiOC(-H) films with increasing carbon content is attributed to the reduction of the molar dipole moment as well as the dipole density [68].

Figure 23 shows the dipolar polarizability as a function of rf power. The value of the dipolar polarizability of the SiOC(-H) films deposited at different rf power was found to decreased from 1.02×10^{40} to 0.96×10^{40} Fm^2, respectively. From FTIR and XPS results, we can infer that the SiOC(-H) films with more -Si-CH_3 group have

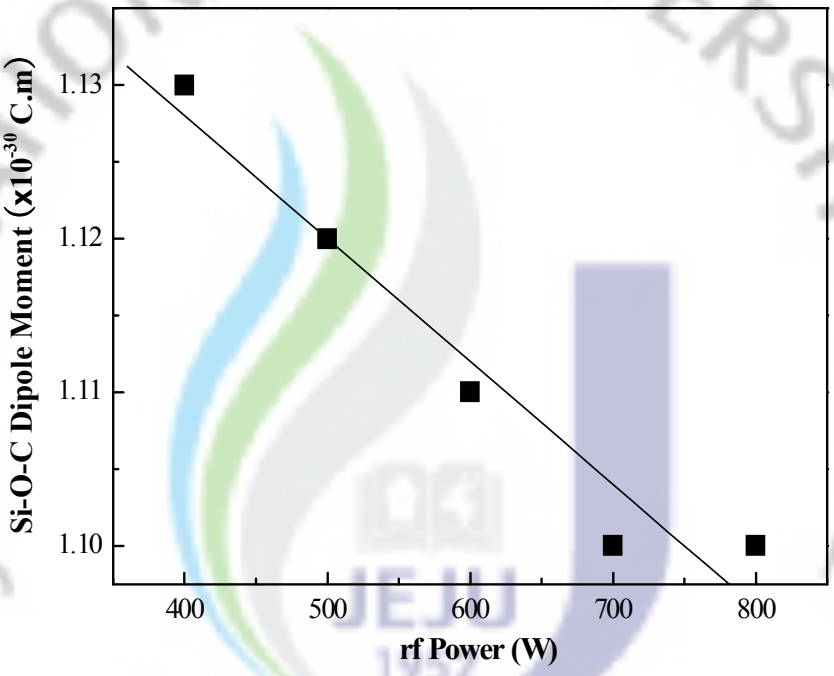

Fig. 22. Dipole moment of the SiOC(-H) films as a function of rf power.

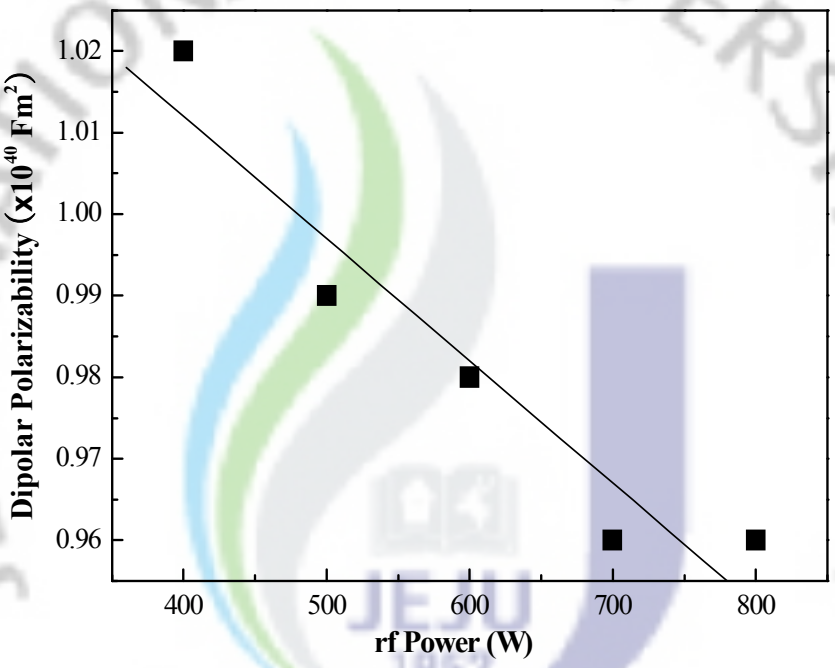

Fig. 23. The calculated the dipolar polarizability as a function of rf powers.

lower polarizability. D. shamiryan *et al.* [65] reported that materials with chemical bonds of lower polarizability then Si-O or lower density materials can be combined even lower *k* values, where some silica Si-O bonds have been replaced with less polar Si-C bonds . A more fundamental reduction can be achieved by using virtually all nonpolar bonds, such as C-C or C-H, for example, in materials like organic polymers. The addition of CH_3 not only introduces less polar bonds, but also creates additional free volume. Therefore SiOC(-H) films are constitutively porous, dielectric constant will be decreased.

Figure 24 shows the dielectric constant and refractive index of the SiOC(-H) film as a function of rf power. The values of the dielectric constant and the refractive index were found to decrease from 3.06 to 2.44 and 1.45 to 1.40, respectively, with an increase of rf power from 400 to 800 W (the lowest *k* value of 2.21 for an rf power of 700 W). However, the film deposited with an rf power of 800 W showed a slight increase in dielectric constant. From these results, It is found that the dielectric constant of the SiOC(-H) films is linearly proportional to the square of the refractive index, *n*. The value of n^2 was calculated to have decreased from 2.10 to 1.96 as a function of rf power. This result can be understood in terms of the fact that the dielectric constant is composed of electronic, ionic and dipolar components, and the electronic dielectric constant is proportional to the square of the refractive index. The decrease of the electronic dielectric constant in the SiOC(-H) film with increasing carbon contents is attributed to the reduction of the dipole moment as well as the film density. Therefore, the reduced electronic dielectric constant had a large influence on reducing the overall dielectric constant because that the electronic dielectric constant was responsible for more than 90% in the total dielectric constant [68]. In this study, a very drastic reduction of the dielectric constant value was obtained through an increase of rf power. One possible mechanism responsible for the decrease of the dielectric constant in the SiOC(-H) films is that the complete dissociation of the precursor molecule into smaller reactive species results in an abundant significant incorporation of carbon via the $-CH_3$ network into the films.

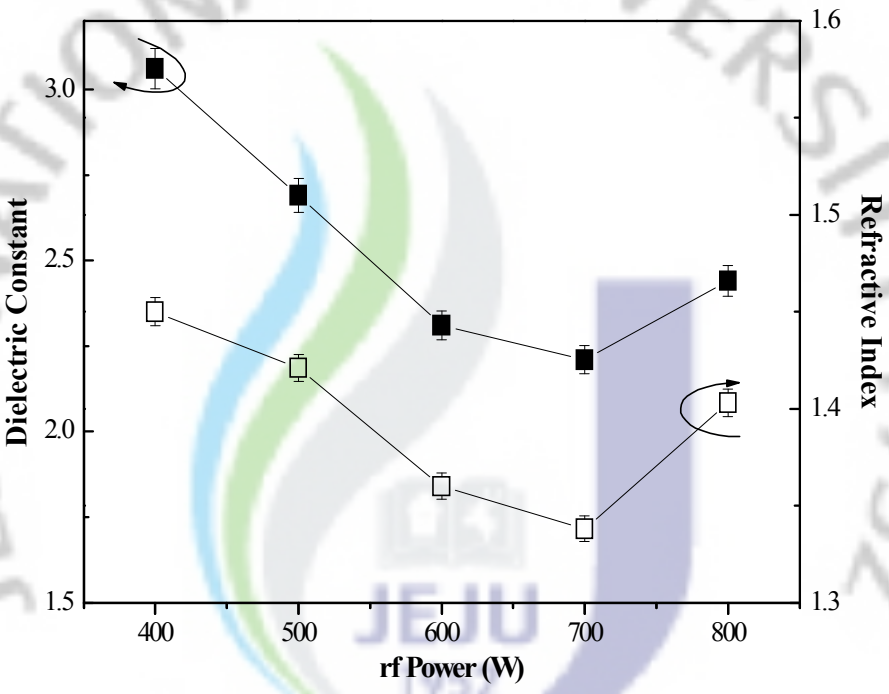

Fig. 24. Dielectric constant and refractive index of the SiOC(-H) films as a function of rf power.

Figure 25 shows the leakage current density of the SiOC(-H) films as a function of the rf power at 1 MV/cm. The leakage current density of the SiOC(-H) films decreased with increasing rf power. As the rf power was increased from 400 to 800 W, the leakage current density decreased from 5.6×10^{-8} to 3.7×10^{-9} A/cm^2, and there was no breakdown. This result indicated that the SiOC(-H) films exhibited the lower leakage current density as well as the higher breakdown field. The best leakage current density was obtained at an rf power of 700 W and was about 2.7×10^{-9} A/cm^2. This result indicates that the electrical properties of the SiOC(-H) films is strongly influenced by the rf power and the moderate rf power of 700 W is favorable for the achievement of improved electrical properties. However, the leakage current density increased slightly for the SiOC(-H) film deposited with an rf power of 800 W. This result is in good agreement with structural data as shown in Figs. 18 (a) and (b), which may be attributed to the break up of methyl radicals in the SiOC(-H) film at higher rf power. This effect implies that the SiOC(-H) films deposited at the higher rf power had a compact structure with homogenous layers which results in a lower leakage current density and a higher breakdown field.

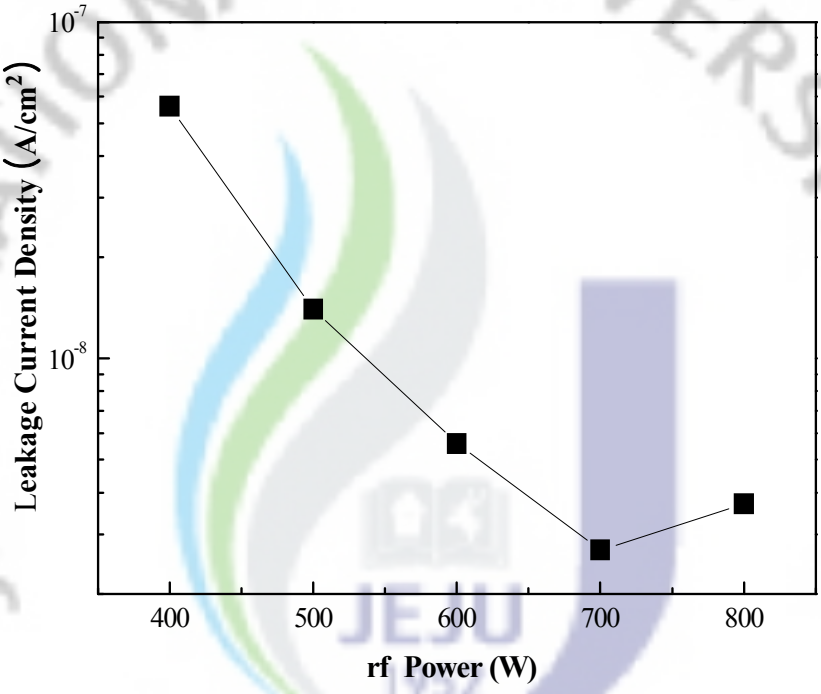

Fig. 25. The plot of leakage current density as a function of rf power measured at 1 MV/cm.

2. SiOC(-H) films deposited with various flow rate ratios of DMDMS/(DMDMS+O_2)

Figure 26 shows the deposition rate of the SiOC(-H) as a function of the precursor flow rate ratio. The deposition rate of the SiOC(-H) films was found to increase with O_2 flow rate. The decomposition of the DMDMS precursor is efficient compared to that of O_2, which the DMDMS precursor consists of the -CH_3 and the -O-CH_3 groups. Hence, reactive oxygen radicals are expected to be formed first and to be adsorbed at the substrate surface. Oxygen radicals also activate and dissociate the DMDMS precursor into highly reactive species that give rise to Si-C bonds. Finally, oxygen radicals selectively oxidize the deposited Si-C bonds and form Si-O bonds on the substrate. This selective oxidation highly depends on the oxygen radical density. Therefore, a higher O_2 flow rate leads to a larger oxygen radical concentration, which results in a higher deposition rate [69].

Figure 27 shows the FTIR absorption spectra from 700 to 4000 cm^{-1} for SiOC(-H) films deposited with various flow rate ratios from 50 to 100%. The spectrum consists of several bands or groups of bands occurring over the entire spectral range, and it is similar to Fig. 17. In order to understand the bonding configurations of the Si-O-Si, Si-O-C, Si-CH_3 and -CH_3 related structures, we deconvoluted the FTIR spectra in their respective regions as illustrated in Fig. 28. Figure 28(a) shows the deconvoluted spectra of the Si-O stretching bond in the region from 1000 to 1250 cm^{-1} for the SiOC(-H) film deposited with various flow rate ratios. This figure reveals four bands with peaks at 1060, 1082, 1124 and 1170 cm^{-1}, which can be assigned to the Si-O-Si stretching mode and to the ring, open and cage links of the Si-O-C bonding modes, respectively. As the flow rate is increased, the absorption peaks corresponding to Si-O-Si and Si-O-C bonds become sharper, At the same time, the former peak shifts towards a lower wave number region, i.e. a red shift, as shown in Fig. 28(a).

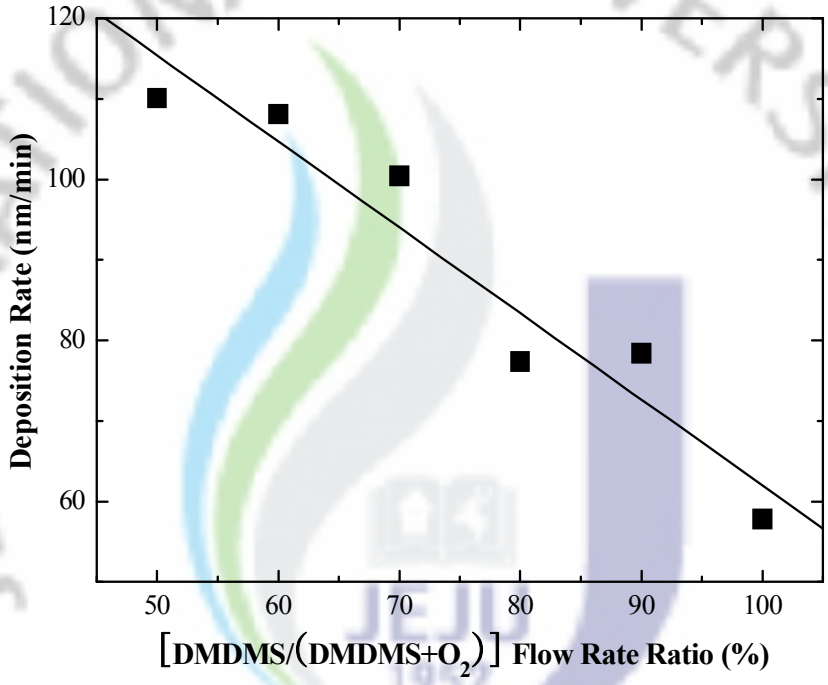

Fig.26. Deposition rate of the SiOC(-H) films as a function of the precursor flow rate ratio.

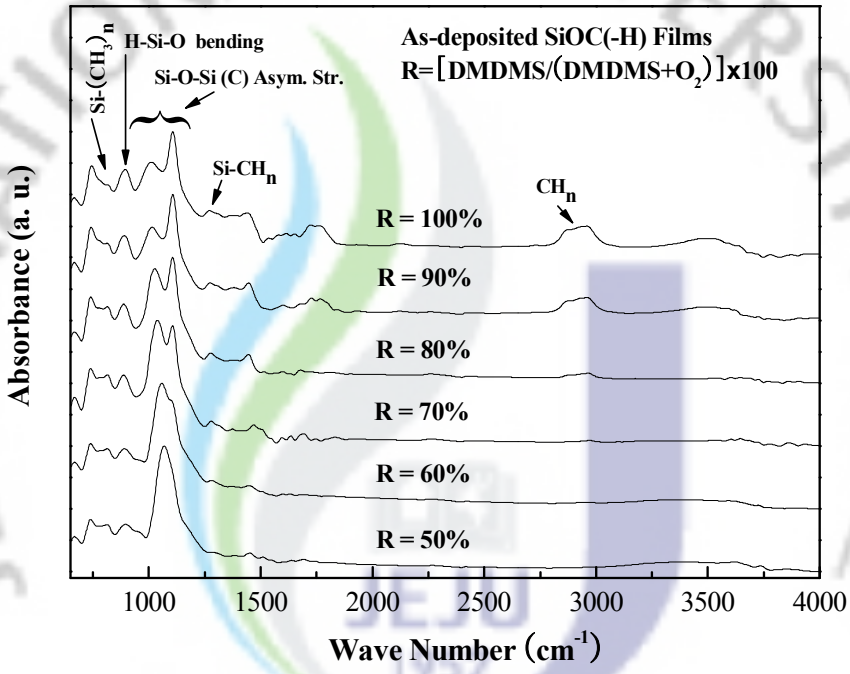

Fig. 27. FTIR spectra of the SiOC(-H) films deposited with various flow rate ratios.

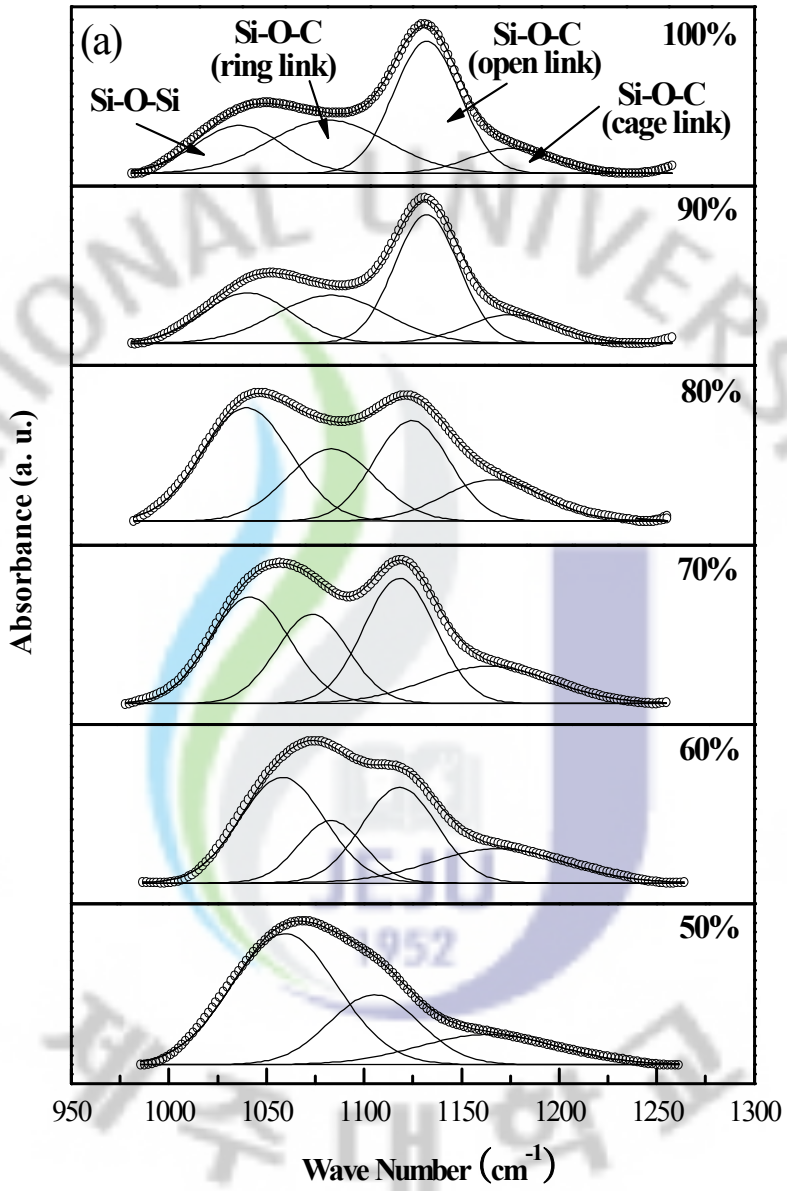

Fig. 28. Deconvoluted FTIR spectra of the SiOC(-H) film with various flow rate ratios: (a) in the region from 1000 to 1250 cm^{-1}, (b) in the region from 700 to 950 $cm^{-1}$and (c) in the region from 2750 to 3050 cm^{-1}.

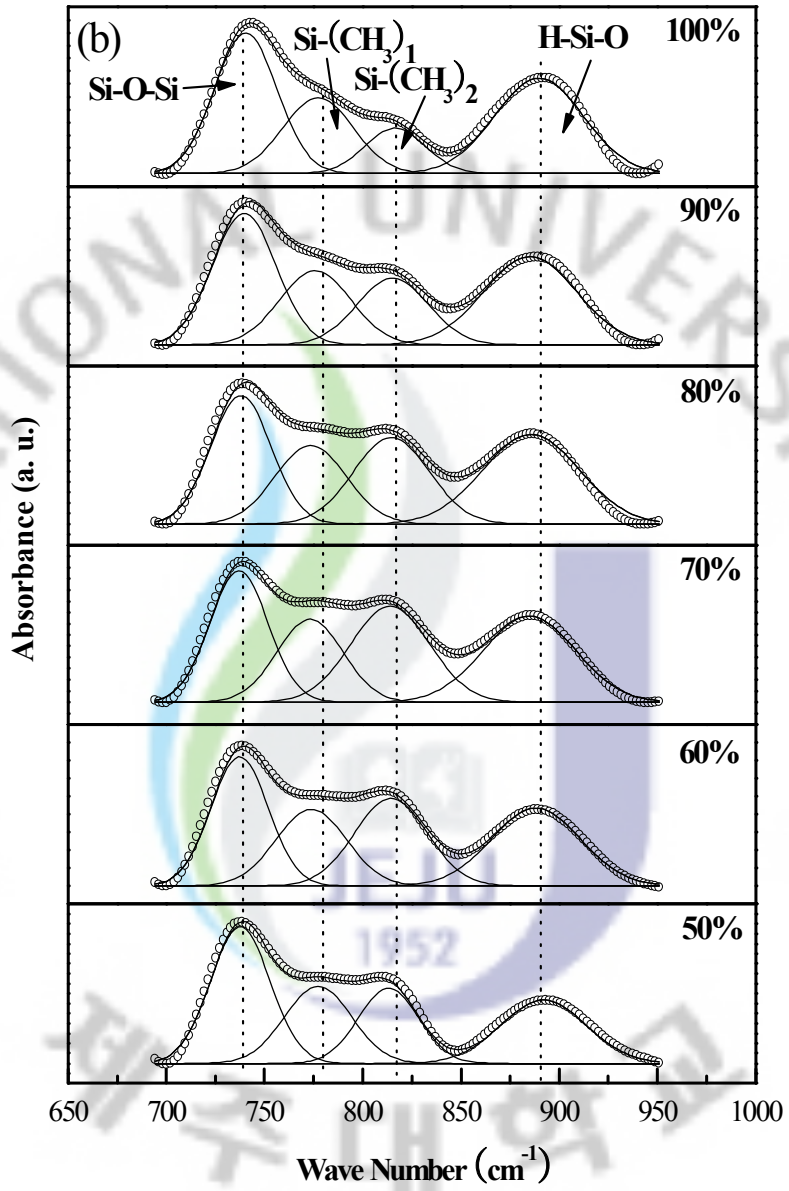

(continue)

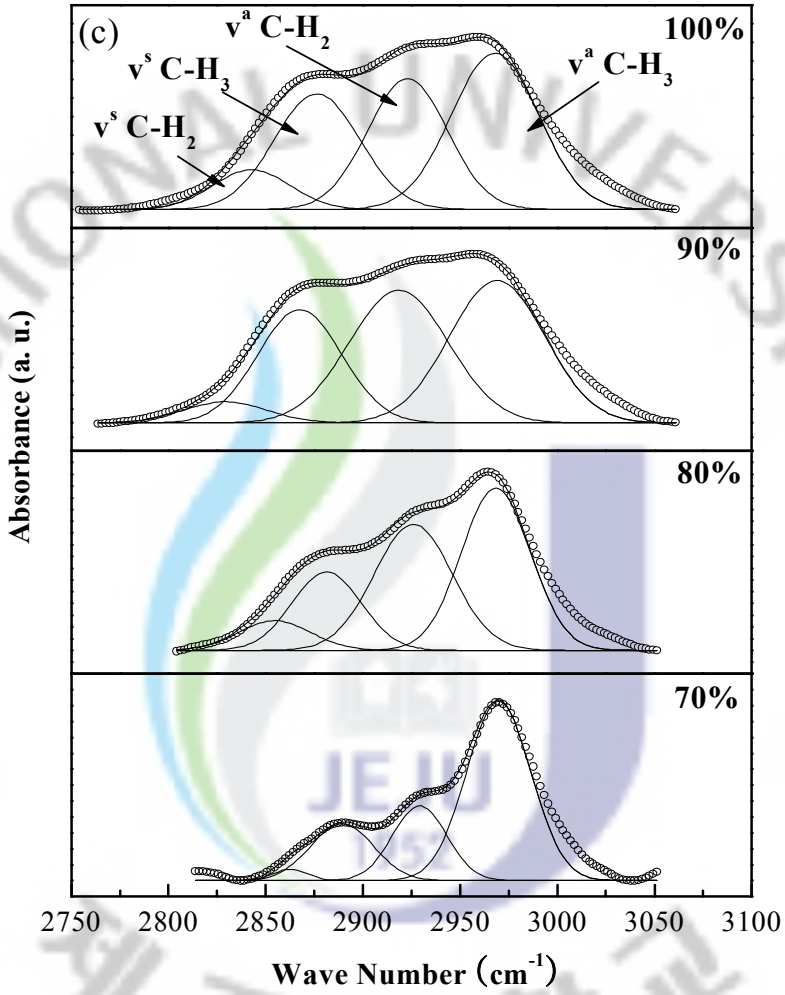

This kind of frequency shift in the FTIR spectra can be related to changes in the bonding characteristics [43]. This result shows that an increase in the DMDMS precursor flow rate gives rise to a structural rearrangement by adding more carbon atoms in the Si-O-Si network chain during the formation of the SiOC(-H) film. The cage-link structures of Si-O-C are believed to be able to produce a nanoporous structure, which results in a lower film density and, hence, a low dielectric constant [45]. Figure 28(b) shows the deconvoluted spectra of the Si-CH_3 rocking modes in a region from 700 to 950 cm^{-1}, which consists of four components. The peaks at 740, 780, 821 and 890 cm^{-1} can be assigned to the Si-O-Si stretching, Si-$(CH_3)_1$, Si-$(CH_3)_2$ and H-Si-O modes in the Si-CH_3 structure. There were no noticeable changes and the peak positions appeared to be almost the same for all the samples. Figure 28(c) shows the deconvoluted spectra of the -CH_3 related modes in the region from 2825 to 3050 cm^{-1} for the SiOC(-H) films with flow rate ratios from 70 to 100%, which were decomposed into four peaks. The integrated peak area increased with the flow rate ratio and more pronounced absorption peaks appeared.

Figure 29(a) shows the XPS narrow scan spectra of Si 2p, C 1s and O 1s electron orbital of the SiOC(-H) film obtained with various flow rate ratios. We observed that the peak intensities of the Si 2p and the O 1s spectra decreased with increasing flow rate ratio whereas the intensity of the C 1s spectrum increased. When the DMDMS flow rate increases, the Si 2p peak shifts to lower binding energy while the C 1s and the O 1s peaks remain almost constant. The Si 2p peak shift mainly results from the different electronegativities of silicon, carbon and oxygen. To understand the bonding configuration in the SiOC(-H) films further, we deconvoluted the XPS narrow scan spectra of the Si 2p and the C 1s peaks by fitting the data with a number of Gaussian peaks. Figure 29(b) shows the curve fitting of the Si 2p core level of each film. The Si 2p spectra can be deconvoluted into four or five peaks, such as Si-C (99.4±0.1 eV), O-Si-$(CH_3)_3$ (100.4±0.1 eV), O_2-Si-$(CH_3)_2$ (101.6±0.1 eV), O_3-Si-CH_3 (102.8±0.1 eV) and Si-O_2 (103.6 eV) [59,60].

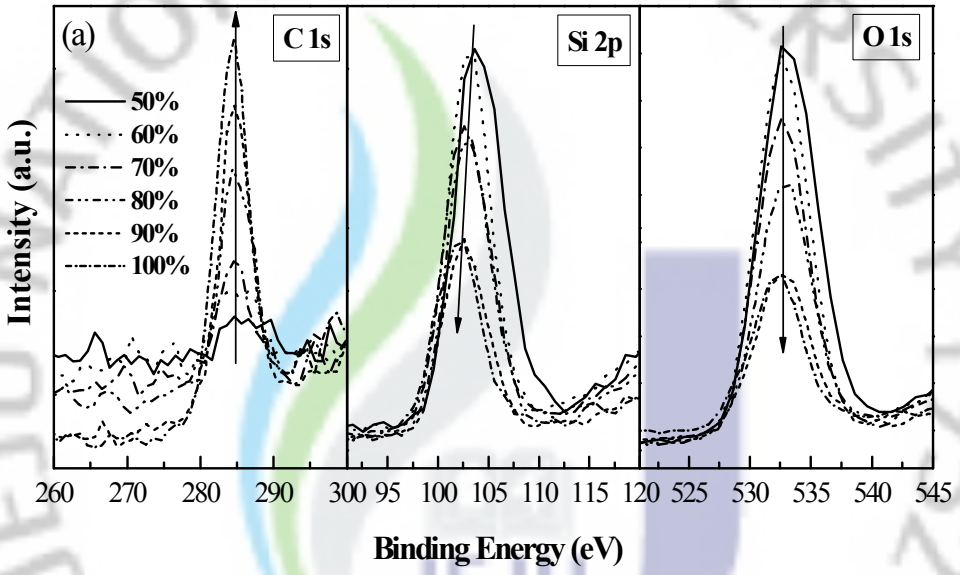

Fig. 29. XPS spectra of the SiOC(-H) films: (a) Si 2p, C 1s and O 1s electron orbital spectra for films various flow rate ratios, (b) deconvoluted Si 2p spectra and (c) deconvoluted C 1s spectra.

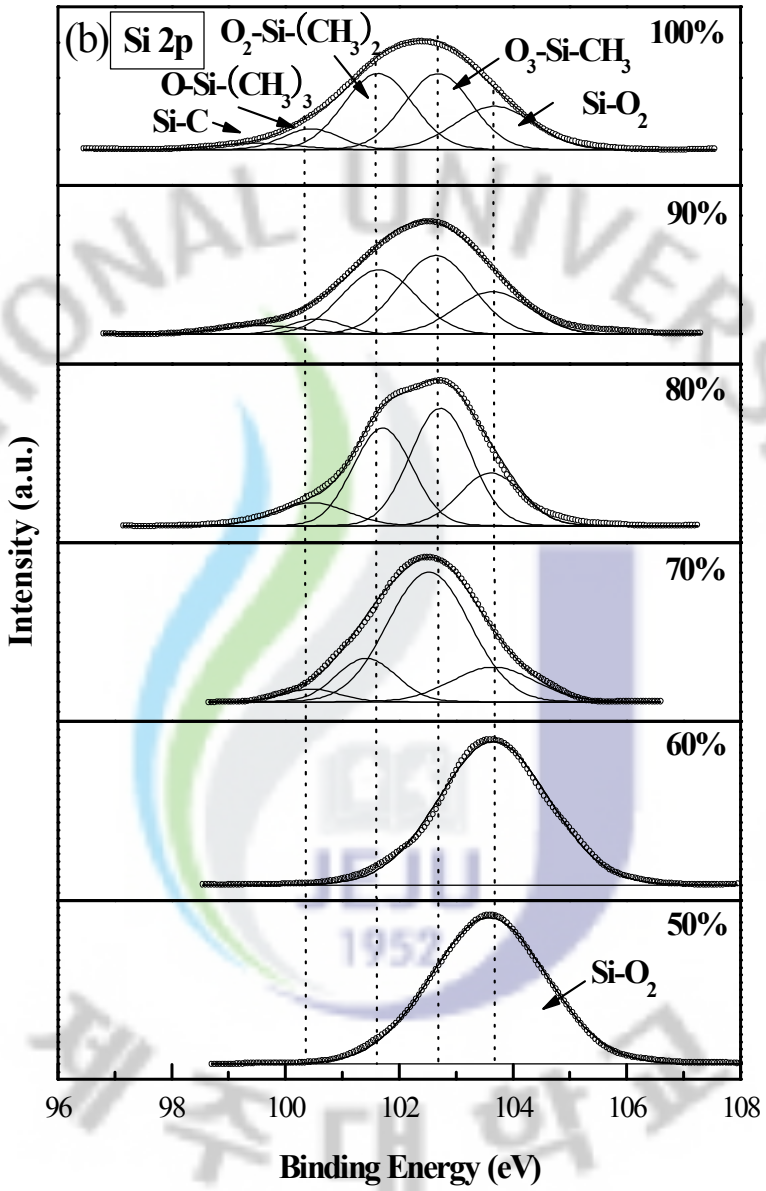

(continue)

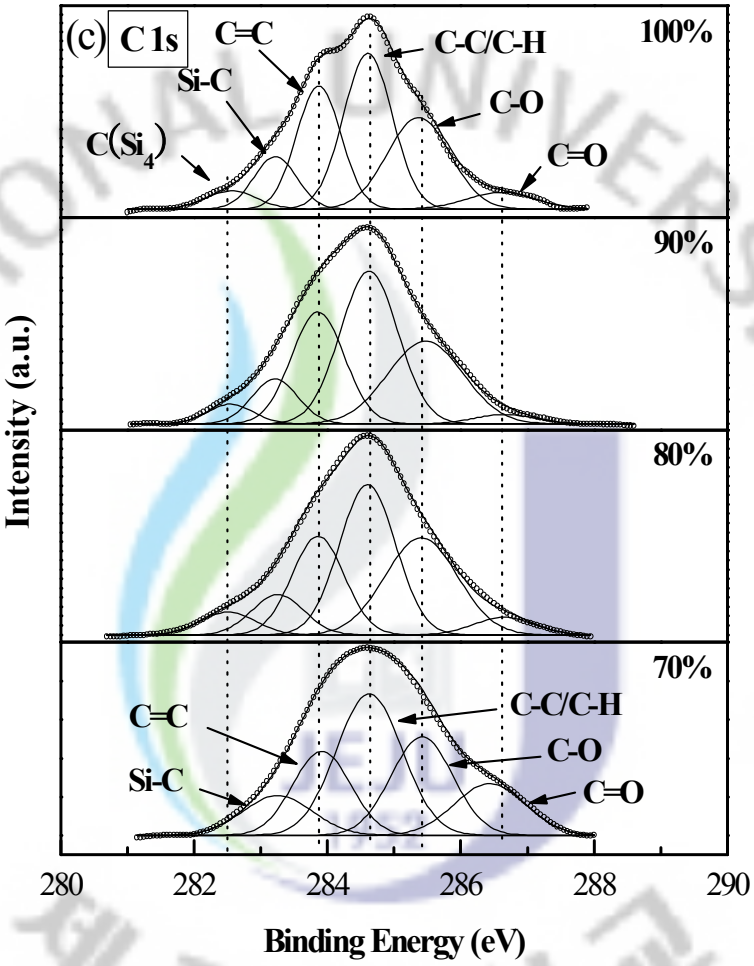

As shown in Fig. 29(b), the SiOC(-H) film with flow ratios of 50 and 60% are almost like the Si-O_2 film structure as the flow rate ratio was increased, more C atoms were incorporated into the Si-O-Si network, which resulted in a chemical shift towards lower binding energy. This result conforms the abundant presence of C atoms in the SiOC(-H) films. Figure 29(c) shows the C 1s electron orbital spectra for the SiOC(-H) films with flow rate ratios of 70 to 100%. As shown in Fig. 29(a), the intensity of the carbon content is very low for the films with flow rate ratios of 50 and 60%. These C 1s spectra can be deconvoluted into six peaks, except for the film with a 70% flow rate ratio. The film with the flow rate ratio of 70% can be decomposed into only five peaks, in which the C(Si)4 peak was absent. The fitted results are assigned as follows: $C(Si)_4$ (282.5±0.1 eV), Si-C (283.4±0.1 eV), C=C (283.9±0.1 eV), C-C/C-H (284.6±0.1 eV), C-O (285.4±0.1 eV) and C=O (286.7±0.1 eV) [59,60]. As the flow rate ratio was increased, more -CH_3 and Si-CH_3 groups were incorporated in the Si-O-Si network and they had the ability to form different C bonding configurations, such as C-O, C-C, C-H, C=C and C=O film. To compared with Fig. 20, the Si 2p electron orbital spectra is a different binding energy, and C 1s and O 1s electron orbital spectra is very similar binding energy and bonding modes. Figure 30 shows the dipole moment of the SiOC(-H) films as a function of rf power. It is observed that the dipole moments decreased linearly from 1.13×10^{-30} to 1.07×10^{-30} C·m as the precursor flow rate increased from 50 to 100%. As the DMDMS/O_2 flow rate ratio was increased from 50 to 100%, the dipolar polarizability decreased from 1.02×10^{40} to 0.91×10^{40} Fm^2 as shown in Fig. 31. This result suggests that the dipolar polarizability is much lower than that of other polarizability component. It is well known that the values of the dipolar dielectric constant is nearly zero because the dipolar polarizability on the SiOC bonding structure is distributed randomly in the SiOC(-H) film [68]. Therefore, the influence of the dipolar dielectric constant can be neglected for low-*k* dielectrics, whereas high-*k* dielectrics have a dominant dipolar polarizability [70].

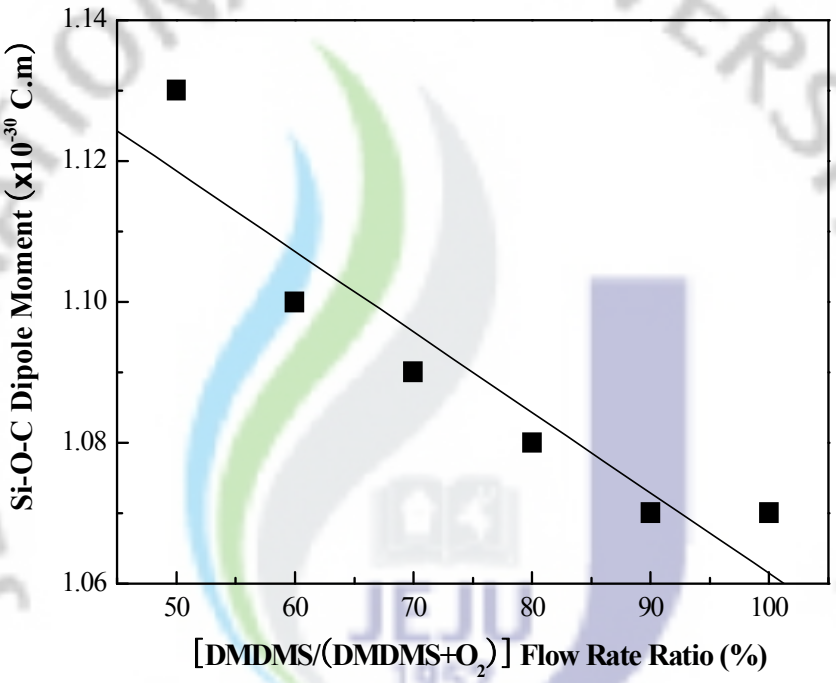

Fig. 30. Dipole moment of the SiOC(-H) films as a function of precursor flow rate ratio.

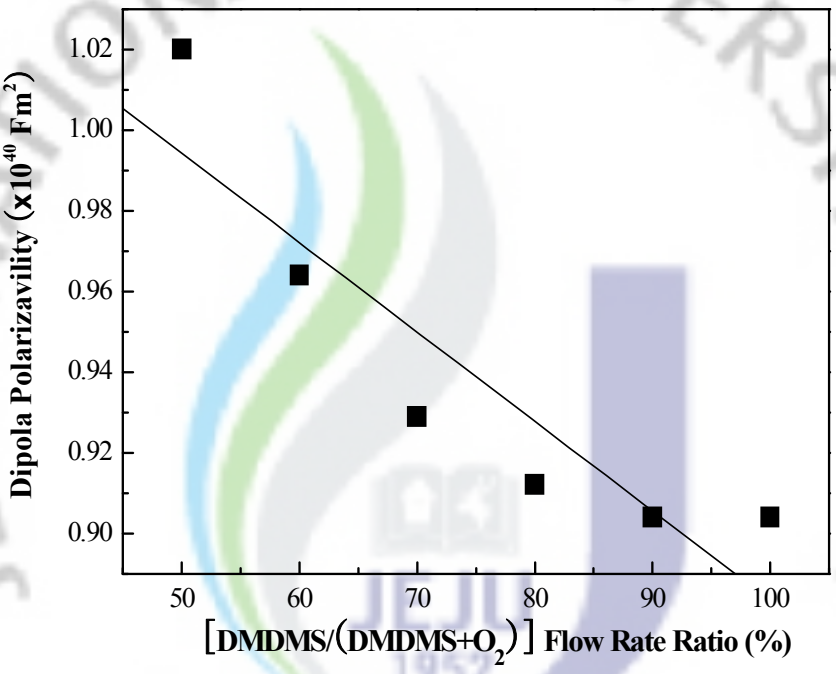

Fig. 31. The calculated the dipolar polarizability as a function of the precursor flow rate ratio.

Figure 32 shows the dielectric constant and refractive index of the SiOC(-H) film as a function of flow rate ratio. The values of the dielectric constant and the refractive index were found to decrease from 3.83 to 2.13 and 1.44 to 1.36, respectively, with an increase of flow rate ratio from 50 to 100% (the lowest k value of 2.13 for a flow rate ratio of 100%). Furthermore, the value of n^2 was calculated to have decreased from 2.07 to 1.85 as a function of the flow rate ratio. The tendency related with $k \propto n^2$ to the dielectric constant with various flow rate ratio. From this result, it is clearly observed that very drastic reductions in the dielectric constant value were obtained as the flow rate ratio was increased.

Figure 33 shows the leakage current density as a function of the precursor flow rate ratio. The leakage current density was measured at 1 MV/cm from the I-V characteristics of the SiOC(-H) films. As the DMDMS/O_2 flow rate ratio was increased from 50 to 100%, the leakage current density decreased from 3.8×10^{-6} to 6.3×10^{-9} A/cm^2, and there was no breakdown. As observed from the I-V characteristics, the SiOC(-H) film prepared with a 50% flow rate ratio broke down at 2.5 MV/cm and none of the other films broke down. The breakdown strength increased with increasing DMDMS/O_2 ratio. From the FTIR and XPS analyses, this result indicates that the electrical properties of the SiOC(-H) film are strongly influenced due to the ratio of the Si-O-Si to Si-O-C bonds present, which can be suitably modified by an appropriate choice flow rate ratio for the precursors during the preparation of the SiOC(-H) thin films.

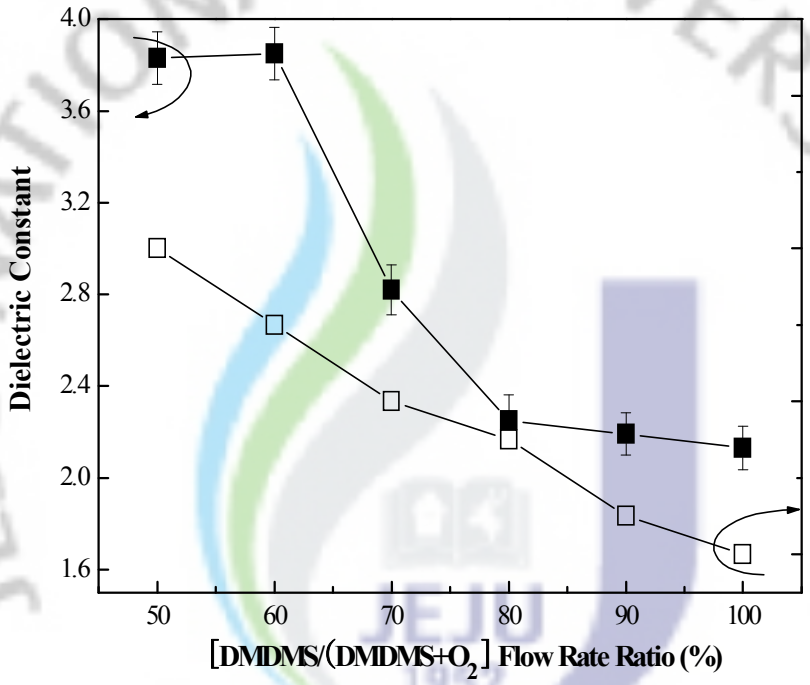

Fig. 32. Dielectric constant and refractive index of the SiOC(-H) films as a function of the precursor flow rate ratio.

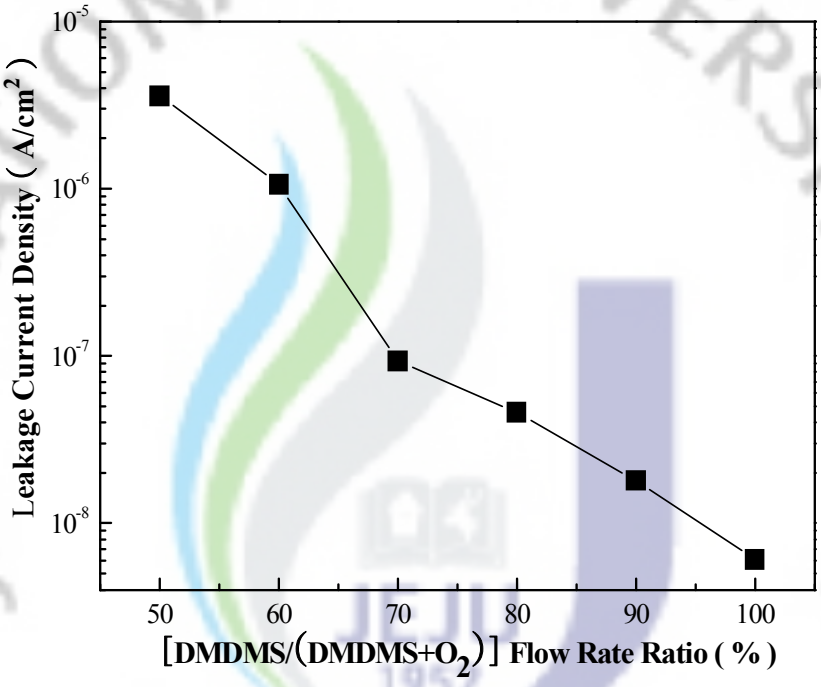

Fig. 33. Leakage current density measured at 1 MV/cm as a function of the precursor flow rate ratio.

3. SiOC(-H) films deposited at various substrate temperatures

Figure 34 shows the deposition rate of the SiOC(-H) film as a function of the substrate temperature. The deposition rate of the SiOC(-H) film decreased gradually with increasing substrate temperature. This result indicated that at high temperatures the Si-O bond has a larger tendency to be adsorbed on to the growing film than does the Si-C bond.

Figure 35 shows the FTIR spectra of the SiOC(-H) films deposited at various substrate temperatures. The characteristic band of the SiOC(-H) film showed absorption bands due to Si-O-Si (around 1040 cm^{-1}), Si-O-C (around 1106 cm^{-1}), $Si-CH_3$ (around 800 and 950 cm^{-1}; 1250 and 1300 cm^{-1}) and -OH (3700-3800 cm^{-1}) in addition to those of the Si substrate. There is a shoulder at about 1160 cm^{-1} in all the absorption spectra, which is assigned to a broad Si-O-C peak, and corresponds to the Si-O-C cage-link structure, resulting in a more porous structure in the SiOC(-H) film [43,45]. This spectrum is very similar to the FTIR absorption spectra of the SiOC(-H) films with various rf power and flow rate ratios.

As the substrate temperature increased, the intensity of the $Si-CH_3$ bond decreased, demonstrating that more oxygen atoms are incorporated into the Si-O-C ring-link network. The precursors are dissociated into highly reactive species that form the SiOC(-H) films with clearly separated peaks in the Si-O-Si and the Si-O-C absorbance bands. With increasing substrate temperature, the Si-O-Si peak becomes stronger due to rearrangement of the bonding configuration. It is one of the characteristic peaks of the infrared spectrum of the SiOC(-H) film. The broad band spectra from 950 to 1250 cm^{-1} consists of overlapping vibration modes from various bond structures, and the line shape of the film deposited at substrate temperature of 300 °C than that other results. In order to understand the bonding configuration of the SiOC(-H) films, we deconvoluted the FTIR spectra into its four constituents, as shown in Fig. 36 The bands with peaks centered at 1021, 1045, 1106 and 1160 cm^{-1}

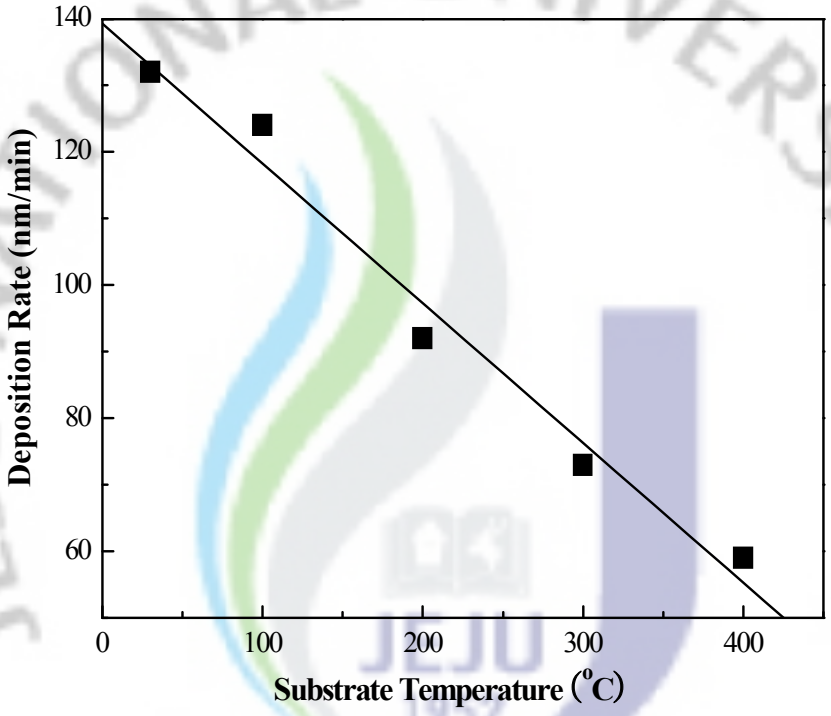

Fig. 34. Deposition rate of the SiOC(-H) films prepared with different substrate temperatures.

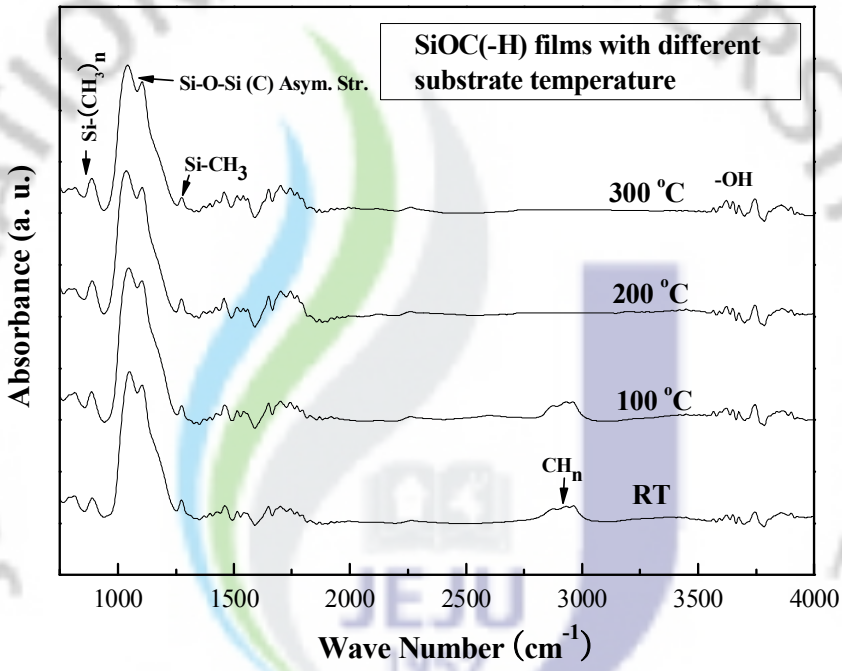

Fig. 35. FTIR spectra of as-deposited SiOC(-H) films with different substrate temperatures.

are assigned to the Si-O-Si stretching vibration, Si-O-C ring-link, open-link and cage-link structures, respectively. From this deconvoluted data, the relative absorption area of each bonding structure was deduced.

Figure 37 shows the relative absorption areas of the bonding structures in the SiOC(-H) films as a function of substrate temperature. This result shows that the Si-O-C cage-link mode remains almost constant (about 24%) whereas the Si-O-C ring-link structure decreased (from 25.3 to 16.7%) with increasing substrate temperature. The Si-O-C open-link structure decreased (from 28.6 to 21.7%) while that of the Si-O-Si stretching mode was increased (from 29.3 to 38.5%) with an increase of substrate temperature.

Figure 38 shows the relative carbon and Si-O-C(Si) content present in the SiOC(-H) film as a function of the substrate temperature. The relative carbon content is calculated by the following equation normalized to the peak height of the Si-O-Si stretch mode in the FTIR spectra [71]. The relative carbon content (%)=[A_c / (A_o+A_c)]×100%, where A_c and A_o are the absorption peak areas for the Si-CH_3 stretching mode (from 800 to 950 cm^{-1} and from 1250 to 1300 cm^{-1}) and the absorption peak area of Si-O-Si (from 900 to 1250 cm^{-1}), respectively. The relative content of carbon atoms decreased from 11.85 to 8.5% as the substrate temperature increased from room temperature to 300 °C. However, the Si-O-Si stretching mode increases with increasing substrate temperature. This effect is attributed to the lower carbon concentration due to the Si-CH_3 bonds being broken at elevated substrate temperatures, which gives rise to an increased dielectric constant. This can be explained by two factors: a decrease in the number of voids and an increased ionic polarization caused by the decreased number of Si-CH_3 bonds [71]. Therefore, at higher substrate temperatures, the weaker Si-CH_3 and C-H bonds leave the films with a lower concentration of these bonds and the SiOC(-H) films become more oxygen rich.

In order to understand the bonding configurations of the SiOC(-H) films in detail, XPS analysis was further employed. Figure 39(a), (b) and (c) shows the XPS narrow

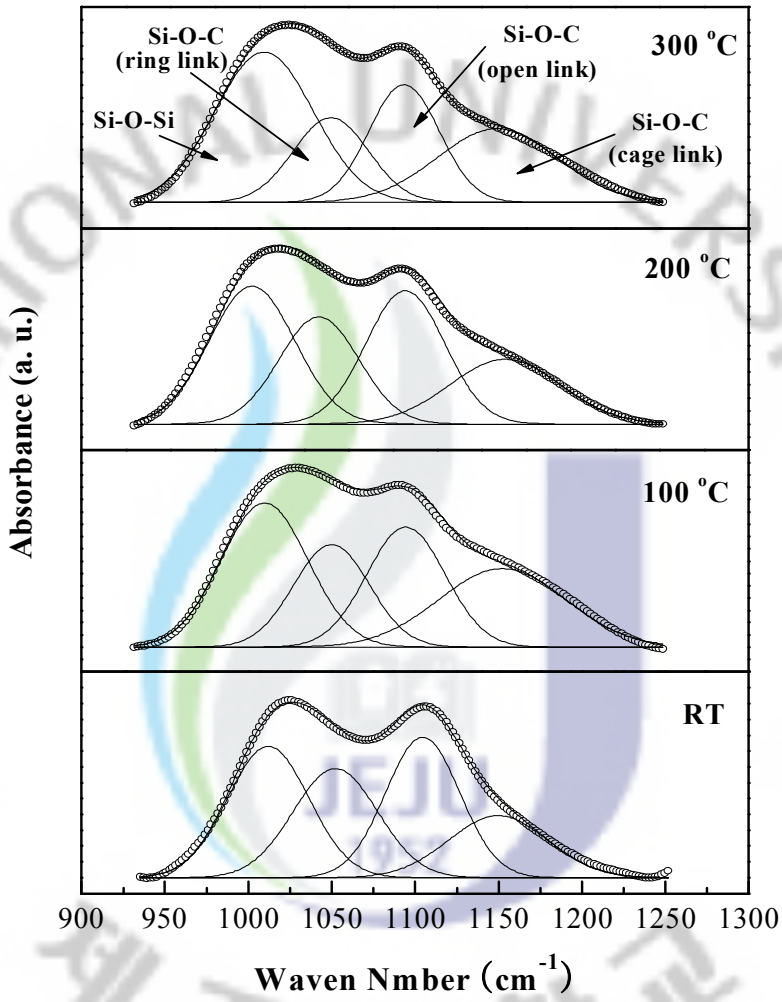

Fig. 36. Deconvolution of FTIR spectra of as-deposited SiOC(-H) films with different substrate temperatures between the wave number region of 950-1250 cm^{-1}.

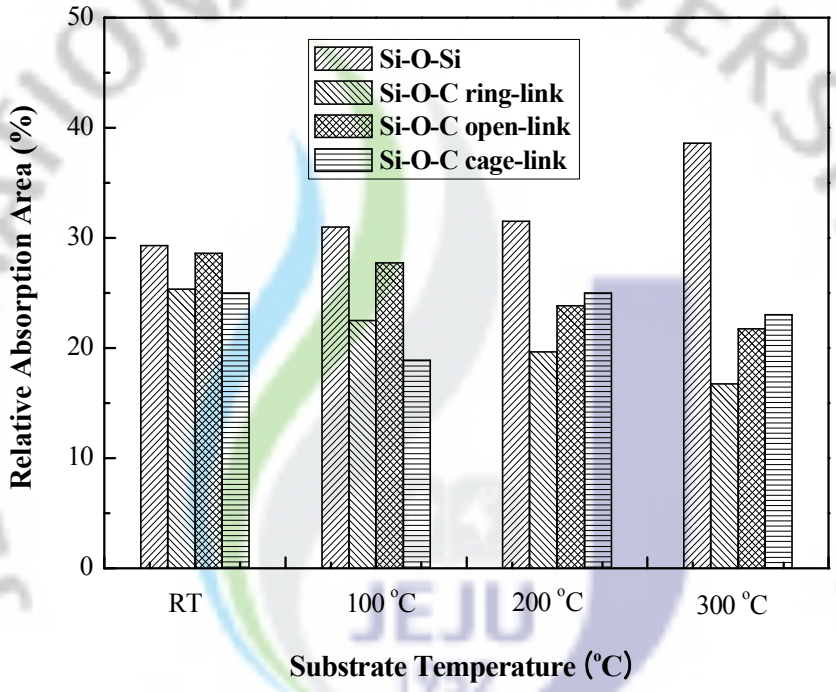

Fig. 37. Relative absorption area of Si-O-Si stretching, Si-O-C ring-link, Si-O-C open-link and Si-O-C cage-link structure as a function of substrate temperatures.

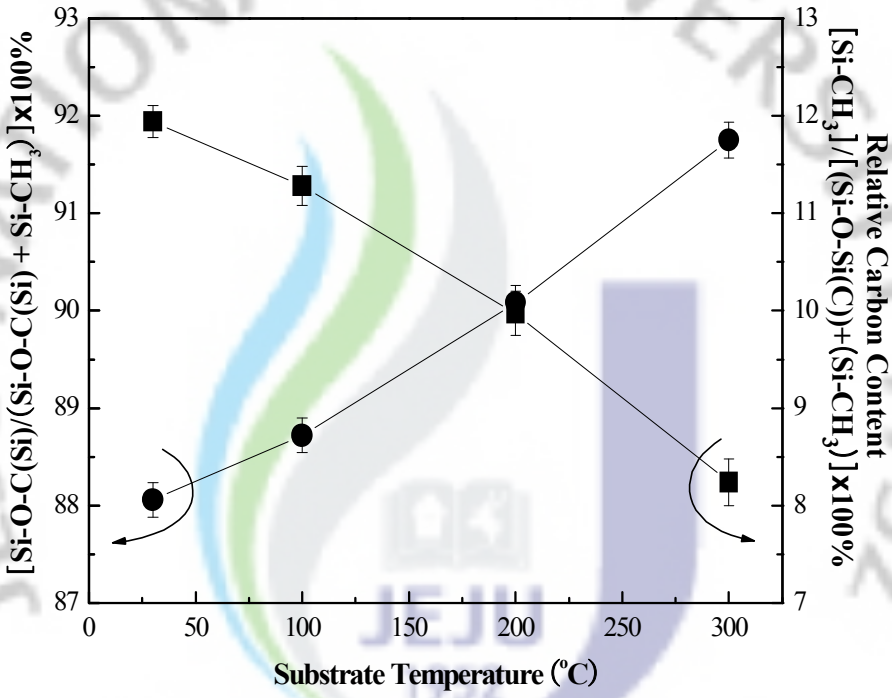

Fig. 38. Relative carbon and Si-O-C(Si) concentration (%) of the SiOC(-H) films deposited with different substrate temperatures.

scans of Si 2p, C 1s and O 1s electron orbital of the SiOC(-H) film prepared with different substrate temperature. The XPS narrow scane spectra were deconvoluted by fitting the data with a number of Gaussian peaks. The Si 2p electron orbital spectra consisted of five peaks as shown in Fig. 39(a) that were assigned to Si-C (98.7 eV), O-Si-$(CH_3)_3$ (100.5±0.1 eV), O_2-Si-$(CH_3)_2$ (101.6±0.1 eV), O_3-Si-CH_3 (102.6±0.1 eV) and Si-O_2 (103.6 eV) [59,60] for the SiOC(-H) deposited at room temperature. The binding energies that have been reported in previous studies are a little different from each other and the fitting procedure is somewhat arbitrary, but it is worth distinguishing the silicon in different states [72-74]. As the substrate temperature increased, the intensities of the peaks due to the O_2-Si-$(CH_3)_2$ and O_3-Si-CH_3 bonds were increased due to the bonding rearrangement at elevated temperatures. The SiOC(-H) films become oxygen rich as the substrate temperature increase, this is due to Si-C bonds being broken at elevated substrate temperatures leaving Si-O bonds dominant in the film. This is because the binding energy of the Si-C bond is lower than that of the Si-O bond [75]. The high relative percentage of the O-Si-C peak in the Si 2p spectra indicates that a randomly amorphous C-Si-O network was dominant in the SiOC(-H) film. This result means that more oxygen atoms are attached to the Si-O chain thus forming SiOC(-H) films at a higher substrate temperature. Figure 37(b) shows the C 1s electron orbital XPS narrow scan spectra of the SiOC(-H) films deposited at different substrate temperature which comprises of three bond components namely, Si-C (283.3±0.1 eV), C-C/C–H (284.6 eV), and C-O (286.2±0.1 eV) [64,65] for the films deposited at different substrate temperature. It is interestingly observed that slight chemical shift in the binding energies in the bonding structure as the substrate temperature increased which corresponds to the oxygen rich SiOC(–H) films. Figure 39(c) shows the O 1s electron orbital XPS narrow scan spectra of the SiOC(-H) films deposited at different substrate temperature which is decomposed into two components namely, O-C (530.1±0.1 eV) and O-Si (532.6 eV) [62], except for the film deposited at 200 and 300 °C. For the film deposited at 200 and 300 °C, the O 1s narrow scan spectrum is well fitted into one

peak at 532.6 eV (O-Si). This result means that more oxygen atoms are attached to the Si-O chain thus forming SiOC(-H) film at higher substrate temperature. The XPS narrow scans of Si 2p, C 1s and O1s spectra suggest that the major part of Si in the SiOC(-H) film is bonded with oxygen atoms to form an expected randomly Si-O-Si network. From these XPS results, we can infer that there are in good agreement with that of FTIR data showing the presence of the cage-linked and the ring-linked structure in the SiOC(-H) film. The various binding energies used for identification of the chemical groups are shown in Table 5.

Table 5. The Si 2p, C ls, and O 1s electron binding energies of the SiOC(-H) films.

Substrate Temperature	Si 2p (eV)					C 1s (eV)			O 1s (eV)	
	Si-C	O-SiO-$(CH_3)_3$	O_2-SiO-$(CH_3)_2$	O_3-SiO-$(CH_3)_1$	Si-O_2	Si-C	C-C/ C-H	C-O	O-C	O-Si
RT	-	100.4	101.4	102.5	103.6	283.2	284.6	286.2	530.1	532.6
100 °C	98.7	100.4	101.5	102.6	103.6	283.2	284.6	286.2	530	532.6
200 °C	-	100.4	101.7	102.7	103.6	283.1	284.6	286.1	-	532.6
300 °C	-	-	101.6	102.7	103.6	283.2	284.6	286.1	-	532.6

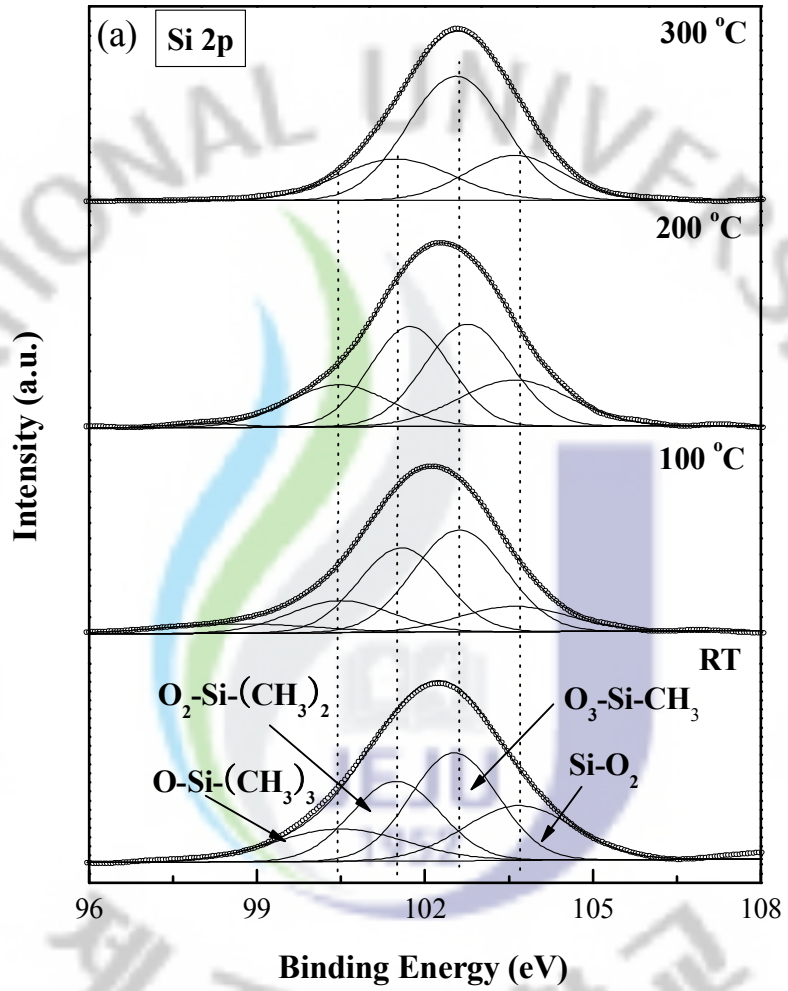

Fig. 39. XPS narrow scan spectra of the SiOC(-H) films deposited with different substrate temperature: (a) Si 2p electron orbital, (b) C 1s electron orbital and (c) O 1s electron orbital.

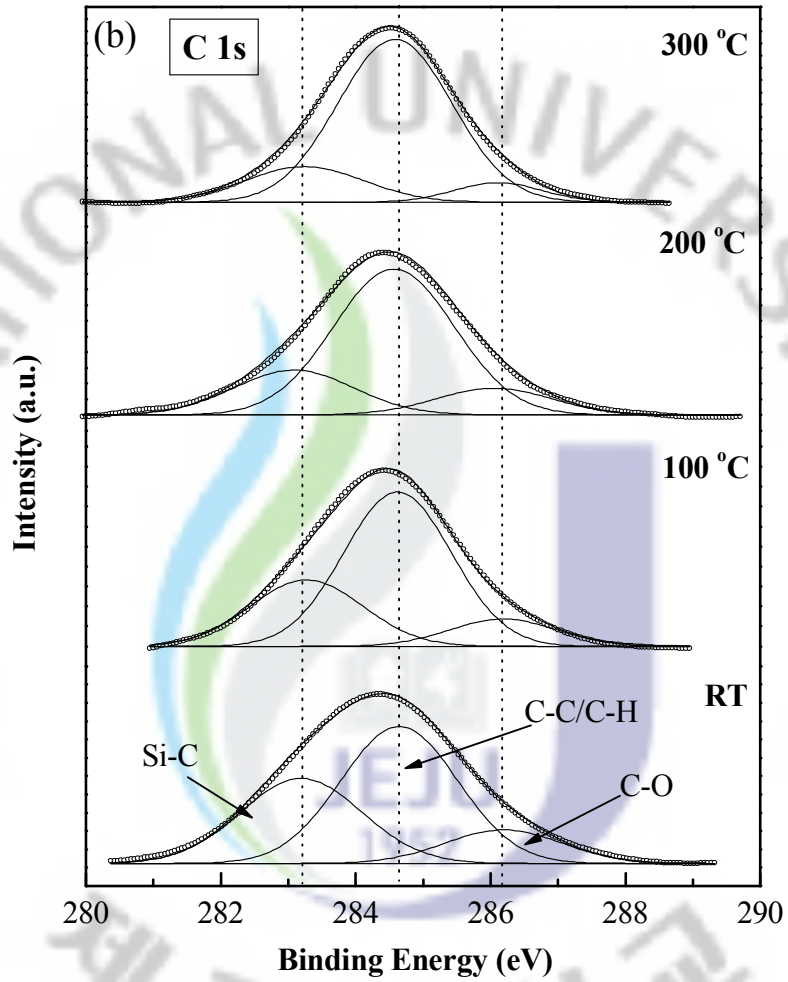

(continue)

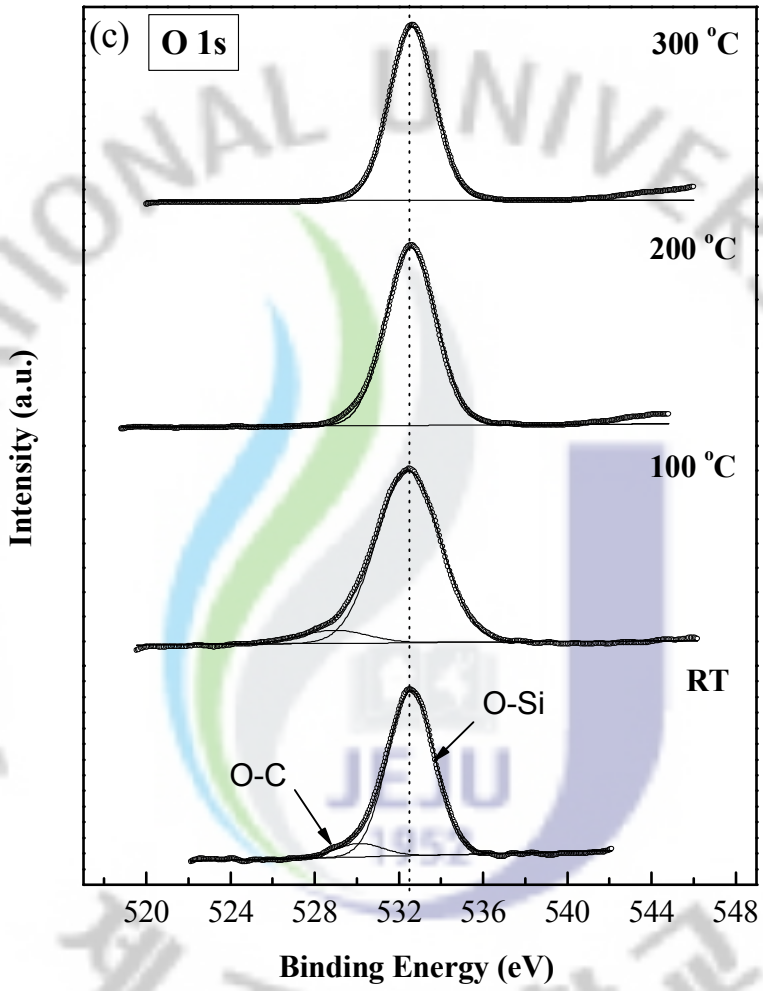

Figure 40 shows the dielectric constant and the refractive index of the SiOC(-H) films as a function of various substrate temperatures. It is found as a trend that both the dielectric constant and square of refractive index increase slightly with substrate temperature. The value of the dielectric constant and the refractive index of the SiOC(-H) films deposited at different substrate temperatures was found to increase from 2.22 to 2.49 and 1.36 to 1.45, respectively, as the substrate temperature increases from room temperature to 300 °C. And also, the dielectric constant is proportional to n^2, which the value of n^2 is about 2.11 at the substrate temperature of 300 °C. Comparing the structural behavior as observed from FTIR and XPS data, it is evident that the enhancement of oxygen rich atoms at higher substrate temperatures in the SiOC(-H) film result in a slight increase of dielectric constant, which can be attributed to the lower carbon concentration cause by the $Si\text{-}CH_3$ bonds broken at elevated substrate temperatures, as shown in Fig. 38. This can be explained by two factors: the decrease in the number of voids caused by the decreasing number of $Si\text{-}CH_3$ bonds [71,76]. Therefore, at higher substrate temperatures, the weaker $Si\text{-}CH_3$ and C-H bonds are broken, leaving the films with a lower concentration of these bonds, and making the SiOC(-H) films more oxygen rich.

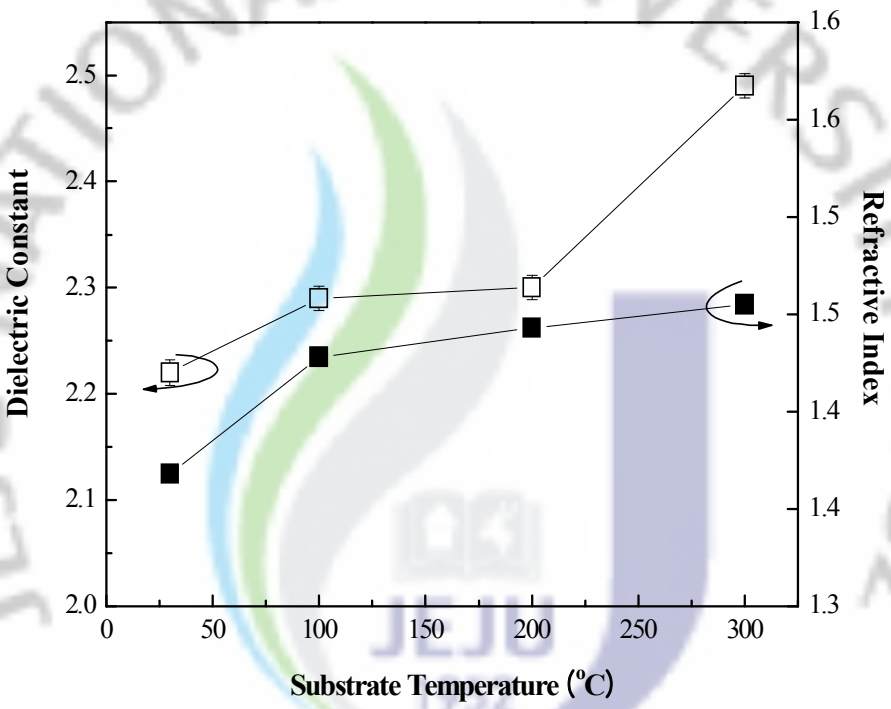

Fig. 40. Dielectric constant and refractive index of the SiOC(-H) films as a function of substrate temperature.

Chapter Ⅴ. Mechanical Properties of Low-*k* SiOC(-H) film

The mechanical properties of the low-*k* SiOC(-H) thin films were obtained by using the pyramidal Berkovich diamond indenter. The hardness and elastic modulus of the SiOC(-H) film were calculated from the load-displacement data followed the analytical method developed by Oliver and Pharr [77]. From the load-displacement data, the projected contact area, A, is deduced from an empirically determined shape function *A=F(d)* which describes the cross-sectional area of the indenter at a distanced, back from its tip; more specifically, the contact area is determined by evaluating the shape function at the contact depth, i.e., *A=F(hc)*. Once the contact area is known, the hardness follows from its normal definition

$$H = \frac{P_{\max}}{A}, \tag{59}$$

and the effective elastic modulus, E_{eff}, which accounts for elastic displacements in both the SiOC(-H) film and the indenter, is evaluated from

$$E_{eff} = \frac{1}{\beta}\sqrt{\pi}\frac{S}{2\sqrt{A}}, \tag{60}$$

Where β is a constant with a value of 1.034 for a Berkovich indenter [77] and S is contact stiffness. Finally, the elastic modulus of the SiOC(-H) film is extracted from the effective modulus by using

$$E_{eff} = [\frac{1-\gamma_s^2}{E_s}] + [\frac{1-\gamma_i^2}{E_i}]^{-1}. \tag{61}$$

Where E_i and γ_i are elastic modulus and Poisson's ratio for the indenter (diamond) and E_s and γ_s are those of the SiOC(-H) films. However, with the continuous stiffness measurement option, the stiffness of the contact area is measured directly at every point during the loading process. Hence, the hardness and elastic modulus can be measurement accurately and continuously as a function of the depth of the indentation.

Figure 41 show the typical load displacement (P-h) curves obtained during nanoindentation of the SiOC(-H) film, which the SiOC(-H) films were deposited at various substrate temperatures (RT, 100, 200 and 300 °C) with rf power of 700 W and precursor flow rate ratio of 80%, and the thickness of all samples is about 600 nm. The maximum indentation depth is 150 nm corresponding to an applied load of 1.4 mN. During the nanoindentation test, the force and displacement were recorded as the indenter tip was pressed into the surface of the SiOC(-H) film with a prescribed loading and unloading profile. With the known geometry of the diamond indenter tip, the depth of an indentation yields the area of contact between the indenter and the material being indented. Thus, the shape of the continuous P-h curve obtained on a film usually reflects the mechanical properties of that material.

Figures 42 and 43 show the elastic modulus (*E*) and hardness (*H*) as function of displacement of the SiOC(-H) films deposited with different substrate temperatures, respectively. In order to avoid the substrate effect on the SiOC(-H) film, we used films with a thickness greater than 600 nm for the nanoindentation measurements. From the mechanical properties data shown in Fig. 42 and 43, both the elastic modulus and hardness of the SiOC(-H) thin films deposited with different substrate temperatures are determined to be in the range from 19 to 30 GPa and from 2.2 to 3.5 GPa, respectively, at an indentation depth of 100 nm. It is observed that the value of *E* and *H* was found to be a minimum for the SiOC(-H) films deposited with lower and higher substrate temperatures. From these results, we can infer that the density of the SiOC(-H) film may be reduced when the films are prepared at

lower substrate temperatures. The higher concentration of the alkoxy groups (namely, C-O, C=O, C-C and C=C), which have a relatively poor mechanical property, lead to the lower hardness and elastic modulus. This is because more amount of carbon atoms are attached to the Si-O-Si chain network which resulted in the nano-porous structure in the SiOC(H) film. Because the amount of carbon concentration affects the values of the mechanical properties of the SiOC(-H) films. Therefore, the voids formed in the SiOC(-H) films are responsible for lower mechanical properties and the low dielectric constants. The values of the mechanical properties reported in our present investigation are higher than that of previous studies [78,79].

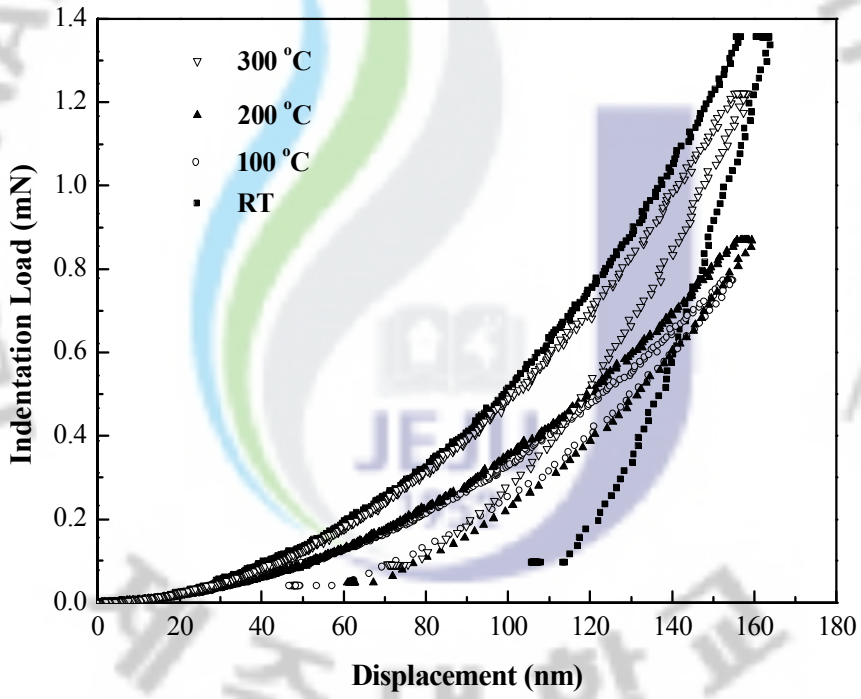

Fig. 41. Example of a typical load - displacement curve obtained during nanoindentation measurement of the SiOC(-H) films prepared at different substrate temperatures.

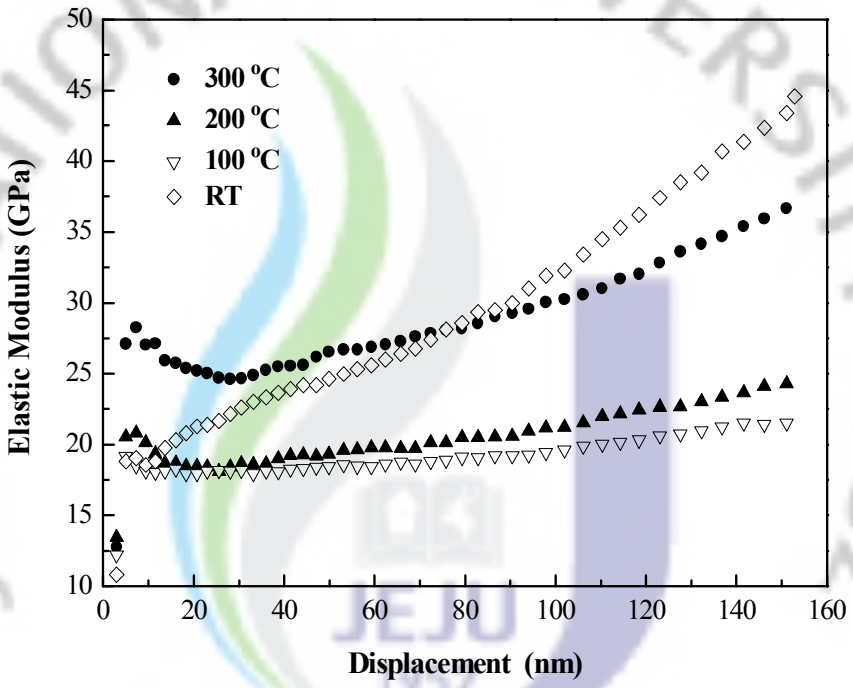

Fig. 42. Elastic modulus values of the SiOC(-H) films with different substrate temperatures.

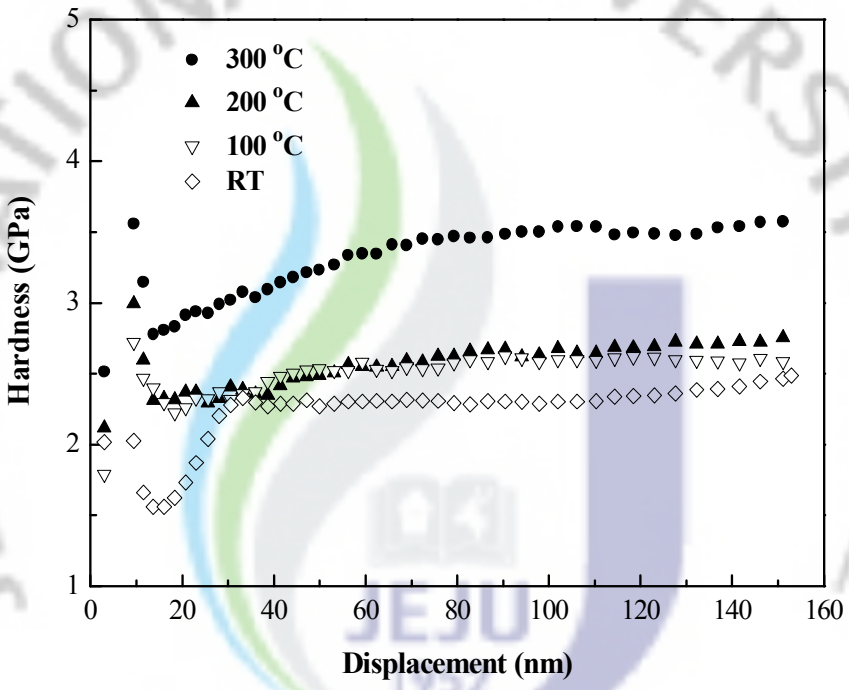

Fig. 43. Hardness values of the SiOC(-H) films with different substrate temperatures.

Chapter Ⅵ. Electrical Properties of the Cu(Al)/SiOC(-H)/*p*-Si(100) MIS Structures

1. Charge trapping properties of the Cu(Al)/SiOC(-H)/*p*-Si(100) MIS structures

The study of traps in the dielectric film is extremely important since the presence of oxide traps significantly affects device performance. Therefore, the origin of oxide traps should be clearly understood in order to control the traps. In this study, the charge trapping behavior of the Cu/SiOC(-H)/*p*-Si(100)/Al and Al/SiOC(-H)/*p*-Si(100)/Al samples was studied using an applied electric bias stress. Figures 44(a) and (b) shows the C-V curves before and immediately after the application of electric bias stress to the Cu/SiOC(-H)/*p*-Si(100)/Al and Al/SiOC(-H)/*p*-Si(100)/Al MIS structures, respectively. The bias stress was applied to the MIS structures for different durations, and the biasing voltage was maintained at +30 and -30 V. The C-V curve shifted towards a positive voltage over time. The positive shift of the flat-band voltage (V_{fb}) for both MIS structures shows that mainly electrons are trapped inside the SiOC(-H) dielectric film. However, the larger shift of V_{fb} indicates a higher amount of negative trap in the dielectric film. The V_{fb} shifts are positive for *p*-type substrates, indicating a trapped negative charge, in effect. The probability of hole injection is much smaller than electron injection for the SiOC(-H) dielectric film. For a low-voltage range, the possibility of generating defects due to a hydrogen related species is also very small [80-82]. For a *p*-type silicon substrate, the V_{fb} shift increased monotonically with injection fluences.

Figures 45(a) and (b) shows the C-V curves before and immediately after the electric bias stress (V_{st}=-30 V) for different durations for the as deposited and annealed Cu/SiOC(-H)/*p*-Si(100)/Al and Al/SiOC(-H)/*p*-Si (100)/Al MIS structures, respectively.

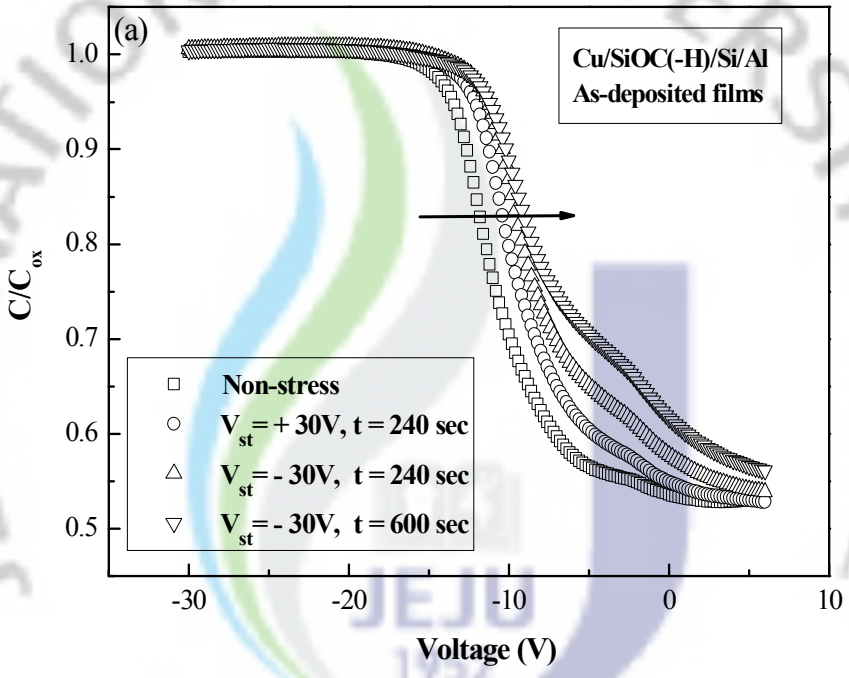

Fig. 44. C-V curves before and immediately after electric bias stress for (a) Cu/SiOC(-H)/*p*-Si (100)/Al and (b) Al/SiOC(-H)/*p*-Si (100)/Al structures.

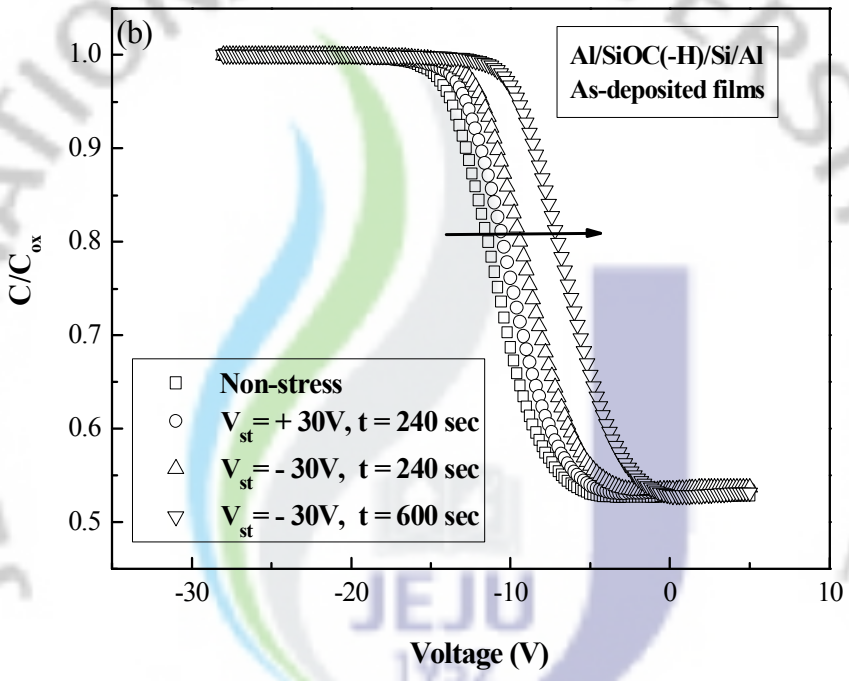

The positive V_{fb} shift after applied bias stress implies electron trapping for both Cu and Al metallization of the SiOC(-H) films. As the annealing temperature increased, both the capacitance value increased for the Cu and Al MIS structures. At the same time, the difference in flat band voltage ΔV_{fb} between non-stress and the stress fluences increased with increasing annealing temperature. This result means that the stress-induced charges increased with the injected fluence for both MIS structures and this increase, is attributed to the generation of localized defects and/or fixed charges at the interface region [83,84]. The value of V_{fb} was -18 V for as-deposited non-stress (do not stress) Cu/SiOC(-H)/*p*-Si(100)/Al structure, and -32 V for annealed structure at 450 °C. The values of V_{fb} was -11 V for as-deposited non-stress Al/SiOC(-H)/*p*-Si(100)/Al structure, and -26 V for the structure after annealing at 450 °C. This could be due to the work function difference between these two metals (the work function is 4.65 eV for Cu and 4.28 eV for Al). However, the value of ΔV_{fb} for as deposited non-stress Cu/SiOC(-H)/*p*-Si(100)/Al structure is 6 V and for the annealed structure at 450 °C, it is 15 V. In comparison the value of ΔV_{fb} for the as-deposited virgin Al/SiOC(-H)/*p*-Si(100)/Al structure is 5 V and for the structure annealed at 450 °C, it is 9 V.

The fixed charge densities, which were assumed to be located at the dielectric/semiconductor interface, were calculated for the MIS structures. V_{fb} is attributed to the trapping of charges by the gate dielectric film. Figure 46 shows the plot of the fixed charge density as a function of the annealing temperature of the Cu/SiOC(-H)/*p*-Si(100)/Al and Al/SiOC(-H)/*p*-Si (100)/Al MIS structures. The fixed charge density was predicted by calculation to increase with increasing annealing temperature for the virgin MIS structure. For the Cu/SiOC(-H)/*p*-Si(100)/Al structures, the fixed charge increased from 1.6×10^{12} cm^{-2} to 2.5×10^{12} cm^{-2} whereas this charge increased from 0.6×10^{12} cm^{-2} to 2.7×10^{12} cm^{-2} for Al/SiOC(-H)/*p*-Si(100)/Al structures, with increasing annealing temperature. This behavior may be due to thermally-induced localized charges generated at the interface of the MIS structures.

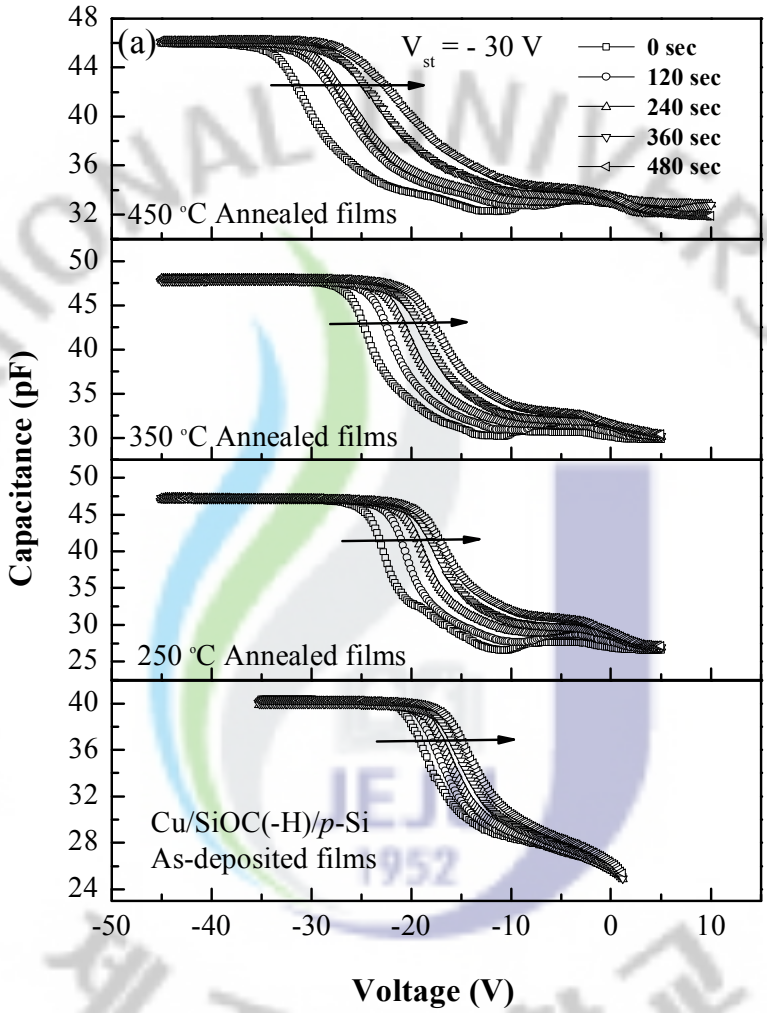

Fig. 45. C-V curves before and immediately after electric bias stress of different durations for the as-deposited and the annealed MIS structures: (a) Cu/SiOC(-H)/*p*-Si(100)/Al and (b) Al/SiOC(-H)/*p*-Si(100)/Al structures.

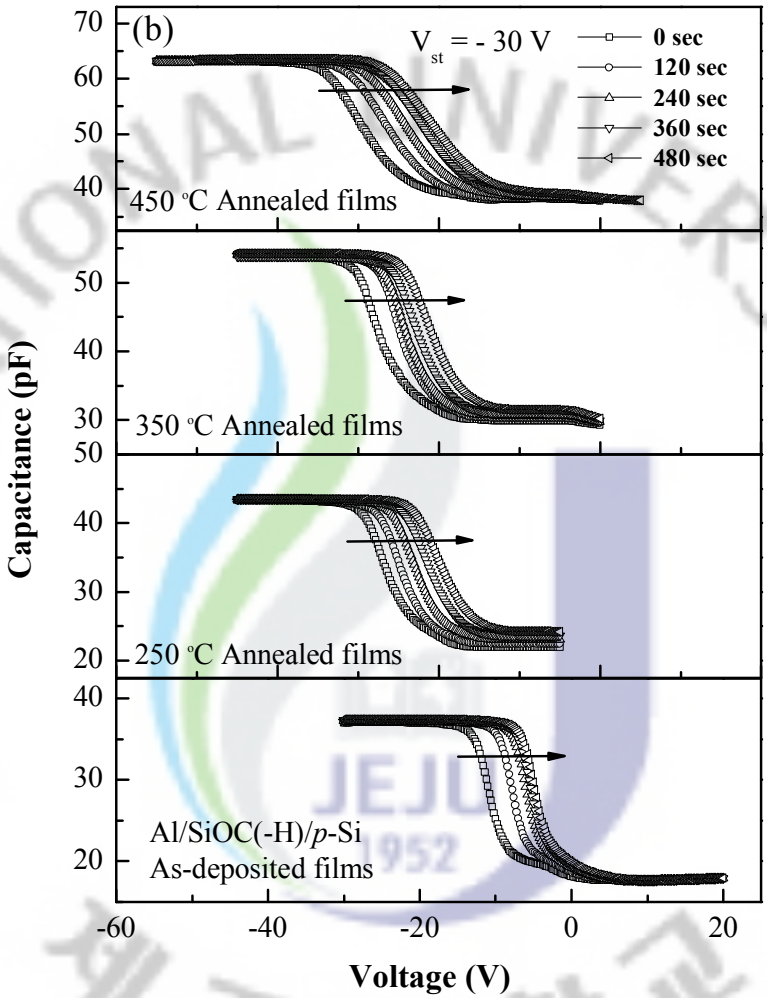

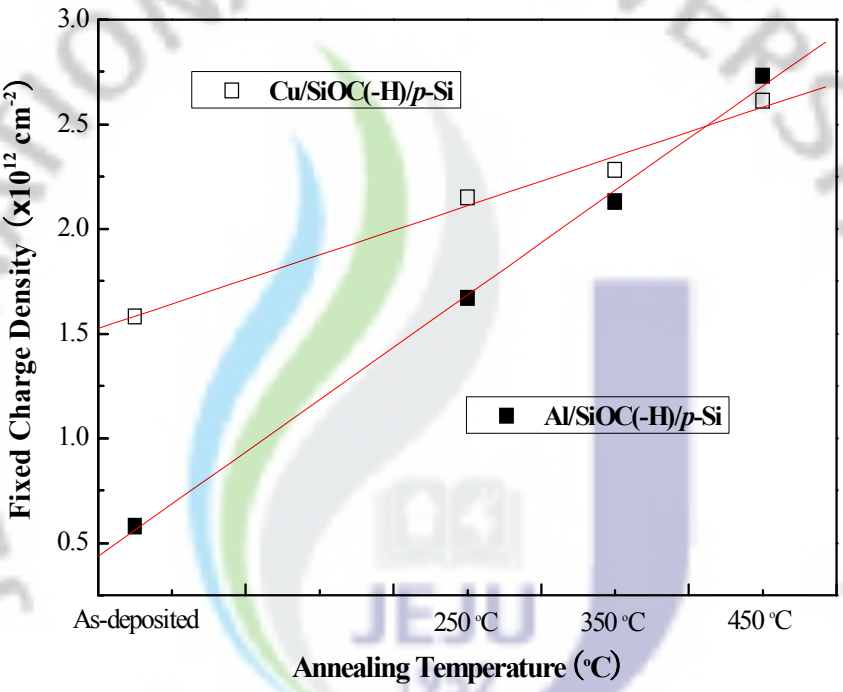

Fig. 46. Plot of fixed charge density as a function annealing temperature of Cu/SiOC(-H)/*p*-Si(100)/Al and Al/SiOC(-H)/*p*-Si(100)/Al MIS structures.

Figure 47 shows the relation between the trapped charge density and the injected electron fluence of the as-deposited and the annealed Cu/SiOC(-H)/*p*-Si(100)/Al and Al/SiOC(-H)/*p*-Si(100)/Al MIS structures at a constant electric bias stress of V_{st}=-30 V. The equation $\Delta Q_{ox}=C_x\Delta V_{fb}$ was used to calculate the change of oxide trapped charges between the first and the second C-V measurements [85] where ΔQ_{ox} is the change in the fixed oxide charge, C_x is the capacitance of the SiOC(-H) dielectric film, and ΔV_{fb} is the change in the flat-band voltage. The post metallization annealing condition could also affect the trap density. It was observed that the trapped charge density increased with increasing annealing temperature. For lower annealing temperature ($T\leq$250 °C), the trap charge density showed saturation after a linear increment with the injected fluence. However, at higher annealing temperatures ($T\geq$350 °C), the trap charge density increased exponentially with the injected fluences as shown in Fig. 47. As the injection fluence continued to increase for a given bias stress voltage (V_{st}=-30 V), the mid-gap of the trapped charge will gradually shift toward the Si substrate, which contributes to the increase in the V_{fb} shift with the increase of non-stress V_{fb}. In other words, the value of ΔV_{fb} tended to increase. This result is in good agreement with the data shown in Figs. 44 and 45. The values of various interface charges for SiOC(-H)/*p*-Si(100) structure determined from C-V curves are shown in Table 6.

Figures 48(a) and (b) shows the energy distribution of the interface state density before and after bias stressing (V_{st}=-30 V) with different durations of as-deposited and annealed Cu/SiOC(-H)/*p*-Si(100)/Al and Al/SiOC(-H)/*p*-Si(100)/Al MIS structures, respectively. Both MIS structures revealed the most of similar energy density distribution of the interface states before and after electrical bias stress for different durations. Although the charge in the interface traps at the flat-band point is not known with certainty, we suspect that interface traps in the upper half of the silicon band-gap are donor-like, and that their charge state is negative when filled with an electron. Under this assumption, the effect of interface traps on the measurement of oxide charge was explored [82]. However, it was found that the interface state

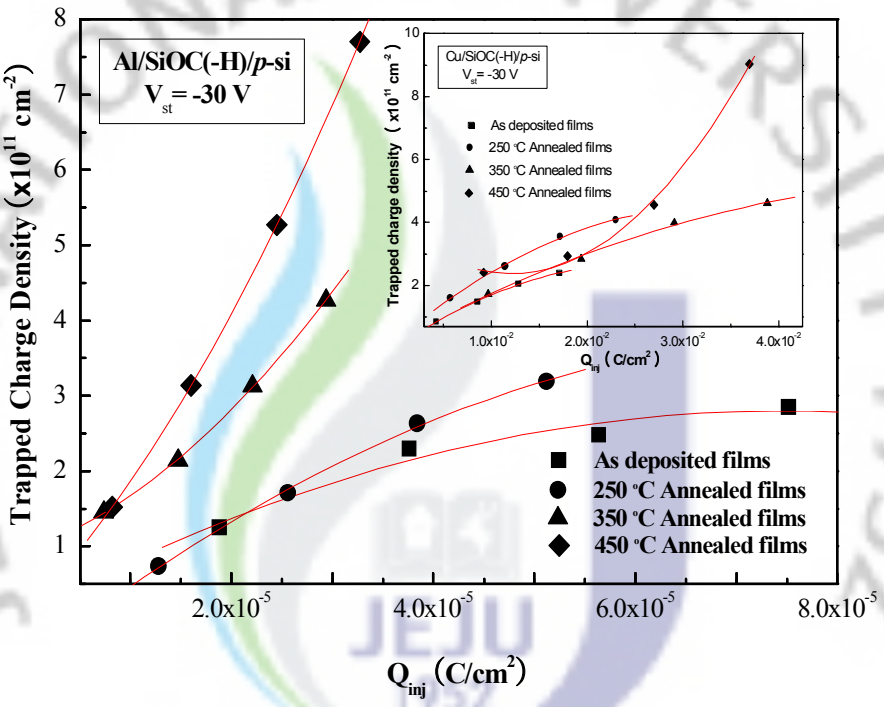

Fig. 47. Relation between trapped charge density and the injected electron fluencies of as-deposited and annealed Al/SiOC(-H)/*p*-Si(100)/Al structures. Inset is for the Cu/SiOC(-H)/*p*-Si(100)/Al structures.

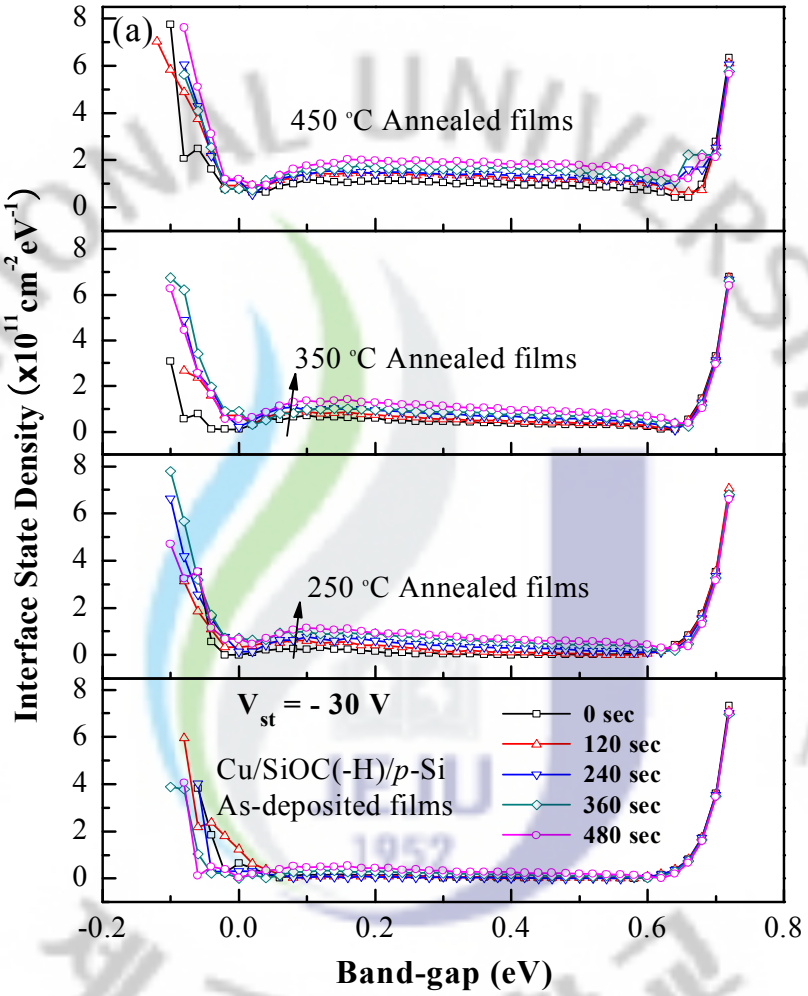

Fig. 48. Energy distribution of interface state density for before and after stressing of as-deposited and annealed MIS structures: (a) Cu/SiOC(-H)/*p*-Si(100)/Al and (b) Al/SiOC(-H)/*p*-Si(100)/Al structures.

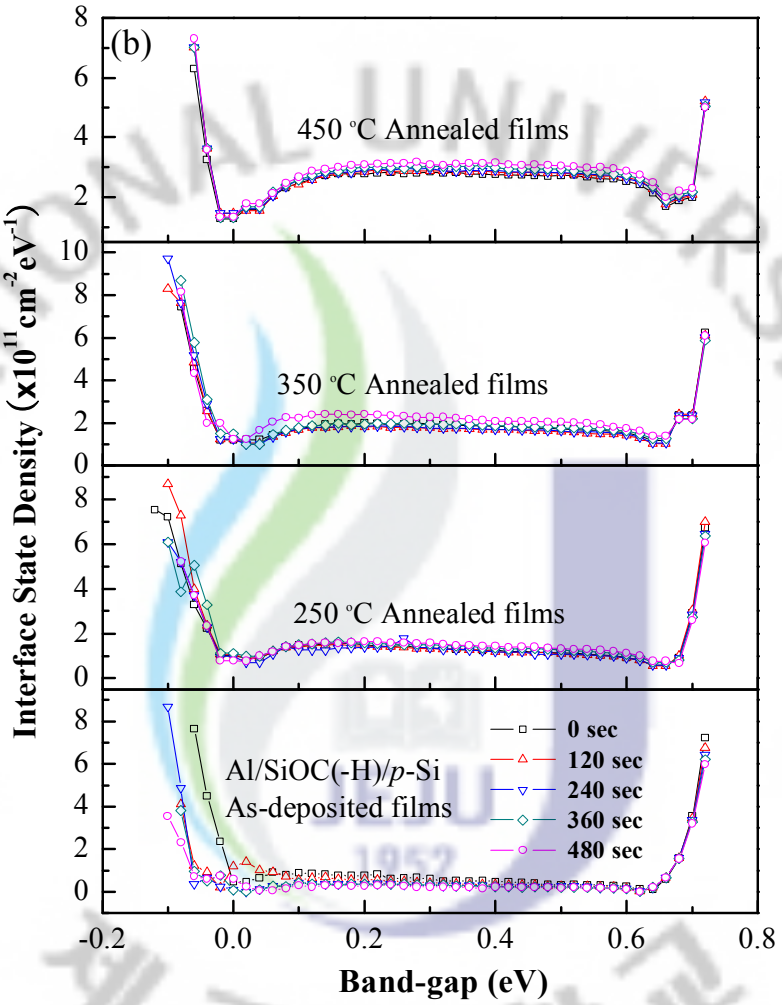

Table 6. The values of various interface charges for SiOC(-H)/*p*-Si(100) structure determined from C-V curves

Annealing Temperature	Fixed charge density		Trapped charge density		Interface state density	
	Cu ($\times10^{12}$cm^{-2})	Al ($\times10^{12}$cm^{-2})	Cu ($\times10^{11}$cm^{-2})	Al ($\times10^{11}$cm^{-2})	Cu ($\times10^{11}$cm^{-2} eV^{-1})	Al ($\times10^{11}$cm^{-2} eV^{-1})
RT	1.58	0.58	0.85	1.25	0.02	0.53
250 °C	2.15	1.67	1.61	1.71	0.01	1.24
350 °C	2.28	2.13	1.73	1.45	0.38	1.87
450 °C	2.61	2.73	2.41	1.52	0.99	2.76

density at the Si mid-gap was lower for the non-stress MIS structures than for the stressed structures. Noticeable changes in the interface state density distribution were observed in the as-deposited and annealed structures of the virgin and electrically stressed Cu/SiOC(-H)/*p*-Si(100)/Al MIS structures, as shown in Fig. 48(a). After electrical stress, the interface state increment indicated that the hydrogen-related incorporation of the trivalent silicon dangling bond at the interface with H and/or OH had formed. This can be explained by the breaking of the hydrogen-related bond in the -Si-H and -Si-OH species at the interface during electrical stressing [86]. Therefore, interface generation is closely related to hydrogen termination and hydrogen releasing (bond breaking) at the SiOC(-H)/*p*-Si(100) interface. On the other hand, only a slight difference was observed for the case of the Al/SiOC(-H)/*p*-Si(100)/Al MIS structures, as shown Fig. 48(b).

In order to obtain a better understanding of the electrical bias stressing effects of the Cu/SiOC(-H)/*p*-Si(100)/Al and Al/SiOC(-H)/*p*-Si(100)/Al MIS structures, we

deduced the relation between the interface state density and the electron injection time. Figures 49(a) and (b) shows a plot of the interface state density as a function of the electron injection time for the as-deposited and the annealed Cu/SiOC(-H)/*p*-Si(100)/Al and Al/SiOC(-H)/*p*-Si(100)/Al MIS structures at an electric bias stress of V_{st}=-30 V, respectively. The interface state density of the Cu/SiOC(-H)/*p*-Si(100)/Al MIS structure increased gradually with increasing annealing temperature and with stressing duration, as shown in Fig. 49(a). However, the interface state density of the Al/SiOC(-H)/*p*-Si(100)/Al MIS structure did not significantly affect either the annealing temperature or stressing duration, as shown in Fig. 49(a). This result is in good agreement with the data shown in Figs. 44 and 45.

Figures 50(a) and (b) shows an HR-TEM image of the as-deposited and annealed (450 °C) SiOC(-H)/*p*-Si(100) interface structures, respectively. A smooth SiOC(-H)/*p*-Si(100) interface with a flatness comparable on an atomic scale was observed for the as-deposited structure as shown in Fig. 50(a). However, a dense layer appeared at the SiOC(-H)/*p*-Si(100) interface annealed at 450 °C, which is attributed to the diffused state at the interface. This HR-TEM data is also in agreement with the C-V characteristics of the bias-stressed as-deposited and annealed MIS structures.

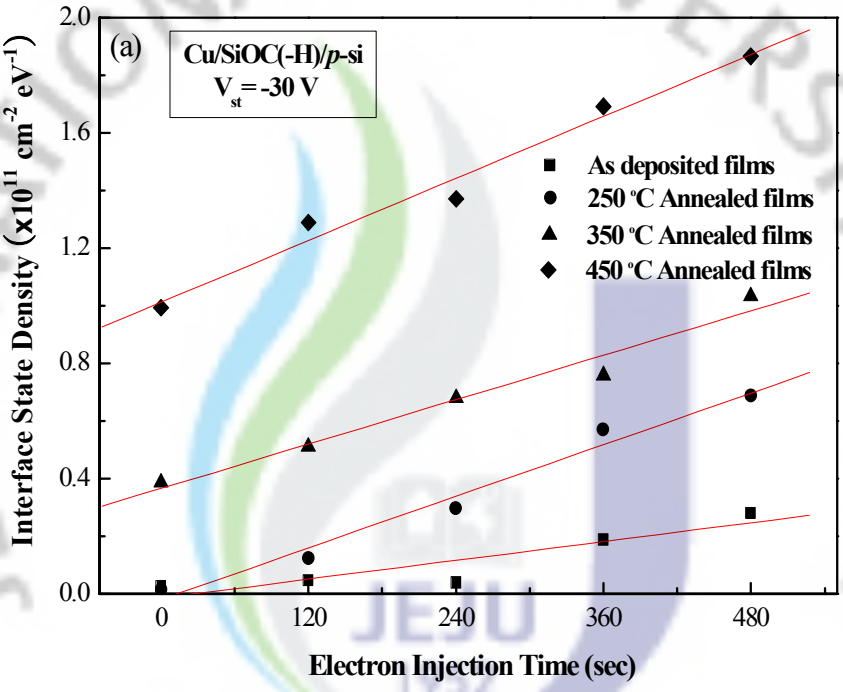

Fig. 49. Plot of interface state density as a function of electron injection time for the as-deposited and the annealed MIS structures: (a) Cu/SiOC(-H)/*p*-Si(100)/Al and (b) Al/SiOC(-H)/*p*-Si(100)/Al structures.

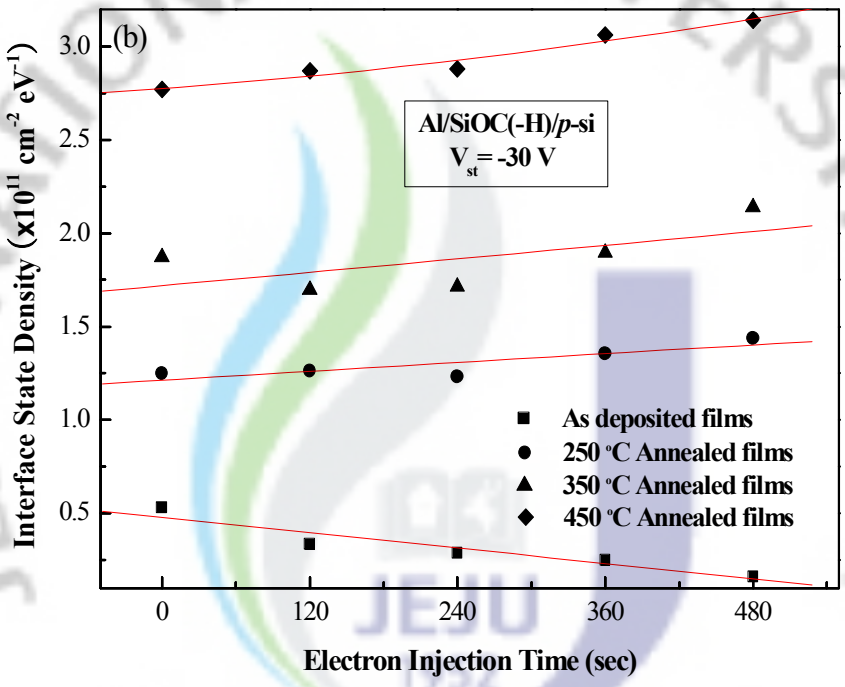

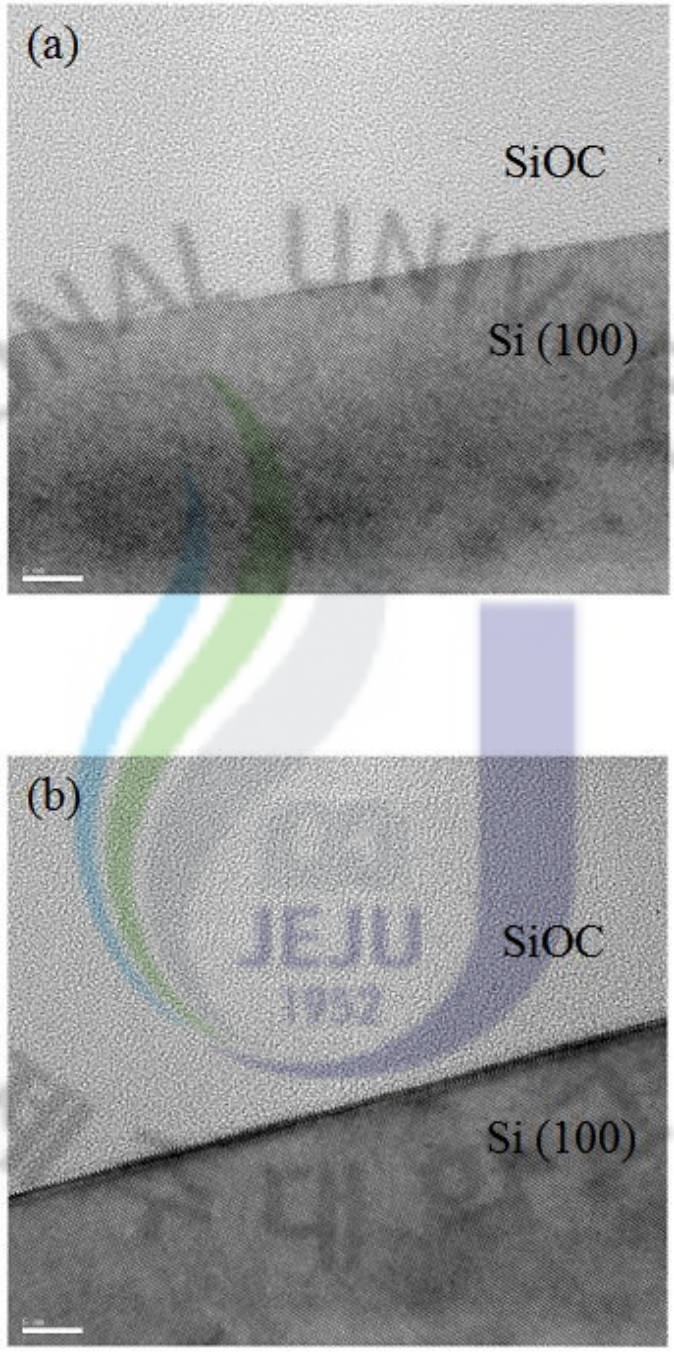

Fig. 50. HR-TEM image of the SiOC(-H)/*p*-Si(100) interface structure for (a) as deposited, and (b) annealed 450 °C structures.

2. Cu diffusion behavior in Cu/SiOC(-H)/*p*-Si(100) MIS structures

The low resistivity of Cu films compared to Al films helps reduce the resistance and capacitance of an RC delay. The major problem with Cu metallization is its high diffusivity in silicon, silicon dioxides and other dielectrics used in integrated circuits. Therefore, it is important to develop an effective diffusion barrier between the SiOC(-H) film and Cu to prevent Cu diffusion. This session investigated the Cu diffusion behavior in low dielectric SiOC(-H) films. Cu/SiOC(-H)/*p*-Si(100)/Al, a MIS structure, was subjected to BTS at various temperatures with a dc bias of 30 V. The role of Cu^+ ions on the properties of the resulting SiOC(-H) films is discussed based on the results of AES and HR-TEM.

Figure 51 shows the C-V characteristics of the Cu/SiOC(-H)/*p*-Si(100)/Al, MIS structure annealed at various temperatures with a BTS of V_{st}=30 V at 225 °C. As the BTS time increased, the V_{fb} shifted more towards the negative region of the C-V curve. For example, with a BTS time of 40 min, the V_{fb} was -15, -18 and -34 V corresponding to the MIS structures annealed at 250, 350 and 450 °C, respectively. A decrease in inversion capacitance with different BTS conditions was observed using *p*-type Si(100) substrates. All the annealed MIS structures showed clear accumulation, depletion and inversion regions except for the sample annealed at 250 °C with a BTS time of 0 and 10 min. The difference in C-V characteristics might be caused by the positive charge carrier due to chemical bonds, such as $-CH_3$ or $Si-CH_3$ and Si-H, incorporated into the SiOC(-H) film with an annealing process. On the other hand, the decrease in inversion capacitance might be caused by the diffusion of Cu atoms, which can produce a deep donor level of 0.49 eV above the valence bond. As a result, generation-recombination centers near the intrinsic levels can reduce the carrier life in such a way that inversion capacitance increases the oxide capacitance [87,88]. Prolonged BTS resulted in a significant V_{fb} shift, a decrease in inversion capacitance and a distortion of the C-V characteristics, as

shown in Fig. 51. A positive flat-band voltage shift revealed an increase in the positive charge (Cu^+) in the SiOC(H) film. Therefore, the drift diffusion of Cu^+ ions was studied carefully by determination of the shift in V_{fb} in the C-V curve of the MIS structures before and after BTS. The values of the flat-band voltage shift are shown in Table 7.

Table 7. The values of the flat-band voltage shift of Cu^+ ion in the SiOC(H) film.

Annealing Temperature	Measurement temperature								
	175 °C			200 °C			225 °C		
	Stress time (min)								
	10	20	40	10	20	40	10	20	40
	Flat-band voltage shift (V)								
250 °C	5.8	8.1	10	6.2	9.6	13.2	9.3	12.0	14.1
350 °C	5.3	6.9	11.9	5.5	11.2	17.1	9.3	14.5	17.5
450 °C	5.7	7.8	13.2	7.7	14	16.7	12.4	18.2	20.8

Annealing Temperature	Measurement temperature					
	250 °C			276 °C		
	Stress time (min)					
	10	20	40	10	20	40
	Flat-band voltage shift (V)					
250 °C	10.2	13.7	17.7	13.6	22.6	-
350 °C	10.8	13.4	17.7	13.9	25.7	-
450 °C	-	-	-	-	-	-

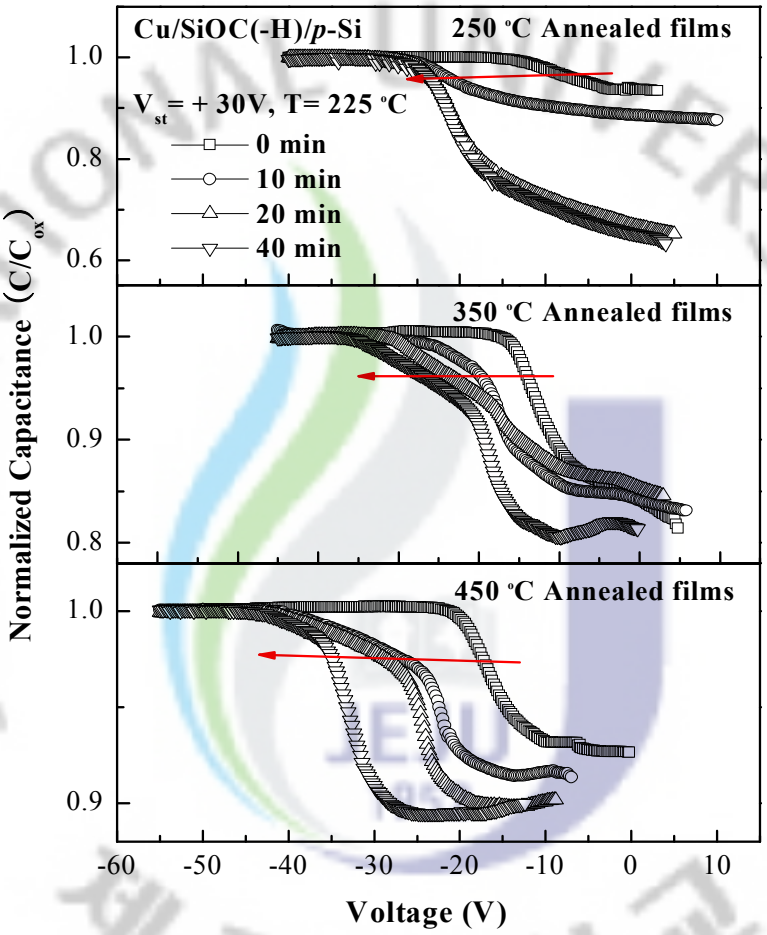

Fig. 51. C-V curves before and immediately after bias temperature stress (V_{st}=30 V, T=225 °C) for the annealed Cu/SiOC(-H)/p-Si(100)/Al MIS structures.

Figure 52 shows the flat-band voltage shift of the Cu^+ ions ($\triangle V_{fb[Cu^+]}$) as a function of the BTS time with various temperatures at an applied electric field of 2 MV/cm for the Cu/SiOC(-H)/*p*-Si(100)/Al MIS structure. The SiOC(-H) films deposited at RT were annealed at temperatures ranging from 250 to 450 °C. Every data point represents the mean of 10 tested MIS structures. The MIS structures stressed between 175 and 225 °C showed minor changes in the flat-band voltage of the Cu^+ ions ($V_{fb[Cu^+]}$) with changes in the stressing time, while the structures stressed between 225 and 275 °C had a higher $\triangle V_{fg[Cu^+]}$ of Cu atoms, as shown in Figs. 52 (a), (b) and (c). For the sample with the BTS of V_{st}=30 V at 225 °C, the $\triangle V_{fg[Cu^+]}$ values of the samples with the stress time of 20 min obtained about 12, 14.5 and 18.2 V at annealed temperature of 250, 350 and 450 °C. A significant V_{fb} shift was observed with increasing post-annealing of the MIS structures and BTS time. This may be due to the higher level of Cu^+ ions entering into the SiOC(-H) dielectric film during the extended BTS treatment. However, for the MIS structure annealed at 450 °C, the C-V characteristics failed under the BTS conditions of 250 and 275 °C, as shown in Fig. 48(C). The general trend clearly suggests the continuous injection of Cu^+ ions and the rapid injection of Cu^+ ions at high temperatures [89].

The drift rate of Cu^+ ions can be determined from the gradients of the lines fitted using the following expression to quantify the diffusion [90].

$$\frac{d[Cu^+]}{dt} = -\frac{C_{OX}}{q}\frac{d(\Delta V_{fb[Cu^+]})}{dt} \tag{62}$$

where $[Cu^+]$ is the Cu atom concentration per unit area, C_{OX} is the dielectric stack capacitor per unit area, and q is the magnitude of the charge on an electron (1.63×10^{-19} C). This equation assumes that the Cu^+ ions drift to the SiO_2/Si interface. The initial drift rate is determined by the change in the electric field in the dielectric with time due to the accumulation of Cu^+ ions.

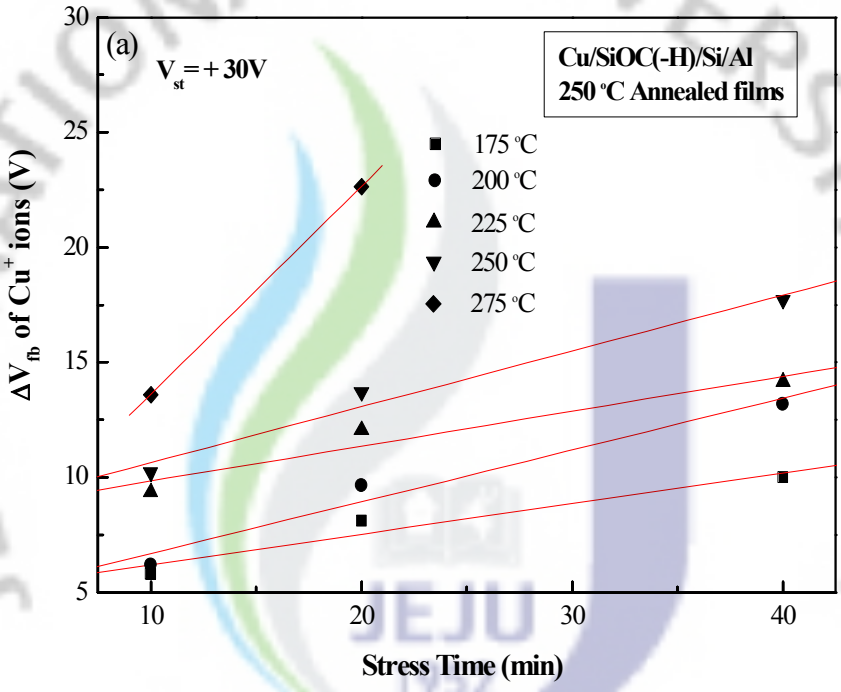

Fig. 52. Difference in the flat-band voltage (ΔV_{fb}) due to the diffusion of Cu^+ ions as a function of the stress duration of the annealed Cu/SiOC(-H)/*p*-Si(100)/Al MIS structure for (a) 250 °C, (b) 350 °C and (c) 450 °C.

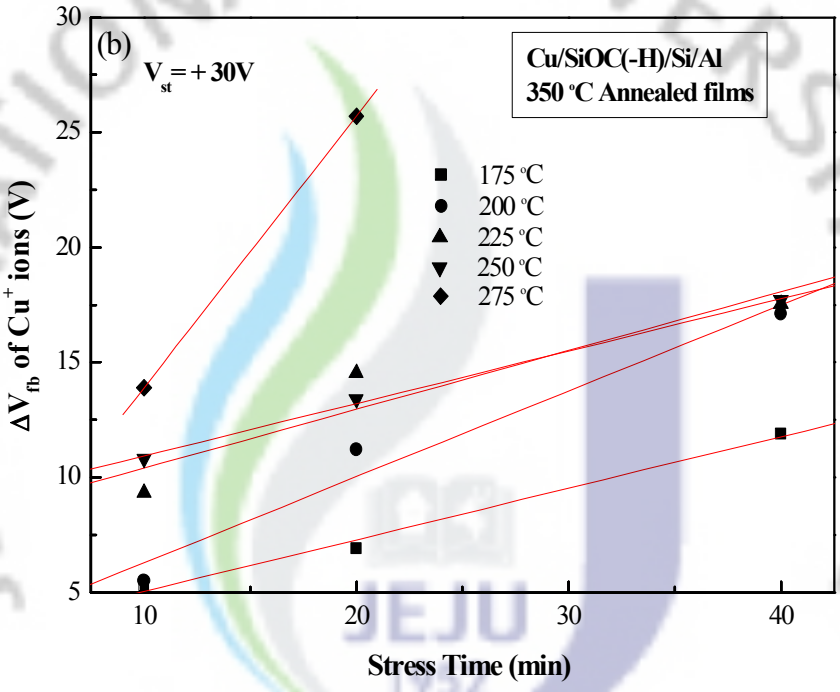

(continue)

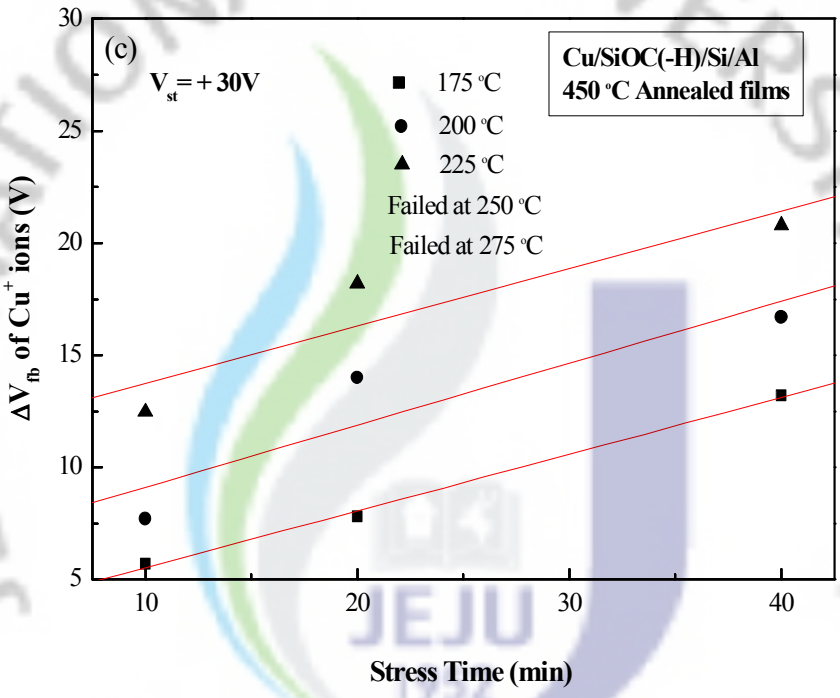

Figure 53 shows Arrhenius plots of the Cu^+ ions drift rate in the Cu/SiOC(-H)/*p*-Si(100)/Al, MIS structure at different annealed temperatures. The Cu^+ ions drift rate of the samples with annealed temperature of 250, 350 and 450 °C increased from 4.07×10^9 to 1.41×10^{11} ions/cm^{2}sec, from 9.12×10^9 to 5.25×10^{10} ions/cm^{2}sec and from 3.73×10^{10} to 5.75×10^{10} ions/cm^{2}sec as a function of the stress temperature. The drift rate of the Cu^+ ions in the material increased with increasing annealing temperature. The estimated activation energy (E_a) of the Cu/SiOC(-H)/*p*-Si(100)/Al MIS structures under BTS was 0.58, 0.26 and 0.22 eV at annealing temperatures of 250, 350 and 450 °C, respectively, indicating a decrease with increasing annealing temperature. The E_a values derived from the BTS treatments for the Cu/SiOC(-H)/*p*-Si(100)/Al MIS structures were compared with those reported previously [91]. The E_a for the Cu^+ ion in porous spin-on deposition (SOD) dielectric (0.71±0.04 eV) was higher than that reported for the diffusion of the Cu^+ ion in silica xerogels (0.42-0.55 eV) [92]. In addition, the E_a of the Cu^+ ion derived for the low-density PECVD dielectric (0.84±0.05 eV) is comparable to that reported for a similar dielectric type, such as MSQ (0.81 eV)[92] and methyl-doped SiO_2 (0.76 eV). For thermal SiO_2, the E_a of the Cu^+ ion was 1.02±0.12 eV, which is similar to that reported by Shacham-Diamand et al. [87] (0.93±0.2 eV) and slightly lower than that reported by McBrayer et al. [93] (1.82 eV). In general, for field assisted diffusion, the diffusion of the Cu^+ ions will be greater than that induced by thermal stress alone. Hence, the activation energy derived from the BTS experiments is expected to be lower [94]. However, other parameters, such as the analysis procedure used to derive the E_a, temperature range, bias employed, and environment, may produce different values.

The distribution of the atomic concentration was determined by AES analysis of the as-deposited and annealed Cu/SiOC(-H)/*p*-Si(100)/Al MIS structures before and after the BTS treatment, as shown in Fig. 54. In this figure, the symbols of an open uptriangle, open circle and open diamond stand for the spectra of the Si, C and O atoms for the deposited SiOC(-H) layer, while the symbol of the downtriangle stands

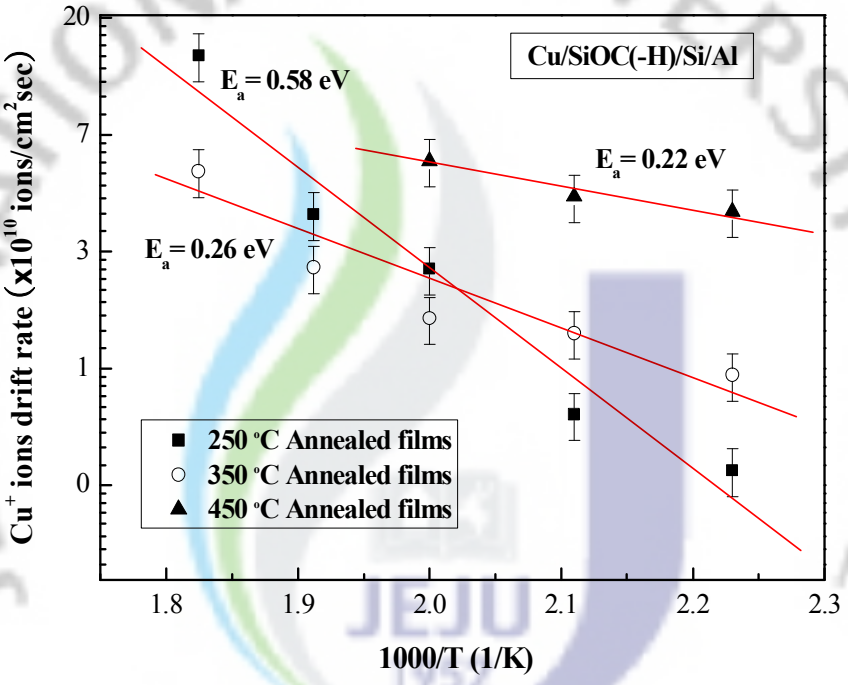

Fig. 53. Arrhenius plot of the Cu^{+} ions drift rate of Cu/SiOC(-H)/*p*-Si(100)/Al MIS structure annealed at different temperatures.

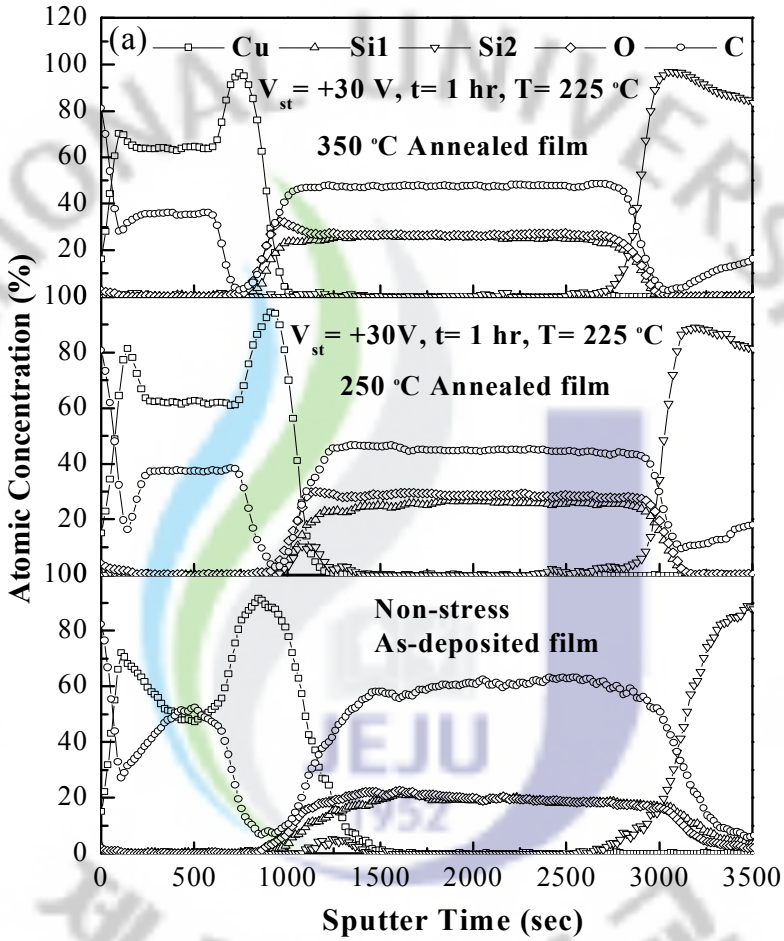

Fig. 54. AES depth profiles of Cu/SiOC(-H)/*p*-Si(100)/Al MIS structure with (a) as deposited, annealed at 250 °C and 350 °C, and (b) annealed at 450 °C, inset shoeing the chemical state of O 1s-O (KLL) plot for silicon-oxygen compounds.

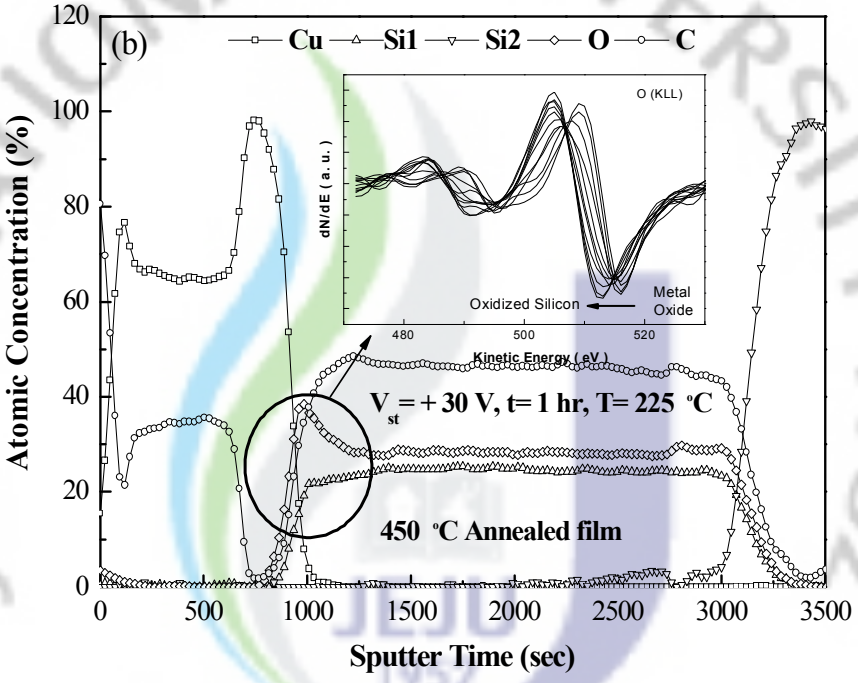

for the spectrum of the Si atom for the substrate silicon. The SiOC(-H) films are uniform in composition and have a smooth interface. The stoichiometric compositions of the samples obtained were found to be $SiO_{1.1}C_{1.7}$ when annealed at 250 °C and 350 °C while the composition $SiO_{1.2}C_{1.8}$ was obtained at annealing temperature of 450 °C. However, the as-deposited sample showed a non-uniform structure with a stoichiometric composition of $SiO_{1.0}C_{3.5}$. We can see that the impurity carbon atom on the Cu/SiOC(-H) surface were removed with sputtering in about 100 sec, which is equivalent to the removal of a sample thickness of about 6 nm. The impurity carbon atom was adsorbed into the Cu/SiOC(-H) surface, when the sample was exposed to air. When the carbon atoms are sputtered around 100 to 850 sec, they were contaminated partially during the deposition of Cu metal. The Cu/SiOC(-H) interface of all the samples were seen to contain a mixture of Cu, O, C and Si atoms, and the thickness was about 10 nm. The depth of the Cu diffusion layer was about 8 nm for samples annealed at 250 °C and 350 °C while the BTS, with depth of about 4 nm, was deeper than the BTS obtaining in the as-deposited sample, in the absence of applied stress. Howerver, the depth of the Cu diffusion layer of the sample annealed at 450 °C with BTS treatment is deeper, as shown in Fig. 54(b). The AES data clearly shows that the diffusion rate of the atomic species involved increased with increasing annealing temperature and BTS treatment [as shown in Fig. 54(a)]. A Cu atoms diffusing through the bulk may remain associated with SiO^- or continue diffusing, so it can either react to form a Cu silicide or a Cu oxide [95]. For example, as shown in the inset of Fig. 54(b), the chemical state of the O 1s-O (KLL) plot of the Auger parameter band for silicon-oxygen compounds shows two distinguishable energy states [as shown in the circular region in Fig. 54 (b)]. The Cu_2O/CuO metal oxide becomes the source for Cu^+/Cu^{++} available for diffusion in annealed samples with the BTS. In addition, the oxidation of Cu_2O to CuO is slower than the oxidation of Cu to Cu_2O, as reported by Rodriguez et al. [96]. Therefore, in such cases, the product of diffusivity and solid solubility of Cu^{++} in the oxide is insignificant compared to that of Cu^+ in the dielectric film [97]. Moreover, it can be

assumed that primarily singly ionized Cu atoms are injected into the dielectric layer. In other words, a notable red-shift in the kinetic energy was observed, which was attributed to the larger amount of Cu atoms into the SiOC(-H) dielectric film. The injection of Cu atoms leads to charge build up in the SiOC(-H) dielectric film and a larger increase in the V_{fb} in the C-V characteristics. When the concentration of Cu atoms in the SiOC(-H) dielectric film reaches a critical value, a conduction path that links the cathode and anode may form, triggering dielectric breakdown [96], as observed in the case of the Cu/SiOC(-H)/*p*-Si(100)/Al MIS structure annealed at 450 °C. In addition, the C-V characteristics failed under the BTS of 250 and 275 °C, as shown in Fig. 52(C).

The diffusion behavior of Cu atoms was further confirmed by HR-TEM. Figures 55(a) and (b) show an HR-TEM image of the as-deposited and annealed at 450 °C Cu/SiOC(-H)/*p*-Si(100) interface structures, respectively. The Cu metal thickness of Fig. 55(a) and 55(b) is about 35 nm. Smooth Cu/SiOC(-H) interface was observed in the as-deposited structure, as shown in Fig. 55(a). However, a diffused interfacial layer (about 10 nm) was observed in the Cu/SiOC(-H) interface annealed at 450 °C after BTS treatment, as marked by the white arrow. Thickness of diffused interfacial layer corresponds to thickness of Cu/SiOC interface determined by HR-TEM analysis. The presence of Cu at the interface was confirmed. The diffused interface layer increased with increasing annealing temperature and BTS treatment. This result agrees to the C-V and AES data.

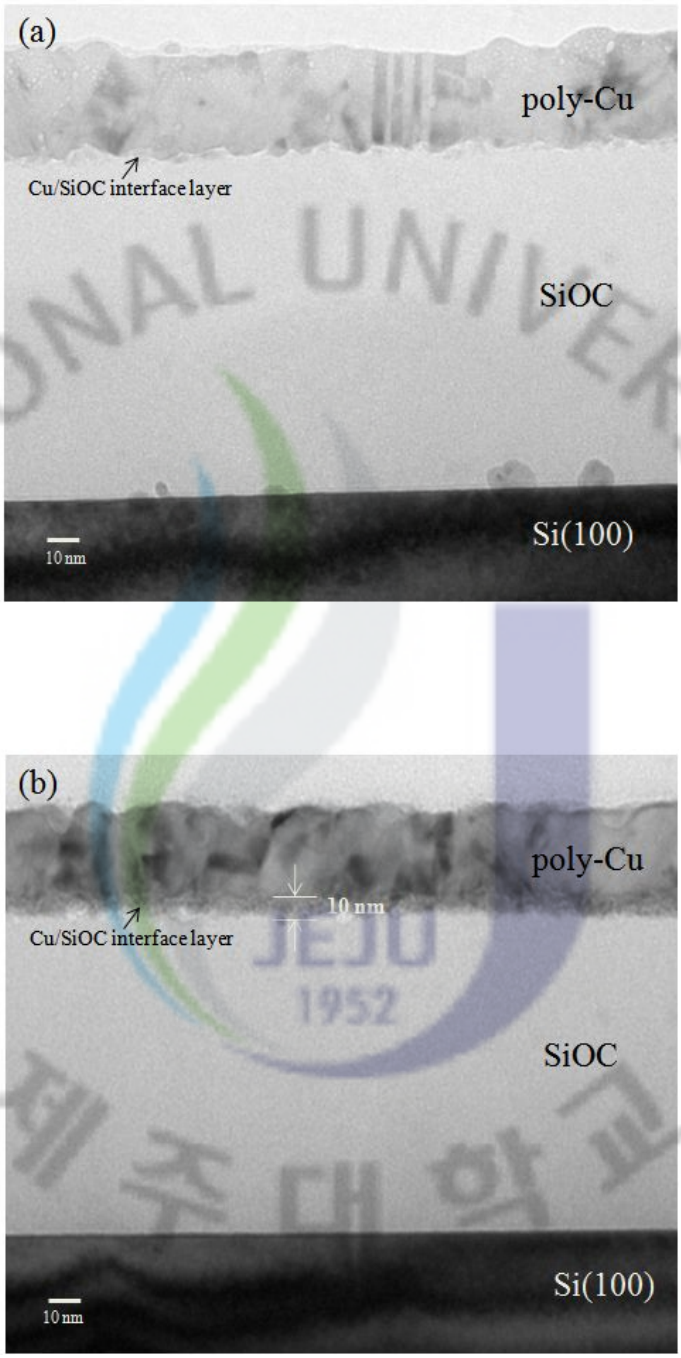

Fig. 55. HR-TEM image of the Cu/SiOC(-H)/*p*-Si(100) interface structure for (a) Non-BTS, and (b) after annealed at 450 °C with BTS.

3. Electrical conduction at the Cu/SiOC(-H)/*p*-Si(100) MIS structures

Cu interconnect processes make large demands on a dielectric material''s integrity, such as with standing increasingly aggressive bias temperatures and minimizing metal diffusion; otherwise, once metal ions penetrate into a low-*k* dielectric, the intrinsic dielectric property will dominate the electrical performance of the interconnecting system [98-101]. An important reliability issue associated with low-*k* materials is the high leakage current. Knowledge of the nature of the carrier transport could provide insight into leakage behavior and into the origin of the breakage processes. Thus, the intrinsic electrical characteristics of low-*k* dielectrics are an important factor for reliability and must be carefully assessed. In this session, the electrical conduction mechanisms of Cu/SiOC(-H)/*p*-Si(100) MIS structures were investigated using their temperature dependent I-V characteristics.

Figure 56(a) shows the I-V characteristics of as deposited and annealed Cu/SiOC(-H)/*p*-Si(100) MIS structures for various measurement temperatures. Most of the MIS structures did not show breakdown until operating the electric field up to 3.7 MV/cm, excepting the as-deposited structure measured at 200 °C. This result demonstrates that the annealing process (up to 450 °C) prevents breakdown even at higher electric fields because annealing significantly changes the number of Si-OH bonds and the amount of moisture trapped in the SiOC(-H) films, which influences the orientation of the polarization in the film [102] and thus improves the interface property. However, the leakage current densities of the as-deposited and the annealed samples were found to increase with both increased annealing and measurement temperatures. For example, the leakage current densities at 2 MV/cm were 1.05×10^{-9} and 6.18×10^{-7} A/cm^2 for the as-deposited and the annealed Cu/SiOC(-H)/*p*-Si(100) MIS structures, respectively. On the other hand, a significant increase (of about one order of magnitude) of the leakage current density with increasing measurement temperature was observed for the annealed samples, as shown in Fig. 56(a).

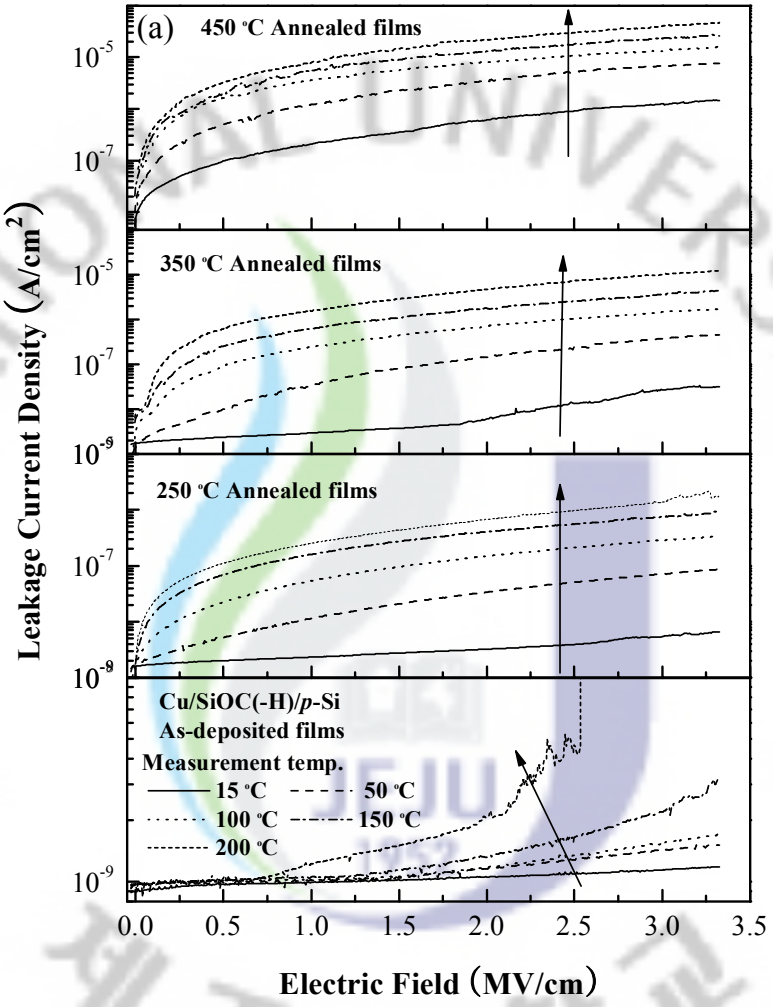

Fig. 56. (a) Leakage current density of as-deposited and annealed Cu/SiOC(-H)/*p*-Si(100)/Al MIS structures as a function of applied electric field measured at different temperatures and (b) plot of the leakage current density of the MIS structures at an applied field of 2 MV/cm as a function of the measurement temperature.

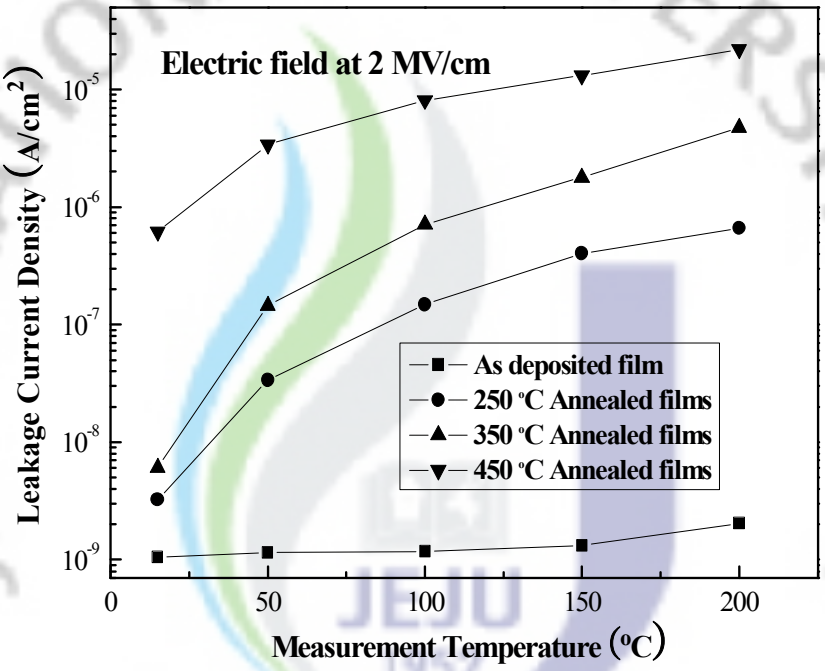

The the leakage current density of the samples with annealed temperature of RT, 250, 350 and 450 °C increased from 1.05×10^{-9} to 2.04×10^{-9} A/cm^2, from 3.24×10^{-9} to 6.65×10^{-7} A/cm^2, from 6.04×10^{-9} to 4.75×10^{-6} A/cm^2 and from 6.18×10^{-7} to 2.19×10^{-5} A/cm^2 as a function of the stress temperature. This result is attributed to the higher number of the Cu^+ ions that had diffused into the SiOC(-H) dielectric film due to high diffusivity at elevated temperatures. The leakage current increases with annealing temperature due to thermally excited energetic electrons in the dielectric film. The current densities of the Cu capacitors were about two or three orders of magnitude higher than those of the Al capacitors, as we have previously described [103]. It has been speculated that the Si-CH_3, Si-H, Si-OH, and -Si$(CH_3)_3$ bonds incorporated in the DMDMS precursor can be broken in the thermally-induced SiOC(-H) dielectric films, which in turn can significantly affect the interfacial properties and cause an increase in copper diffusion [104]. Figure 56(b) shows the leakage current density at an applied electric field of 2 MV/cm as a function of the measurement temperature for as-deposited and annealed MIS structures. The as-deposited MIS structures showed an almost constant leakage current density as 1.5×10^{-9} A/cm^2 for various measurement temperatures. However, the annealed MIS structures showed a rapid increase of the leakage current density (by about one to two orders of magnitude) with increasing measurement temperature. This is an important result because Cu has a high diffusivity at higher temperatures and requires a diffusion barrier between the Cu and the SiOC(-H) films [105,106].

The conduction mechanism of the Cu capacitor was investigated by examination of the J-E data in terms of the Schottky emission (SE) and the Poole-Frenkel (PF) mechanisms. The SE generated by the thermionic effect is caused by electron transport across the potential energy barrier via field-assisted lowering at a metal-dielectric interface [49]. The PF emission is due to field-enhanced thermal excitation of trapped electrons from the insulation into the conduction band [49]. Figures 57 show the leakage current densities (J) versus $E^{1/2}$ of the as-deposited and the annealed Cu/SiOC(-H)/*p*-Si(100) MIS structures measured at various ,

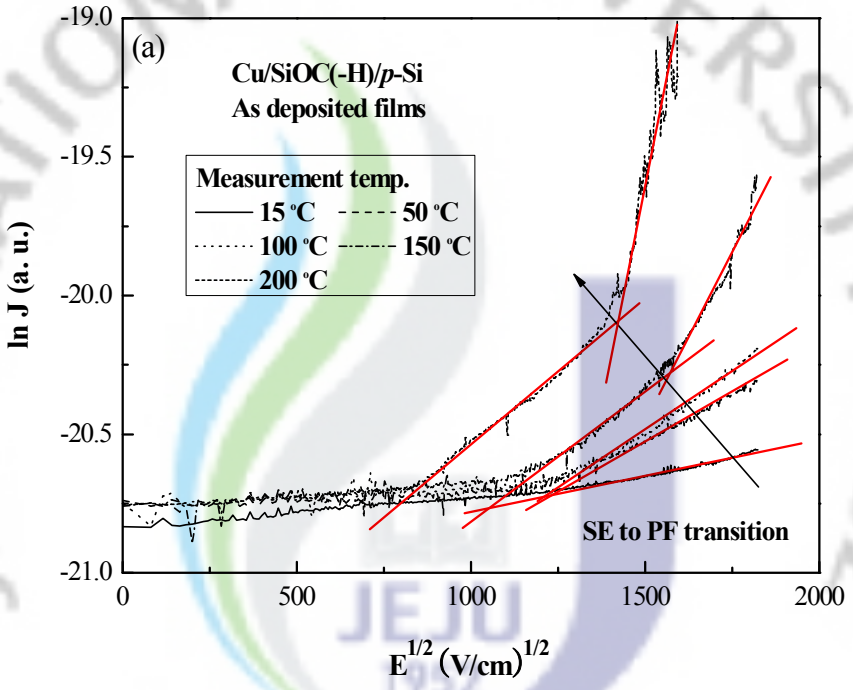

Fig. 57. Leakage current density (J) versus $E^{1/2}$ of Cu/SiOC(-H)/*p*-Si(100)/Al measured at different temperatures for (a) as-deposited and (b) annealed MIS structures.

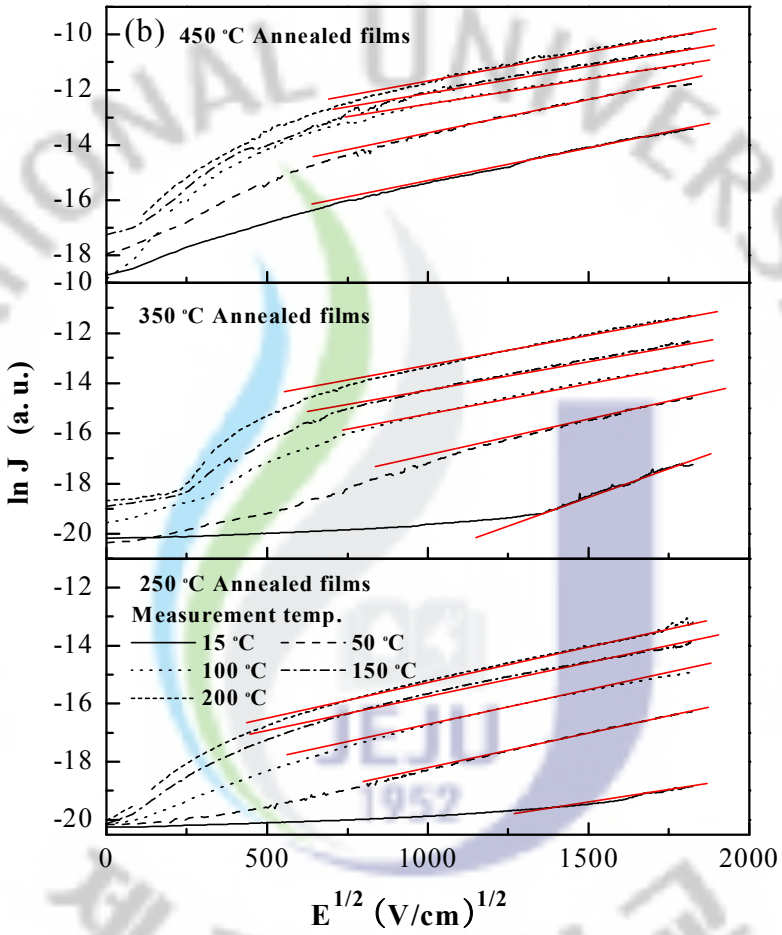

temperatures, respectively. As shown in Fig. 57(a), a linear relationship was obtained from the $\ln J$ versus $E^{1/2}$ plot suggesting SE for mid-range electric fields (0.5 to 2.25 MV/cm) and the PF mechanism at higher electric fields (beyond 2.25 MV/cm) [107]. The as-deposited MIS structure underwent a current transition from SE to PF conduction. The current transition from SE to PF conduction of the samples with the stress temperature of 150 °C and 200 °C has became as 2.5 and 2.0 MV/cm. However, in the case of annealed Cu/SiOC(-H)/*p*-Si(100) MIS structures, only the SE mechanism dominated, and the structures did not show any PF emission (see in Fig. 57(b)). Moreover, the temperature-dependent I-V measurements clearly demonstrated the effect of Cu drift diffusion on the electrical properties of the porous SiOC(-H) films. The leakage current densities of the two conduction mechanisms are expressed as follows [49];

For Schottky emission;

$$J = A^{*} T^{2} \exp\left(\frac{\beta_{SE} E^{1/2} - \phi_{SE}}{k_B T}\right), \tag{63}$$

$$\beta_{SE} = (e^3/4\pi\epsilon_0\epsilon)^{1/2}. \tag{64}$$

where e is the electronic charge, ϵ_0 is the dielectric constant of free space, ϵ is the high- frequency relative dielectric constant, A^{*} is the effective Richardson's constant, T is the absolute temperature, ϕ_{SE} is the contact potential barrier height at the surface, and k_B is Boltzmann's constant.

For the PF-dominated current density, we have

$$J = J_0 \exp\left(\frac{\beta_{PF} E^{1/2} - \phi_{PF}}{k_B T}\right), \tag{65}$$

$$\beta_{PF} = (e^3/\pi\epsilon_0\epsilon)^{1/2}. \tag{66}$$

where $J_o = \sigma_o E$ is the low field current density, σ_o is the low field conductivity, and ϕ_{PF} is the potential barrier height of the trap potential well. The PF transport mechanism is a result of a lowering of the barrier height of traps in the dielectrics. In order to determine which mechanism was dominant, the theoretical and the experimental values of β_{SE} and β_{PF} were extracted and compared (see Tables 8 and 9). The theoretical values were calculated using Eqs. (63) and (60), taking the measured dielectric constant of the SiOC(-H) films as the k value. The theoretical and the experimental values of β_{SE} and β_{PF} are listed in Tables 8 and 9. We observed only the SE mechanism in our MIS structures; we did not measure the experimental value of β_{PF}.

By rearranging Eq. (63) into a relationship between $\ln J/T^2$ and $1/T$, we calculated the Schottky barrier height (ϕ_{PF}) as follows:

$$\ln \frac{J}{T^2} = \ln A^* - \frac{1}{T}\left(\frac{\phi_{SE}}{k_B} - \frac{\beta_{SE}\sqrt{E}}{k_B}\right) \tag{67}$$

Table 8. The values of the dielectric constant and the constant β for Cu/SiOC(-H)/*p*-Si MIS structures.

Annealing Temperature (℃)	**Experimental ϵ (C-V)**	**Theoretical β_{SE} (× 10^{-24} J $cm^{1/2}/V^{1/2}$)**	**Theoretical β_{PF} (× 10^{-24} J $cm^{1/2}/V^{1/2}$)**
R.T	1.99	4.29	8.59
250	2.14	4.15	8.30
350	2.70	3.69	7.39
450	3.07	3.46	6.93

Table 9. The experimental values of β_{SE} ($\times 10^{-24}$ J cm$^{1/2}$/V$^{1/2}$) for as-deposited and annealed Cu/SiOC(-H)/*p*-Si MIS structures measured at various temperatures.

Annealing Temperature (℃)	Experimental β_{SE} (× 10^{-24} J cm$^{1/2}$/V$^{1/2}$) Current measurement temperature (℃)				
	15	50	100	150	200
R.T.	3.97	3.88	4.92	7.23	7.61
250	3.73	3.72	3.84	3.91	3.70
350	4.23	3.73	3.71	3.75	3.77
450	3.78	3.75	3.69	3.74	3.81

Figure 58 shows the temperature dependence of the SE dominated leakage current of the as-deposited and the annealed Cu/SiOC(-H)/*p*-Si(100) MIS structures. The $\ln J/T^2$ versus $1/T$ plot shown in Fig. 58 clearly fits a straight line, as expected for a thermionic emission. The $\ln J/T^2$ values of all samples decreased as a function of stress temperature $1/T$. The Schottky barrier height could be calculated from a slope of the $\ln J/T^2$ versus $1/T$ plot. Figure 59 shows the relationship between the Schottky barrier height and the annealing temperature used for the Cu/SiOC(-H)/*p*-Si(100) MIS structures. The the Schottky barrier height of the samples annealed at temperature of RT, 250 °C, 350 °C and 450 °C obtained 0.326, 0.281, 0.233 and 0.145 eV. The value of ϕ_{SE} decreases with increasing annealing temperature. The trap height of the PF conduction mechanism for the as-deposited Cu/SiOC(-H)/*p*-Si(100) MIS structure was calculated to be 0.365 eV, which is higher than the Schottky barrier height of 0.325 eV. As there was no noticeable PF mechanism in the annealed MIS structures, we could not calculate the PF trap height for those samples. Many factors affect the barrier height, such as the work function

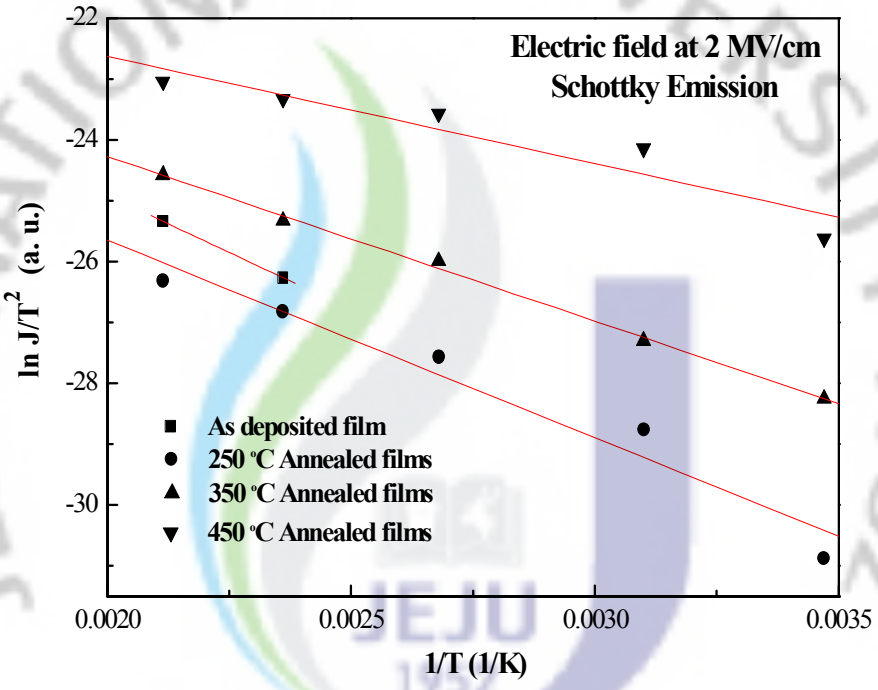

Fig. 58. Temperature dependence of as-deposited and annealed Cu/SiOC(-H)/*p*-Si(100)/Al MIS structures with a SE-dominated leakage current at an electric field of 2 MV/cm.

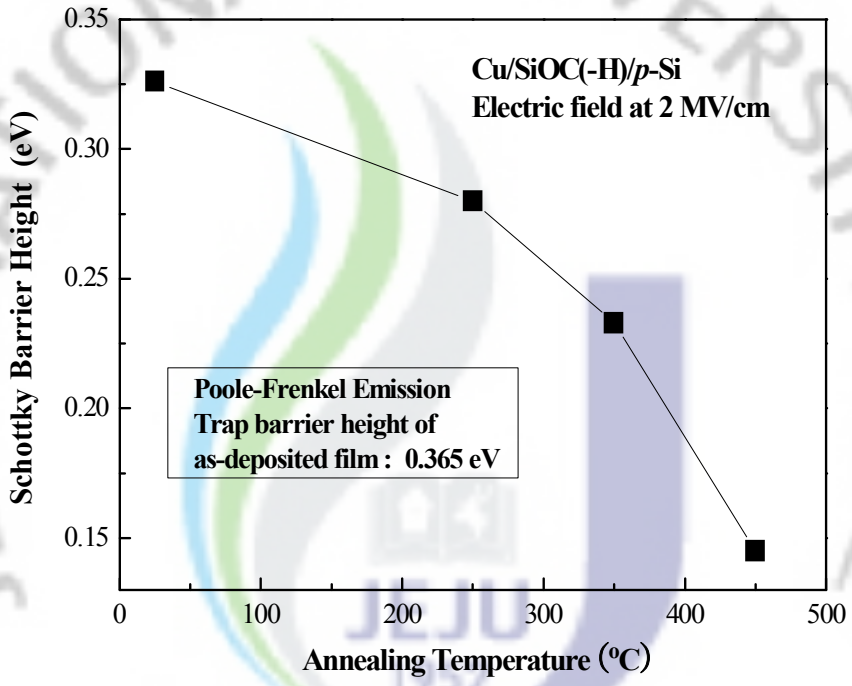

Fig. 59. Schottky barrier height as a function of annealing temperature.

of the electrode metal, the electron affinity of the dielectric film, and the surface states. Nevertheless, the decrease in barrier height and the increase in both the leakage current density and the dielectric constant of the SiOC(-H) film are attributed to the penetration of Cu^+ ions.

In order to evaluate electrical conduction at much higher temperatures, the samples annealed at temperature of 500 °C. Figure 60 shows the leakage current density of the Cu/SiOC(-H)/*p*-Si(100) MIS structures annealed at 500 °C measured at various temperatures. All samples showed a breakdown voltage. The breakdown field strength decreased with increasing measurement temperature, as shown in Fig. 60. The breakdown field is about 2.35, 2.06, 1.91, 1.87 and 1.59 MV/cm for the measurement temperature of 15 °C, 50 °C, 100 °C, 150 °C and 200 °C. Therefore, the breakdown field of the sample measured at low temperature was much higher than that measured at high temperature. These results are attributed to the injection of Cu^+ ions into the SiOC(-H) dielectric film, thereby deteriorating the film's quality. The leakage current density and the electrical degradation originated either from bond (Si-H and Si-OH) breakage of the SiOC(-H) dielectric film due to Cu^+ ion drift or from impact ionization due to injected electrons. The inset of Fig. 60 shows a plot of $\ln J/E^2$ as a function of $1/E$. Linear regions were obtained beyond electric fields in the range between 1.2 and 2 MV/cm, corresponding to various measurement temperatures, indicating Fowler-Nordheim (FN) tunneling just prior to dielectric breakdown. Table 10 shows the FN tunneling region corresponding to various measurement temperatures. Tunneling plays an important role in dielectric breakdown, and the high thermal (annealing and measurement temperature) stress in the tunneling region is a major cause of the dielectric breakdown in the SiOC(-H) film [108,109].

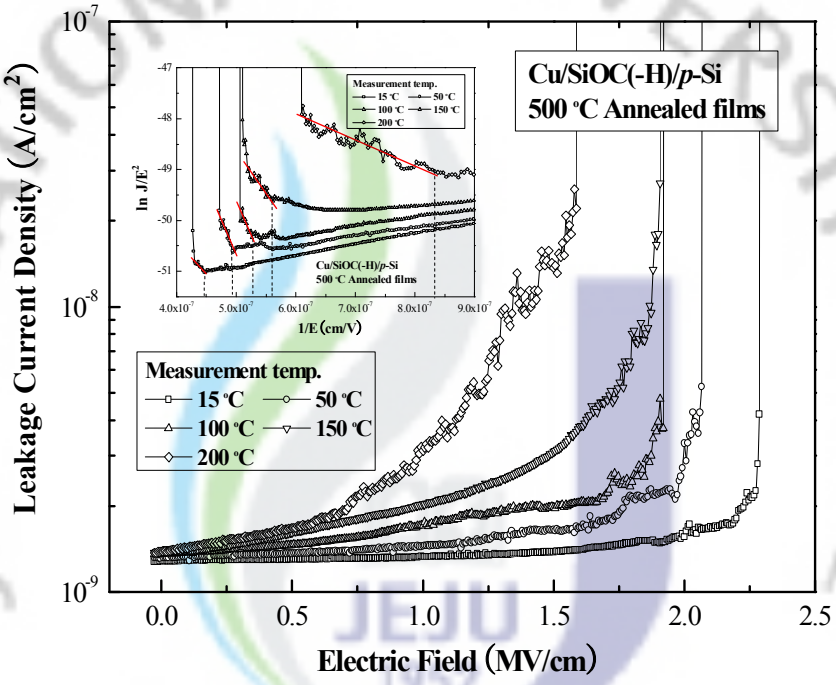

Fig. 60. Leakage current density of the Cu/SiOC(-H)/*p*-Si(100)/Al MIS structure annealed at 500 °C as a function of the applied electric field measured at different temperatures (inset: plot of $\ln J/E^2$ versus $1/E$ showing Fowler-Nordheim tunneling prior to dielectric breakdown).

Table 10. Fowler-Nordheim tunneling region of the Cu/SiOC(-H)/*p*-Si MIS structures annealed at 500 ℃ for various measurement temperatures.

Current measurement temperature (°C)	**Fowler-Nordheim tunneling region field (MV/cm)**
15	2.22 ~ 2.28
50	1.62 ~ 2.06
100	1.34 ~ 1.91
150	1.06 ~ 1.87
200	0.68 ~ 1.59

Chapter Ⅶ. Frequency Dependent C-V and G/ω-V Characteristics of Low-*k* SiOC(-H) Films

The physical and the electrical properties of MIS structures strongly depend on the preparation conditions of the films and on the formation of interfacial layers. In addition to I-V measurements, the C-V and the G/ω-V characteristics of MIS structures have been extensively studied to determine the effects of the interfacial layer on the characteristics of MIS structures [110-114]. The electrical properties at the interface of a low dielectric/semiconductor SiOC(-H)/*p*-Si(100) structure are known to influence the characteristics of the device. The performance of an MIS structure depends on various factor, such as the presence of localized interface states at the SiOC(-H)/*p*-Si(100) interface, cleaning, the interface preparation process, the metal to-semiconductor barrier height, the interfacial dielectric layer formation, and the series resistance [115,116]. Therefore, if these issues are to be better understood, a more detailed investigation of the interface state of the SiOC(-H)/*p*-Si(100) structure based on frequency dependence is required. In this session, the electrical and the dielectric properties of an Al/SiOC(-H)/*p*-Si(100)/Al MIS structure were studied using C-V and G/ω-V measurements over a frequency range from 1 kHz to 5 MHz. We examined the frequency dependence of the Al/SiOC(-H)/*p*-Si(100)/Al MIS structure and calculated the series resistance, the dielectric constant, the dielectric loss, the loss tangent, and the ac electrical conductivity by applying the admittance method.

Figures 61(a) and (b) show the frequency dependence measurements of the C-V and G/ω-V characteristics of Al/SiOC(-H)/*p*-Si(100)/Al structures at room temperature, respectively. As shown in Fig. 61(a), each C-V curve has three regimes of accumulation-depletion-inversion region, but with a considerable voltage-axis shift due to the presence of interface states. The flat band voltage shifted more towards the

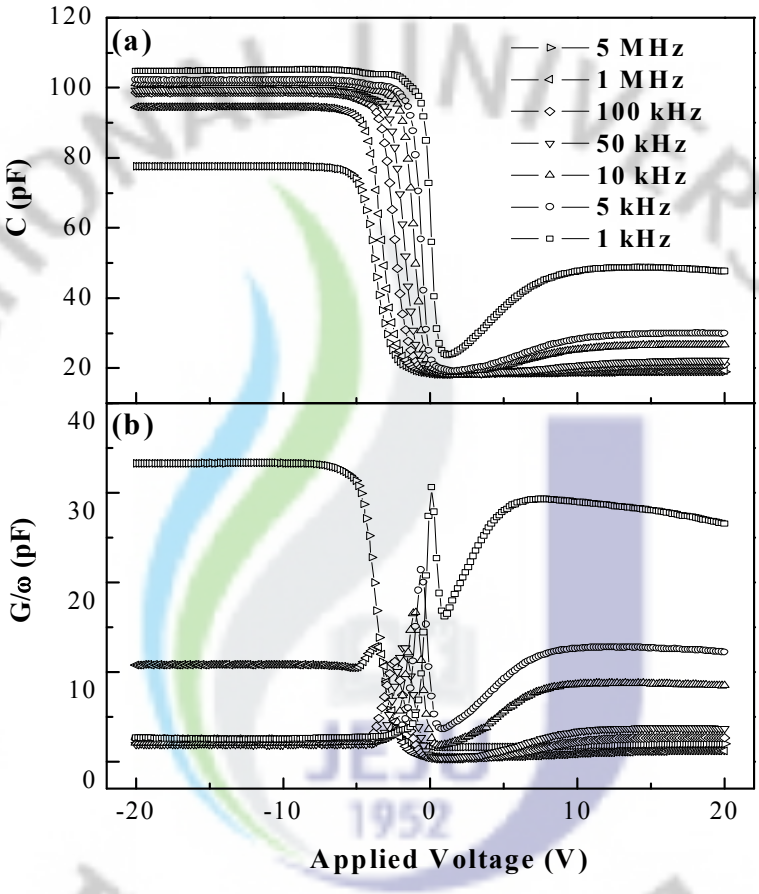

Fig. 61. (a) C-V and (b) G/ω-V characteristics of the Al/SiOC(-H)/*p*-Si(100)/Al MIS structures measured at different frequencies.

negative region of the C-V curve with increasing measurement frequency. In the accumulation region for a given applied bias voltage, the capacitance increases with decreasing measurement frequency. The capacitance of such an inhomogeneous layer at the semiconductor-dielectric interface [*p*-Si(100)/SiOC(-H)] acts in series with the dielectric capacitance, thus causing frequency dispersion. This effect occurs because at lower frequencies the interface states can follow the ac signal and yield an excess capacitance, which depends on the frequency. The applied ac signal causes the Fermi level to oscillate about the mean positions governed by the dc bias, when the MIS structure is in the depletion region [117]. In the high-frequency limit ($f \geq 100$ kHz), however, the interface states cannot follow the ac signal. This makes the contribution of the interface state capacitance to the total capacitance negligibly small [117]. As can be seen in Fig. 61(b), the values of conductance give a peak in each frequency of about -1 V. Such a behavior of the G/ω peaks was attributed to a particular distribution of interface states between SiOC(-H)/*p*-Si(100) interface. Additionally, appreciable frequency dependent dispersion is evident at the depletion region. As shown in Figs. 61(a) and (b), C and G/ω are more sensitive to frequency, at relatively low-frequencies, the value of C decreases with increasing frequency whereas the value of G/ω increases with increasing measurement frequency. The values of various parameters for the MIS structures were determined from the C-V and G/ω-V characteristics at various measurement frequencies at room temperature and are given in Table 11. As shown in Fig. 61(a), the capacitance of the Al/SiOC(-H)/*p*-Si(100)/Al MIS structure was strongly dependent on the values of series resistance (R_s), the density of interface states (N_{ss}) and the frequency of the ac signal superimposed on the dc applied bias (see Table 11). The higher values of C at low frequencies are due to excess capacitance (C_o) resulting from the N_{ss} in equilibrium with Si. In order words, at low frequencies, the N_{ss} state can follow the ac signal and consequently do contribute appreciably to the MIS capacitance. The G/ω-V characteristics of the MIS structure at different frequencies (in Fig. 61(b)) increase

Table 11. The values of various parameters for Al/SiOC(-H)/*p*-Si(100)/Al MIS structures determined from C-V and G/ω-V characteristics at the different frequencies.

f (kHz)	V_m (V)	C (F)	G/ω (F)	N_{ss} ($eV^{-1}cm^{-2}$)	R_s (Ω)
1	0.1	5.59×10^{-11}	3.06×10^{-11}	3.99×10^{12}	1.19×10^{6}
5	-0.6	5.67×10^{-11}	2.14×10^{-11}	3.05×10^{11}	185509
10	-0.9	4.96×10^{-11}	1.67×10^{-11}	1.82×10^{11}	96640
50	-1.8	6.11×10^{-11}	1.27×10^{-11}	2.42×10^{11}	10399
100	-2.6	6.52×10^{-11}	1.09×10^{-11}	2.69×10^{11}	3982
1000	-3.6	7.09×10^{-11}	1.28×10^{-11}	5.80×10^{11}	394
5000	-4.8	7.26×10^{-11}	3.08×10^{-11}	2.11×10^{13}	195

with increasing frequency. These behaviors may be different at low and intermediate frequencies, depending on the relaxation time the of N_{ss} states and the frequency of the ac signal. From the above discussion, it can be concluded that under applied bias voltage (V), the interface states are responsible for the observed frequency dispersion in C-V and G/ω-V curves. Depending on the relaxation time of the interface states and the frequency of the ac signal, there may be a capacitance due to interface states in excess of the depletion layer capacitance.

In order to extract the value of R_s in the MIS structures, several methods have been suggested [118,119] and we have used the following expression to calculated the R_s,

$$R_s = \frac{G_{ma}}{G_{ma}^2 + (\omega C_{ma})^2} \quad . \tag{68}$$

Where C_{ma} and G_{ma} represent the measured capacitance and conductance, respectively in the strong accumulation region. By comparing the imaginary and real part of the corrected admittance one can obtain the corrected capacitance (C_c) and conductance (G_c) as the following [118],

$$C_c = \frac{[G_m^2 + (\omega C_m)^2]C_m}{a^2 + (\omega C_m)^2}, \tag{69}$$

$$G_c = \frac{G_m^2 + (\omega C_m)^2 a}{a^2 + (\omega C_m)^2}. \tag{70}$$

where

$$a = C_m - [G_m^2 + (\omega C_m)^2]R_s \tag{71}$$

In this study, The value of R_s for the Al/SiOC(-H)/*p*-Si(100)/Al structures for the various experimental parameters was calculated. Figure 62(a) shows the R_s as a function of applied voltage for the various frequencies. As can be seen in Fig. 62(a), the R_s gives a peak depending on the frequency in the voltage range about -1 to 1 V and this peak disappears at sufficiently high frequencies. Also, we obtained the frequency dependent R_s at various reverse bias voltages as shown in Fig. 62(b). It is clearly seen in Fig. 62(b) that the R_s is independent of voltage at high frequencies ($f \geq 50$ kHz). As a result of that, we can say that at sufficiently high frequencies the N_{ss} states cannot follow the ac signal and consequently cannot contribute to the MIS capacitance.

In order to obtain the real MIS capacitance and conductance or correction capacitance (C_c) and conductance (G_c/ω), at two different high frequencies for both the C-V and G/ω-V characteristics measured under forward and reverse biases, were corrected for the effect of R_s by using Eqs. (69) and (70).

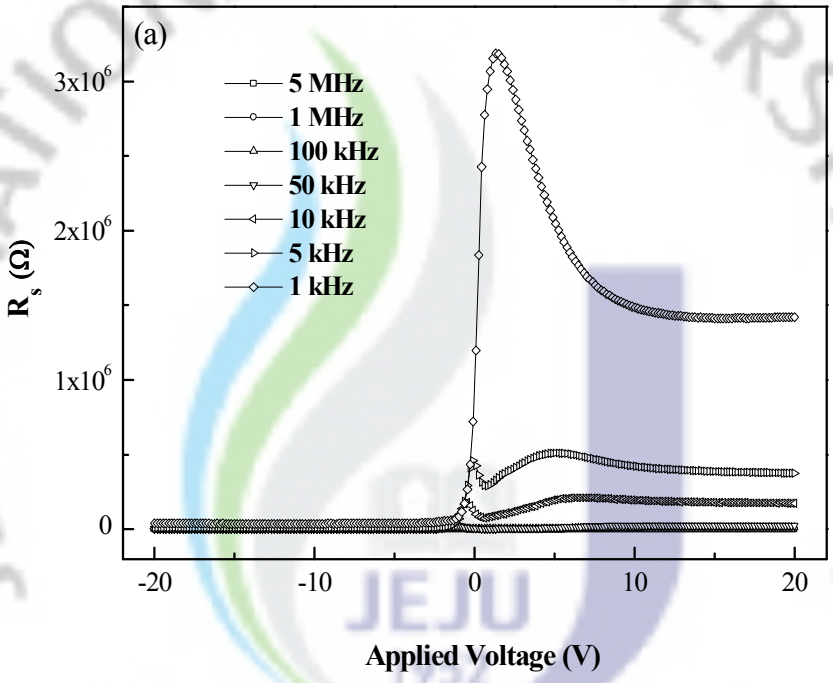

Fig. 62. The variation of R_s as a function of (a) applied voltage for various frequencies and (b) frequency for various voltages.

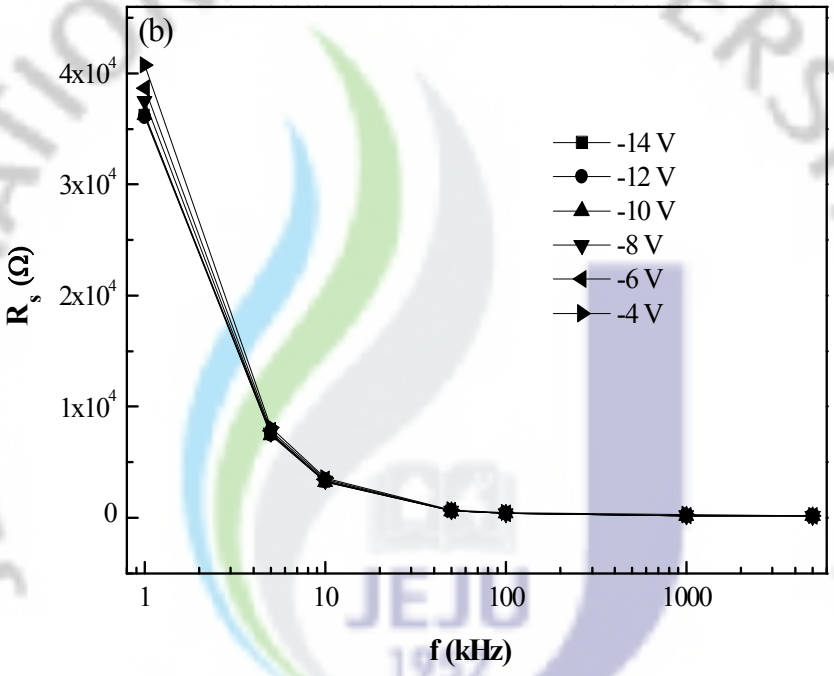

Figures 63(a) and (b) show the voltage dependent plot of the corrected C_c-V and G_c/ω-V for two frequencies (1 and 5 MHz), respectively. When the correction was made on the C-V plot for the effect of R_s, the values of the corrected capacitance almost remains the same with decreasing voltage, especially under reverse bias. The accumulation region is shown enlarged in the inset of Fig. 63(a). On the other hand, the plot of the corrected conductance increased slightly with decreasing voltage, especially under reverse bias. The accumulation region is shown enlarged in the inset of Fig. 63(b). The plot of the corrected conductance gives a small peak, proving that the charge transfer can take place through the interface. The frequency and applied voltage dependence of the dielectric constant (ϵ'), dielectric loss (ϵ''), dielectric loss tangent ($\tan\delta$) and ac electrical conductivity (σ_{ac}) of Al/SiOC(-H)/Si/*p*-Si(100) structures were determined for the various frequencies from the following expressions [120,121].

$$\epsilon' = \frac{C_{ox}}{C_0} \tag{72}$$

where

$$C_0 = \epsilon_0 (A/d_{ox}) \tag{73}$$

A is the area of the sample, d_{ox} is the interfacial dielectric layer thickness and ϵ_0 is the permittivity of free space (ϵ_0=8.85×10^{-14} F/cm). In the strong accumulation regions, the maximum capacitance of the MIS structure corresponds to the oxide capacitance ($C_m = C_{ox}$). The imaginary part of the dielectric loss (ϵ'') is determined from the knowledge of the measured conductance G_m by use of the following relation,

$$\epsilon'' = \frac{G_m}{C_0 \omega}, \tag{74}$$

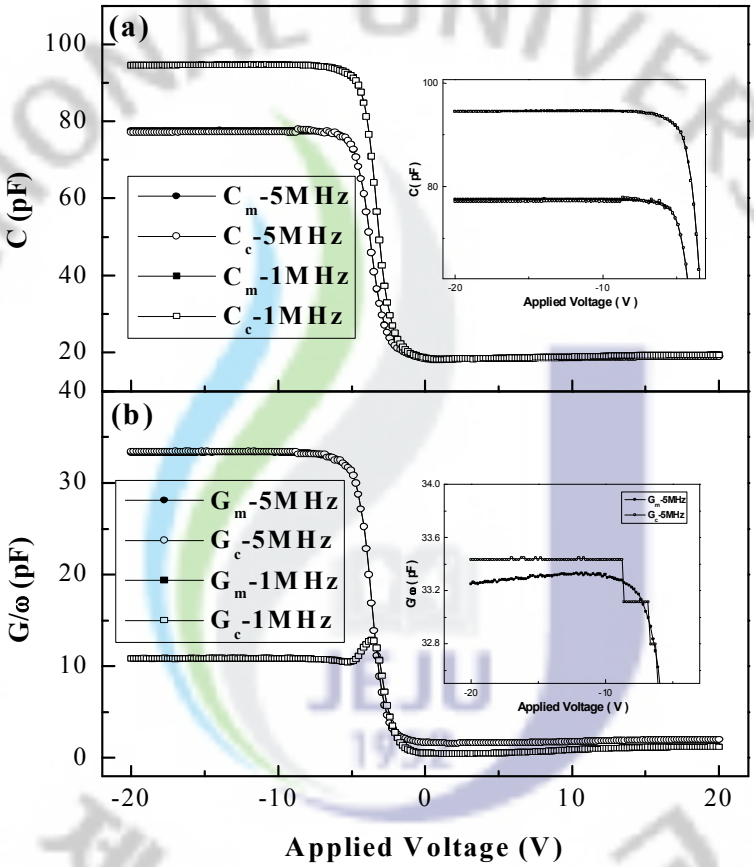

Fig. 63. The voltage dependent plot of the corrected (a) C-V and (b) G/ω-V for the frequencies 1 and 5 MHz. Inset showing the enlarged part of the accumulation region.

Then the dielectric loss tangent ($\tan\delta$) was calculated from the relation,

$$\tan\delta = \frac{\epsilon''}{\epsilon'}, \tag{75}$$

and, the ac electrical conductivity (σ_{ac}) was evaluated using the following expression,

$$\sigma_{ac} = \omega C \tan\delta (d/A) = \epsilon'' \omega \epsilon_0. \tag{76}$$

The frequency dependence of the ϵ', ϵ'' and $\tan\delta$ of the Al/SiOC(-H)/*p*-Si(100)/Al MIS structures are presented in Figs. 64(a) and (b), respectively. From the calculated values of capacitance and conductance, the values of the ϵ', ϵ'' and $\tan\delta$ were found to be strongly influenced by the measurement frequency. As can be seen from the Fig. 64(a), the value of ϵ' decreases with increasing frequency whereas the dielectric loss ϵ'' showed an opposite trend to that of the ϵ'. This is the normal behavior of a dielectric material [SiOC(-H)]. The value of ϵ' and ϵ'' were found to be of 2.68 and 0.07 measured at 1 kHz. This result shows that the strong low-frequency dispersion, that characterizes the frequency dependence for the ϵ' and ϵ'' of Al/SiOC(-H)/*p*-Si(100)/Al MIS structures which is in consistent with the data as shown in Fig. 64(a). However, in general, there are four possible mechanisms that may be contribute to the low-frequency dielectric behavior of MIS structures. These mechanisms involve the electrode interface, the ac electrical conductivity, the dipole-orientation and the charge carriers [117]. In principle, at low-frequencies and temperature, all the four types of polarizations processes, i.e., the electronic, ionic, dipolar, and space charge polarization contribute to the values of ϵ' and ϵ''. On raising the frequency, the contributions of the space charge, dipolar or the ionic polarization become ineffective leaving behind only the electronic part. Furthermore, the decrease in ϵ' with increasing frequency can be explained by the fact that as the

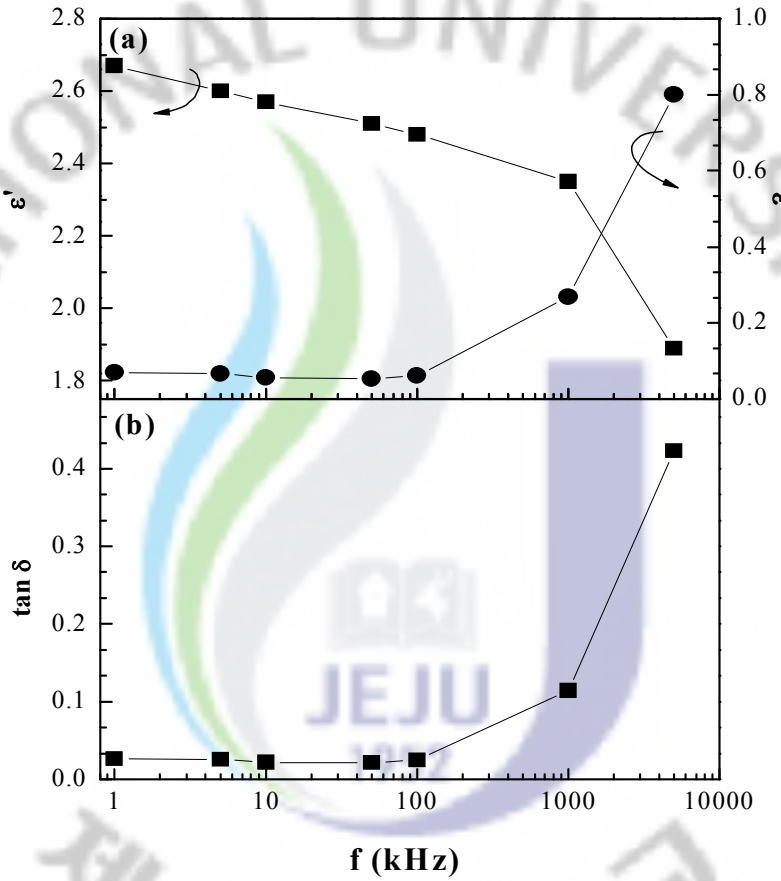

Fig. 64. The frequency dependence of (a) dielectric constant (ϵ'), dielectric loss (ϵ'') and (b) dielectric tangent ($\tan\delta$), respectively, for Al/SiOC(-H)/*p*-Si(100)/Al structures at room temperature.

frequency was raised, the space charge polarization had less time to orient themselves in the direction of the alternating current field. However, the value of ϵ'' increases with increasing frequency, which can be attributed to the high interface traps formed at the SiOC(-H)/*p*-Si(100) interface that adversely influences the electrical properties [117]. In our work, we can conclude that the Si-O bonds can be converted to Si-C by addition of the -CH_3 groups giving rise to compensation of the positive and negative charges at the interface, as a result, the reduction of interface states arises [122,123]. The variation of the loss tangent ($\tan\delta$) with respect to frequency of Al/SiOC(-H)/*p*-Si(100)/Al MIS structure is shown in Fig. 64(b). As shown in Fig. 64(b), the value of $\tan\delta$ increases with increasing frequency in the range of 1 kHz to 5 MHz. Theses experimental results revealed that the values of the ϵ', ϵ'' and $\tan\delta$ had a strong dependence on the measurement frequency. The capacitance of the MIS structure at high frequencies in the accumulation region is controlled basically by the dielectric properties of the bulk insulator [124].

Figure 65 illustrates the dependence of the ac electrical conductivity on the frequency. This figure depicts the variation of the ac electrical conductivity (σ_{ac}) with frequency (in the frequency range 1 kHz-5 MHz) at room temperature for the Al/SiOC(-H)/Si/*p*-Si(100) MIS structure. It was found that the ac electrical conductivity generally increases with increasing frequency and especially of note was the sharp increase in σ_{ac} after about 1 MHz. Similar behavior was also observed in previous literature [124-126]. This behavior can be attributed to a gradual decrease in R_s with increasing frequency.

The C and G/ω of Al/SiOC(-H)/Si/*p*-Si(100) structure as a function of frequency at a fixed gate voltage was measured. Figures 66(a) and (b) show the capacitance (C) and conductance (G/ω) in the depletion and the weak inversion region as a function of frequency in the voltage range from 0 to 5 V in steps of 1 V. As can be seen from Figs. 66(a) and (b), the measured values of C and G/ω at the depletion region decrease with increasing frequency in the frequency range of 1 kHz to 1 MHz. From

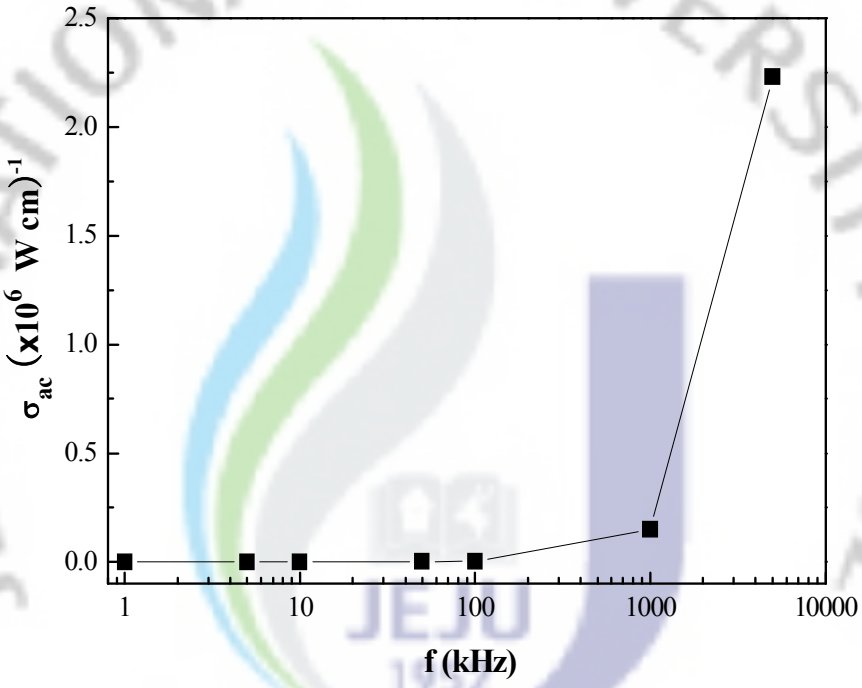

Fig. 65. The frequency dependence of the ac electrical conductivity (σ_{ac}) for Al/SiOC(-H)/*p*-Si(100)/Al structures at room temperature.

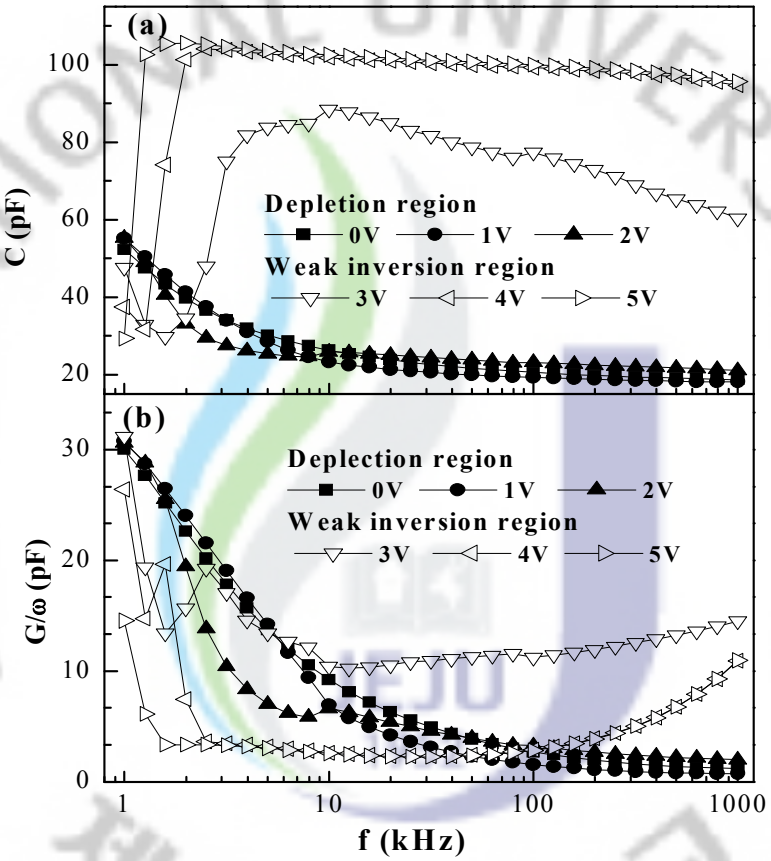

Fig. 66. The frequency dependence of (a) C-f and (b) G/ω-f characteristics of Al/SiOC(-H)/p-Si(100)/Al structures measured at depletion and weak inversion regions.

this figure, it was observed that the changes in C and G/ω take place over a wide frequency range. Also the measured C in the weak inversion region increased rapidly at low frequency and then decreased gradually for further increases in frequency. This behavior is attributed to the presence of a continuous distribution of N_{ss}, which leads to a progressive decreasing response of the N_{ss} with the applied ac voltage [127]. However, the measured G/ω follows a similar trend for both the depletion and weak inversion region in a decreasing manner with increasing frequency. In addition, the higher values of C and G/ω at low frequency are due to excess capacitance and conductance resulting from the N_{ss} states being in equilibrium with the semiconductor so that they can follow the ac signal. It can be concluded that under forward bias (0-5 V) the interface states are responsible for the observed frequency dispersion in the C-V and G/ω-V curves.

Figure 67 shows the variation R_s as a function of frequencies measured at the fixed gate voltages in the depletion and the weak inversion regions. Thus, R_s depends strongly on the applied voltage at a frequency less than 50 kHz. Also, at high frequencies, $f \geq 100$ kHz, the charges at the interface states cannot follow an ac signal. From this data, it is clearly seen that the R_s is dependent both frequency and voltage and changes from region to region. These behaviors suggest that the trap charges have enough energy to escape from the traps located at Al/SiOC(-H) interface in the Si band gap [128].

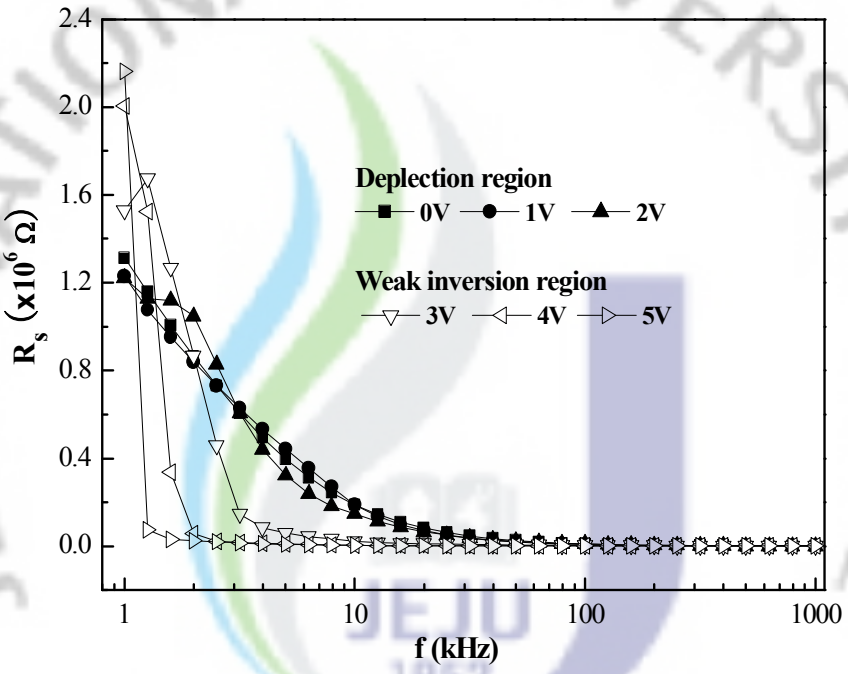

Fig. 67. The frequency dependence of R_s-f characteristics of Al/SiOC(-H)/p-Si(100)/Al structures measured at depletion and weak inversion regions.

Chapter Ⅷ. Conclusion

In this research, low-*k* SiOC(-H) thin films were deposited on *p*-Si(100) substrates by using PECVD with DMDMS precursor and oxygen gas precursors. The diagnostic of bulk plasma states were analyzed by the Langmuir probe and optical emission spectroscopy during the film deposition. The bonding characteristics and the chemical groups present in the SiOC(-H) films were investigated with FTIR spectroscopy in the absorbance mode and the XPS. I-V and C-V characteristics of the SiOC(-H) films were measured for the MIS structure, Cu(Al)/SiOC(-H)/*p*-Si(100), in order to study the interface behavior. Comparative studies concerning the structural and the electrical properties were discussed based on the formation of the SiOC(-H) film.

1) During the plasma polymerization, the reactive species are dissociated and then deposited on the Si substrate to form the SiOC(-H) film. As the rf power increased from 100 to 800 W, the corresponding N_e and T_e were found to be increased from 6.23×10^{8} to 1.22×10^{10} cm^{-3} and from 1.57 to 2.03 eV, respectively. This elevated electron density at higher rf powers leads to a higher deposition rate of the SiOC(-H) film. Also, a complete dissociation of the precursor had taken place for rf powers greater than 500 W. As a result of this process more radicals and ions had been created. From this result, we can infer that the electron density increase and more radicals are produced when the rf power is increased.

2) The FTIR spectra of all samples deposited with various conditions, such as flow rate ratio, rf power and substrate temperature, were generally broad and overlapping due to the complex stoichiometry and the amorphous nature of the films. The characteristic band of all SiOC(-H) films showed absorption bands due to Si-O-Si (around 1055 cm^{-1}), Si-O-C (around 1055 cm^{-1}), Si-CH_3 (around 950 and 1250 cm^{-1}), CH_n (1457 and 2955 cm^{-1}) and -OH (around 3200 to 3700 cm^{-1}) in addition to those of the Si substrate. There is a shoulder at 1150 cm^{-1} in all the absorption spectra, which was assigned to the broad Si-O-C peak corresponding to the Si-O-C cage-link

structure and resulting in a more porous nature in the SiOC(-H) film.

3) As the applied rf power was increased, the -CH_3 groups present in the DMDMS precursor dissociated into smaller reactive species such as CH, C and O, without the formation of CH_2 and CH_3 radicals and then the CH radical dissociated further into C, H_α, and H_β radicals, respectively. The O_2-Si-$(CH_3)_2$ and O_3-Si-CH_3, O_3-Si-$(CH_3)_3$ and C-C/C-H bonding configurations of the SiOC(-H) film increased in number with increasing rf power, whereas the Si-O_2 bond decreased in number. These bonding structures help to reduce the *k* value of the SiOC(-H) films. The dielectric constant of the SiOC(-H) films decreased as the rf power was increased due to the incorporation of Si-C related bonds attributed to the lower dipole polarizability. The film deposited with an rf power of 700 W showed the lowest dielectric constant of 2.21 and a refractive index of 1.33. Furthermore, the best leakage current density achieved was about 2.7×10^{-9} A/cm^2 at 1 MV/cm.

4) When the flow rate ratio was increased from 50 to 100%, chemical shifts were observed both in the FTIR and XPS data. An increase in the DMDMS precursor flow rate gives rise to a structural rearrangement through the addition more carbon atoms in the Si-O-Si network chain during the formation of the SiOC(-H) film. This result indicates that the cage-linked structures of the Si-O-C bond are able to produce a nano-porous structure, which results in a lower film density and, hence, a low dielectric constant. The electrical characterization of the SiOC(-H) films revealed improved properties with increasing precursor flow rate ratio. This effect indicates that the flow rate influences the formation of the interface and that with increasing of flow rate, the Si dangling bonds at the interface were decreased in number due to the incorporation of carbon atoms, which resulted in an improvement of the interface of the SiOC(-H)/*p*-Si(100) structure. A dielectric constant as low as 2.1 was obtained for the as-deposited SiOC(-H) films prepared with a flow rate ratio of 100%. The leakage current density was found to be 3.7×10^{-9} A/cm^2.

5) In order to investigated the influence of the substrate temperature on the properties of SiOC(-H) films, the films were deposited at various substrate

temperatures with an rf power of 700 W and a working pressure of 700 mTorr. The chemical and structural nature of these films was characterized by XPS and FTIR. The results obtained indicated that the SiOC(-H) films exhibit clearly distinguished bonds of the type Si-O-Si and Si-O-C. As the substrate temperature was increased the dielectric constant of the SiOC(-H) film also increased due to Si-C bonds being broken, leaving the film rich in Si-O bonds. The lowest dielectric constant and refractive index of the films deposited at room temperature were found to be 2.22 and 1.36, respectively.

6) The detailed mechanical properties of the SiOC(-H) thin films prepared with different substrate temperatures and deposited on *p*-type Si(100) substrates by using PECVD with DMDMS and oxygen gas as precursors. Nanoindentation studies were carried out to determine the mechanical properties of the SiOC(-H) films. The hardness and the elastic modulus of the SiOC(-H) films prepared with different substrate temperatures were measured to be in the range from 2.25 to 4.5 GPa and from 20 to 35 GPa, respectively. The values of the hardness and elastic modulus were observed to increase with increasing substrate temperature. From the analyses of a typical FTIR absorption spectra over the range of 400 to 4000 cm^{-1}, the SiOC(-H) films showed various bonding configurations, such as the Si-O-Si(C), the $Si-CH_3$, the -OH and the CH_n bonds in the films. This result implies that the $-CH_3$ group in the SiOC(-H) film, as an end group, was broken when the substrate temperature was increased, thereby reducing the film density and increasing the values of the measured mechanical properties.

7) The interface state density, the fixed charges, and the trapped charge density were calculated for the Cu/SiOC(-H)/*p*-Si(100)/Al and Al/SiOC(-H)/*p*-Si(100)/Al MIS structures under an electrical bias stress for different time durations. The positive shift of V_{fb} after applying bias stress implies that electron trapping has occurred for both Cu and Al metallization of the SiOC(-H) films. As the annealing temperature was increased, both the capacitance value and V_{fb} increased for the Cu and Al MIS structures. Both MIS structures revealed mostly a similar energy distribution of the

density of interface states before and after electrical bias stress for different durations. The fixed charge increased from 1.6×10^{12} to 2.5×10^{12} cm^{-2} for Cu/SiOC(−H)/*p*-Si(100)/Al structures and from 0.6×10^{12} to 2.7×10^{12} cm^{-2} for Al/SiOC(−H)/*p*-Si(100)/Al structures with increasing annealing temperature. This effect was caused by the stress-induced charges generated at the interface of the MIS structures. The interface state density of the Cu/SiOC(−H)/*p*-Si(100)/Al MIS structure gradually increased with both increasing annealing temperature and stressing duration. However, the interface state density of the Al/SiOC(−H)/*p*-Si(100)/Al MIS structure was not significantly affected by either the annealing temperature or the duration of the stress.

8) The diffusion phenomena of Cu^+ ions in the SiOC(-H) films with the Cu/SiOC(-H)/*p*-Si(100)/Al MIS structures after annealing was evaluated by C-V measurements with a flat-band shift caused by bias-temperature stress (BTS). The C-V curve revealed a shift in the V_{fb} due to Cu^+ ion diffusion in the SiOC(-H) dielectric film. The V_{fb} corresponding to the MIS structures annealed at 250, 350 and 450 °C with a BTS time of 40 min was -15, -18 and -34 V, respectively. The activation energies (E_a) of the Cu/SiOC(−H)/*p*-Si(100)/Al MIS structures under BTS at annealing temperatures of 250, 350 and 450 °C were 0.58, 0.26 and 0.22 eV, respectively. The diffused interface layer increased with increasing annealing temperature and BTS treatment. The drift diffusion experiments indicated that the Cu^+ ion drift rate in the SiOC(-H) films increased with increasing annealing temperature.

9) The electrical conduction mechanism of the as-deposited and the annealed Cu/SiOC(-H)/*p*-Si(100) MIS structure was considered as a function of the applied electric field measured at different temperatures, The leakage current densities of the as-deposited and the annealed MIS structures increased with both increased annealing and with increasing measurement temperature. The current densities of the Cu capacitors were about two or three orders of magnitude higher than those of Al capacitors. As-deposited MIS structures showed the two kinds of the electrical mechanisms; namely, SE mechanism for midrange electric fields (0.5 to 2.25 MV/cm) and PF emission mechanism at higher electric fields (beyond 2.25 MV/cm). In

contrast, the annealed MIS structures showed only SE conduction. The value of the Schottky barrier height decreased with increasing annealing temperature. The Schottky barrier height decreased from 0.326 eV for the as-deposited MIS structures and to 0.145 eV for the MIS structures annealed at 450 ℃. The PF barrier height for the as-deposited Cu/SiOC(-H)/*p*-Si(100) MIS structure was calculated to be 0.365 eV. All samples showed voltage breakdown after annealing at 500 ℃. The breakdown field strength decreased with increasing measurement temperature. Form these results and the FTIR analysis, we can infer that the leakage current density and electrical degradation originated either from the bond (Si-H and Si-OH) breakage of the SiOC(-H) dielectric film due to Cu^{+} ion drift or from the impact ionization due to injected electrons.

10) The series resistance, dielectric constant, dielectric loss, loss tangent and ac electrical conductivity of the Al/SiOC(-H)/*p*-Si(100)/Al MIS structures were calculated. R_s strongly depended on the applied voltage for frequencies less than 50 kHz. ϵ' decreased with increasing frequency whereas the dielectric loss ϵ'' showed a trend opposite to that of ϵ'. The values of ϵ' and ϵ'' were calculated as 2.68 and 0.07, respectively at 1 kHz. The ac electrical conductivity increased with increasing frequency. From these results, we knew that the behaviors of the dielectric properties of the SiOC(-H) film were strongly influenced by the frequency due to the presence of interface states, the fixed surface charge, and the series resistance of the Al/SiOC(-H)/*p*-Si(100)/Al MIS structure.

11) In our study, the high quality SiOC(-H) films formed at an rf power of 700 W and the flow rate ratio of 80% by using PECVD with DMDMS and oxygen gas. The SiOC(-H) films had a low dielectric constant of about 2.1, which the bonding structure have a cross-linking structure with nano-pore due to the combined Si-CH_n-Si bond and Si-O-Si network. Futhermore, we defined the interface charge phenomena and the Cu^{+} ion diffusion in the SiOC(-H) film at the Cu(Al)/SiOC(-H)/*p*-Si(100)/Al interface under electrical bias stress for different time durations.

References

[1] W. Volksen, R. D. Miller and G. Dubois, Chem. Rev., **110**, 56 (2010)

[2] M. T. Bohr, IEEE IEDM Tech. Dig., 241 (1995).

[3] M. Morgen, E.T. Ryan, J.H. Zhao, C. Hu, T. Cho and P.S. Ho, Annu. Rev. Mater. Sci., **30**, 645 (2000).

[4] Y. Xu, Y. Tsai, K.N. Tu, B. Zhao, Q.Z. Liu, M. Brongo, G.T.T. Sheng and C.H. Tung, Appl. Phys. Lett., **75**, 853 (1999).

[5] M. Mikhail, R. Baklanov and K. Maex, Phil. Trans. R. Soc., **A 364**, 201(2006).

[6] C. Ryu, *Materials Science and Engineering*(Stanford University, Ph. D. Dissertation, 1998).

[7] K. Endo, K. Shinoda and T. Tatsumi, J. Appl. Phys., **86**, 2739 (1999).

[8] A. Grill and V. Patel, Appl. Phys. Lett., **79**, 803 (2001).

[9] Y. H. Kim, S. K. Lee and H. J. Kim, J. Vac. Sci. Technol., **A 18**, 1216 (2000).

[10] M. R. Wang, Rusli, M. B. Yu, N. Babu, C. Y. Li and K. Rakesh, Thin Solid Films, **462-463**, 219 (2004).

[11] C. Y. Kim, S. H. Kim, H. S. Kim, R. Navamathavan and C. K. Choi, J. Korean Phys. Soc., **50**, 1119 (2007).

[12] R. Navamathavan, A. S. Jung, H. S. Kim, Y. J. Jang and C. K. Choi, J. Korean Phys. Soc., **50**, 1803 (2007).

[13] T. Ohba, J. FUJITSU Sci. Tech., **38**, 17 (2002).

[14] L. Peter, Semiconductor International, **23**(6), 6108 (2000).

[15] N. P. Hacker, MRS Bullentin, **22**(10), 33 (1997).

[16] P. R. Resnick, Polymer Preprints, Division of Polymer Chemistry, American Chemical Society, **31**, 312 (1990).

[17] E. I. du Pont de Nemoues and Company, DuPont Teflon Amorphous Fluropolymer, product data sheet (2002).

[18] N. P. Hacker, MRS Bullentin, **22** (10), 33 (1997).

[19] G. Mwssner, I. Turnik, J. W. Balde, and P. Garrou, editors, *Thin Film Multichip Modules*, (A Technical Monograph of the International Society for Hybrid Microelectronics, 1992).

[20] Dow Chemical Company, Benzocyclobutene Technical data sheet, Midland, MI 48642.

[21] L. Peters, *Semiconductor International*, **21** (10), 64 (1998).

[22] N. H. Hendricks, K. S. Lau, A. R. Smith, and W. B. Wan, Materials Research Society Proceedings, **381**, 59 (1995).

[23] J. H. Golden, C. J. Hawker, and P. S. Ho, *Semiconductor International*, **24** (5), 79 (2001).

[24] P. Singer, *Semiconductor International*, **23** (5), 44 (2000).

[25] A. F. Braun, *Semiconductor International*, **23** (6), 128 (2000).

[26] C. Jin, J. D. Luttmer, D. M. Snith, and T. Ramos, MRS Bulletin, **22** (10), 39 (1997).

[27] H. S. Nalwa, editor, *Handbook of Low and high Dielectric Constant Materials and Their Applications: Materials and Processing*, (Academic Press, Inc., San Diego 1999).

[28] E. D. Birdsell and R. A. Gerhardt, in *Low Dielectric Constant Materials Ⅳ*, C. Chiang, P. S. Ho, T. M. Lu, and J. T. Wetzel, editor, Materials Research Society Symposium, Warrendale, PA, **511**, 111 (1998).

[29] S. Nitta, A. Jain, V. Pisupatti, W. Gill, P. Wayner, and J. L. Plawsky, in *Low Sielectric Constant Materials Ⅳ*, C. Chiang, P. S. Ho, T. M. Lu, and J. T. Wetzel, editor, Materials Research Society Symposium, Warrendale, PA, **511**, 99 (1998).

[30] Honeywell Advanced Microelectronic Materials, Nanoglass, product bulletin (2000).

[31] T. Ramos, K. Rhoderick, R. Roth, L. Brungardt, S. Wallace, J. Drage, J. Dunne, D. Wndisch, R. Katsanes, N. Viernes, and D. M. Smith, in *Low*

Dielectric Constant Materials IV, C. Chiang, P. S. Ho, T. M. Lu, and J. T. Wetzel, editor, Materials Research Society Symposium, Warrendale, PA, **511**, 105 (1998).

[32] C. C. Cho, D. M. Smith, and J. Anderson, Materials Chemistry and Physics, **42**, 91 (1995).

[33] C. Jin and J. Wetzel, *Proceeding of the International Interconnect Technology Conference*, San Francisco, CA, (2000).

[34] Q. Han, W. Chen, C. Waldfried, O. Escorica, N. M. Sbrokey, T. J. Bridgwater, E. S. Moyer, and I. Berry, *Proceedings of the International Interconnect Technology Conference*, IEEE Electron Devices Society, 171 (2001).

[35] A. Gill and D. A. Neumayer, J. Appl. Phys., **94**, 6697 (2003).

[36] J. P. Wang, Y. K. Su and J. F. Chen, IEEE Trans. Device Mater. Reliability, **8**, 210 (2008).

[37] I. S. Bae, S. J. Cho, W. S. Choi, H. J. Cho, B. Hong, H. D. Jeong and J. H. Boo, Prog. Org. Coat., **61**, 245 (2008).

[38] K. Maex, M. R. Baklanov, D. Shamiryan, F. Lacopi, S. H. Brongersma and Z. S. Yanovitskaya, J. Appl. Phys., **93**, 8790(2003).

[39] C. S. Yang, K. S. Oh, J. Y. Ryu, D. C. Kim, S. Y. Jing and C. K. Choi, Thin Solid Films, **390**, 113 (2001).

[40] A. Grill and V. Patel, Mater. Res. Soc. Symp. Proc., **612**, D2.9.1 (2000).

[41] D. H. Chung, *Electrical Conduction Mechanism and Equivalent Circuit Analysis in Alq_3 based Organic light Emitting Diode* (Kwangwoon University, Ph. D. Dissertation, 2004).

[42] C. H. Ting and T. E. Seidel, Mater. Res. Soc. Symp., **381**, 3 (1995).

[43] A. Grill, V. Patel, Appl. Phys. Lett., **85**, 6 (1999).

[44] L. M. Han, J. S. Pan, S. M. Chen, N. Balasubramanian, J. Shi, L. S. Wong and P. D. Foo, J. Electrochem. Soc., **148**, F148 (2001).

[45] A. Grill, D. A. Neumayer, J. Appl. Phys., **94**, 6697 (2003).

[46] P. W. Atkins, *Physical Chemistry*, 5th ed. (Oxford University Press, New

York, 1994).

[47] Y. H. Kim, "*Deposition and Characterization of Low-Dielectric-Constant SiOC Thin Fims for Interlayer Dielectrics of Multilevel Interconnection*", (Seoul National University, Ph. D. Dissertation, 2002).

[48] EH Nicollian and JR Brews, *MOS Physics and Technology* (Wiley, New York, 1982).

[49] S. M. Sze, *Physics of Semiconductor Device* (Wiley, New York, 1981).

[50] S. Kar and W. E. Dahlke, *Solid-State Electro*., **15**, 221 (1972).

[51] M. Ohring, *The Materials Science of Thin Films*(Academic Press, 1969).

[52] L. I. Maissel and I. Glang. *Handbook of Thin Film Technology*(Mcgraw-Hill Book Company, New York, 1983).

[53] M. J. Lee, *Structural and electrical properties of tantalum pentoxide for display devices* (Kyung Hee University, Ph. D. Dissertation, 2003).

[54] K. C. Kao, *Dielectric Phenomena in Solids* (Elsevier, Berlin, 2004).

[55] A. S. Jung, R. Navamathvan, K. M. Lee and C. K. Choi, Surf. Coat. Technol., **202**, 5693 (2008).

[56] V.I. Demidov, C.A. Dejoseph and A.A. Kudryavtsev, Plasma Sources Sci. Technol., **13**, 600 (2004).

[57] T. Welzel, I. Dani, F. Richter, Plasma Sources Sci. Technol., **11**, 251 (2002).

[58] C. Ye, Z. Ning, Y. Xin, T. Wang, X. Yu and M. Jiang, Microelectron. Eng., **82**, 35 (2005).

[59] P. N. Sen, M. F. Thrope, Phys. Rev. B, **15**, 4030 (1997).

[60] Y. Lin, T. Y. Tsui and J. J. Vlassak, J. Electrochem. Soc., **153**, F144 (2006).

[61] C. S. Yang, Y. H. Yu, K. M. Lee, H.J. Lee and C. K. Choi, Thin Solid Films, **435**, 165 (2003).

[62] C. Onneby, C.G. Pantano, J. Vac. Sci. Technol. A, **15**, 1597 (1997).

[63] J. Heo, H.J. Kim, J.H. Han and J.W. Shon, Thin Solid Films, **515**, 5035 (2007).

[64] H. Li, T. Xu, C. Wang, J. Chen, H. Zhou and H. Liu, Diamond Relat. Mater.,

15, 1585 (2006).

[65] A. S. Glaude, L. Thomas, E. Tomasella, J. M. Badie, R. Berjoan, Surf. Coat. Technol., **201**, 174 (2006).

[66] H. Kitoh, M. Muroyama, M. Sasaki, M. Iwasawa and H. Kimura, Jap. J. Appl. Phys., **35**, 1464 (1996).

[67] Y. Uchida, K. Taguchi, T. Nagai, S. Sugahara and M. Matsumura, Jap. J. Appl. Phy., **37**, 6396 (1998).

[68] K. S. Oh, "*A Study on the Physical Properties of Carbon-doped Silicon Oxide Low-k Thin Films with Nano-pore Structure for ULSI Interconnect Application*", (JeJu National University, Ph. D. Dissertation, 2005).

[69] C. Y. Kim, S. H. Kim, R. Navamathavan and C. K. Choi, J. Korean Phys. Soc., **50**, 1119 (2007).

[70] Hill NE, Vaughan WE, Price AH and Davies M. Sugden TM, *Dielectric Properties and Molecular Behavio*r, (Van Nostrand Reinhold, New York, 1969).

[71] Y. H. Kim, S. K. lee and H. J. Kim, J. Vac. Sci. Technol., A **18**, 1216 (2000).

[72] Y. H. Wang, M. R. Moitreyee, R. Kumar, L. Shen, K. Y. Zeng, J. W. Chai and J. S. Pan, Thin Solid Films, **460**, 211 (2004).

[73] Y. H. Wang, J. Lin and C. H. A. Chua, Mater. Sci. Eng., B **95**, 43 (2002).

[74] L. M. Han, J. Pan, S. Chen, N. Balasubramanian, J. Shi, L. S. Wong and P. D. Foo, J. Electrochem. Soc., **148**, F148 (2001).

[75] C. Radtke, I.J.R. Baumvel, J.Morais and F.C. Stedile, Appl. Phys. Lett., **78**, 3601 (2001).

[76] T.K.S. Wong, B. Liu, B. Narayanan, V. Ligatchev and R. Kumar, Thin Solid Films, **462 - 463**, 156 (2004).

[77] W. C. Oliver and G. M. Pharr, J. Mater. Res., **7**, 1564 (1992).

[78] L. Shen and K. Zeng, Microelectronic Eng., **71**, 221 (2004).

[79] C. S. Yang and C. K. Choi, Curr. Appl. Phys., **6**, 243 (2006).

[80] W.J. Zhu, T.P. Ma, S. Zafar and T. Tamagawa, IEEE Electron Device Lett., **23**,

597 (2002).

[81] K. Suzuk,M. Sakagami, E.Nishimura and K.Watanabe, IEEE Transactions on Nuclear Sci., **NS-32**, 3911 (1985).

[82] L.P. Trombeta, F.J. Feigl and R.J. Zeto, J. Appl. Phys., **69**, 2512 (1991).

[83] C. Mahata, M.K. Bera, P.K. Bose and C.K. Maiti, Thin Solid Films, **517**, 163 (2008).

[84] B.E. Deal, IEEE Trans. on Electron Devices, **ED-27**, 606 (1980).

[85] S. Zafar, A. Callegari, V. Narayanan and S. Guha, Appl. Phys. Lett., **81**, 608 (2002).

[86] M. Kimura and H. Koyama, J. Appl. Phys., **85**, 7671 (1999).

[87] Y. S. Diamand, A. Dedhia, D. Hoffstetterand and W.G. Oldham, J. Electrochem. Soc., **140**, 2427 (1993).

[88] S. K. Rha, S. Y. Lee, W. J. Lee, Y. S. Hwang, C. H. Park, D. W. Kim, Y. S. Lee and C. H. Whang, J. Vac. Sci. Technol. B, **16**, 2019 (1998).

[89] K.C. Tsai, W.F. Wu and C.G. Chao, J. Electron. Mater., **35**, 1523 (2006).

[90] A. L. S. Loke, J. T. Wetzel, J. J. Stankus, M. S. Angyal, B. K. Mowry and S. S. Wong, IEEE Electron Dev. Lett., **19**, 177 (1998).

[91] S. Rogojevic, A. Jain, F. Wang, W.N. Gill, J.L. Plawsky and T.M. Lu, J. Electrochem. Soc., **149**, F122 (2002).

[92] S. Mukaigawa, T. Aoki, Y. Shimizu and T. Kikkawa, Jpn. J. Appl. Phys., **39**, 2189 (2000).

[93] J. D. McBrayer, R. M. Swanson and T. W. Sigmon, J. Electrochem. Soc., **133**, 1242 (1986).

[94] I. Fisher and M. Eizenberg, Thin Solid Films, **516**, 4111 (2008).

[95] C. D. Wagner, D. E. Passoja, H. F. Hillery, T. G. Kinisky, H.A. Six, W. T. Jansen and J. A. Taylor, J. Vac. Sci. Technol., **21**, 933 (1982).

[96] O. R. Rodriguez, W. Cho, R. Saxena, J. L. Plawsky and W. N. Gill, J. Appl. Phys., **98**, 024108 (2005).

[97] A. L. S. Loke, J. T. Wetzel, P. H. Townsend, T. Tanabe, R. N. Vrtis, M. P.

Zussman and D. Kumar, C. Ryu, S. S. Wong, IEEE Trans. Electron Devices, **46**, 2178 (1999).

[98] K. Y. Yiang, W. J. Yoo and A. Krishnamoorthy, IEEE Trans. Electron Devices, **52**, 2333 (2005).

[99] P. T. Liu, T. C. Chang, S. T. Yan, C. H. Li and S. M. Sze, J. Electrochem. Soc., **150**, F7 (2003).

[100] F. Chen, P. S. McLaughlin and K. Chanda, Appl. Phys. Lett., **91**, 192109 (2007).

[101] Y. L. Li, Z. Tokei and K. Maex, Microelectron. Eng., **76**, 20 (2004).

[102] Z. W. He, X. Q. Liu, Q. Su and Y. Y. Wang, Appl. Phys. A, **82**, 349 (2006).

[103] R. Navamathavan, C. Y. Kim, C. K. Choi and H. J. Lee, J. Korean Phys. Soc., **55**, 1955 (2009).

[104] S. Yu, T. K. S. Wong, X. Hu and J. Wei, Microelectron. Eng., **77**, 14 (2005).

[105] Y. S. Diamand, A. Dedhia, D. Hoffstetterand and W. G. Oldham, J. Electrochem. Soc., **140**, 2427 (1993).

[106] C. C. Ho and B. S. Chiou, Microelectron. Eng., **84**, 646 (2007).

[107] S. Yu, T. K. S. Wong, X. Hu and J. Wei, Microelectron. Eng., **77**, 14 (2005).

[108] K. Y. Yiang, W. J. Yoo, Q. Guo and A. Krishnamoorthy, Appl. Phys. Lett., **83**, 524 (2003).

[109] V. V. Afanasev, M. Houssa, A. Stesmans, G. J. Adriaenssens and M. M. Heyns, J. Non-cryst. Solids, **303**, 69 (2002).

[110] I. Dokme and S. Altindal, Physica B, **393**, 328 (2007).

[111] M. M. Bulbul and S. Zeyrek, Microelectron. Eng., **83**, 2522 (2006).

[112] A. Tataroglu, Microelectron. Eng., **83**, 2551 (2006).

[113] M. M. Bulbul, Microelectron. Eng., **84**, 124 (2007).

[114] I. Yucedag, S. Altindal and A. Tataroglu, Microelectron. Eng., **84**, 180 (2007)

[115] B. Tataroglu, S. Altindal and A. Tataroglu, Microelectron. Eng., **83**, 2021 (2006).

[116] I. M. Afandiyeva, I. Dokme, S. Altindal, L. K. Abdullayeva and S. G. Askerov, Microelectron. Eng., **85**, 365 (2008).

[117] A. Tataroglu, Microelectron. Eng., **83**, 2551 (2006).

[118] E. H. Nicollian, J. R. Brews, *Metal-Oxide-Semiconductor Physics and Technology* (John Wiley & Sons, New York, 1982).

[119] K. S. K. Kwa, S. Chattopadhyay, N. D. Jankovic, S. H. Olsen, L. S. Driscoll and A. G. Oniell, Semicond. Sci. Technol., **18**, 82 (2003).

[120] V. V. Daniel, *Dielectric Relaxation* (Academic Press, London, 1967).

[121] C. P. Symth, *Dielectric Behavior and Structure* (McGraw-Hill, new York, 1955).

[122] R. Navamathavan, C. Y. Kim, C. K. Choi and H. J. Lee, J. Korean Phys. Soc., **55**, 1955 (2009).

[123] A. S. Zakirov, R. Navamathavan, S. H. Kim, Y. J. Jang, A. S. Jung and C. K. Choi, J. Korean Phys. Soc., **49**, 1293 (2006).

[124] A. Tataroglu, S. Altindal and M. M. BulBul, Microelectron. Eng., **81**, 140 (2005).

[125] C. V. Kannan, S. Ganesamoorthy, C. Subramanian and P. Ramasamy, Phys. Stat. Sol., A **196**, 465 (2003).

[126] Z. Jiwei, Y. Xi, W. Mingzhong and Z. Liangying, J. Phys., D **34**, 1413 (2001).

[127] B. Tataroglu, S. Altindal and A. Tataroglu, Microelectron. Eng., **83**, 2021 (2006).

[128] I. Yucedag, S. Altindal and A. Tataroglu, Microelectron. Eng., **84**, 180 (2007).

국문초록

본 연구에서는 PECVD 방법으로 nano-pore 구조를 갖는 SiOC(-H) 박막을 형성하여 flow rate ratio, rf power 그리고 기판온도에 따른 SiOC(-H) 박막의 결합구조를 조사하였고, 또한 Al/SiOC(-H)/*p*-Si(100)와 Cu/SiOC-H)/*p*-Si(100) 구조에 대한 전기적 특성을 규명하여 향후 32 nm급 Cu/Low-*k* chip 개발에 따른 기초적 물성에 대한 연구를 제시하였다. 그리고 박막형성에 사용될 PECVD 장비에 대한 플라즈마 특성에 대한 진단으로부터 공정조건을 수립하였다. 본 연구 수행에 있어서, 저 유전상수를 갖는 물질로 Dimethyl-dimethoxy-silane (DMDMS, $C_4H_{12}O_2Si$) 전구체와 O_2 가스를 사용하였고, 본 논문의 연구결과로써 다음과 같은 SiOC(-H) 박막의 구조적 특성과 MIS 구조에 대한 전하의 수송현상을 규명하였다.

플라즈마의 최적 조건을 찾기 위해, 전자 밀도 (Te), 전자온도 (Te) 및 각종 활성종들의 거동을 조사하였다. rf 파워가 100 W에서 800 W로 증가할수록 전자밀도 6.23×10^{8} 에서 1.22×10^{10} cm^{-3} 그리고 및 전자온도는 1.57 to 2.03 eV로 각각 증가하였다. 또한 전구체의 완전한 해리는 500 W이상에서 일어났다.

형성된 SiOC(-H) 박막의 결합구조는 FTIR를 이용하여 wave number가 400에서 4000 cm^{-1}인 영역에서 Si - O - Si (around 1055 cm^{-1}), Si - O - C (around 1105 cm^{-1}), Si - CH_3 (around 950 and 1250 cm^{-1}) 그리고 - OH (3200 - 3700 cm^{-1})와 같은 다양한 결합모드를 조사하였다. 여기서 Si - O - Si asymmetric mode는 Si-O-S network link, Si-O-C ring link, Si-O-C open link, Si-O-C cage link 구조로 이루어져 있음을 조사되었다. 이러한 구조는 박막 내에 함유된 -CH_3 groups이 Si-O와 결합하여 SiO_2 network 구조를 보다 덜 치밀한 형태의 Si-O-C 구조로 만들고, 이러한 결과로 Si-O-Si asymmetric mode는 낮은 wave number로 이동하는 것을 보였다 (red shift). 그러나 기판온도 300 °C 이상에서 증착된 SiOC(-H) 박막은 낮은 탄소함량을 갖는다. 이는 높은 기판온도에 의해 Si-CH_3 결합은 깨지고, 상대적으로 Si-O 결합이 증가하여 유전상수는 증가한다. 또한 XPS 스펙트럼에서의 Si 2p peak는 탄소원자의 농도 증가로 인해 낮은 binding energy로 이동하여 SiOC(-H)

박막이 형성됨을 알 수 있다. 이는 곧 SiOC(-H) 박막내의 Si-O bond와 Si-C bond 상호간의 반발력에 의해 O-Si-C 사이의 결합각을 증가함을 의미하며, 유전상수를 감소시키는 주요한 원인으로 규명되었다.

Cu(Al)/SiOC(-H)/*p*-Si(100)/Al MIS 구조에서의 계면특성을 조사하기 위해 전기적 바이어스 스트레스를 전극에 공급하였다. 먼저 전극이 Al 인 경우, 열처리 전 박막의 flat-band voltage는 바이어스 스트레스 전보다 양의 방향으로 약 11 V 이동하였으며, 열처리 온도가 450 °C일 때 약 26 V의 flat-band voltage의 이동을 보였다. 전극이 Cu인 경우, 열처리 전 박막의 flat-band voltage는 바이어스 스트레스 전보다 양의 방향으로 약 18 V 이동하였으며, 열처리 온도가 450 °C일 때 약 32 V의 flat-band voltage의 이동을 보였다. 결과적으로, 전기적 스트레스 후의 flat-band voltage는 금속의 종류와 상관없이 양의 방향으로 이동하였고, 계면전하밀도는 전기적 스트레스를 가하는 동안, SiOC(-H) 박막의 열처리 온도가 증가할수록 증가됨을 조사하였다. 이와 같은 전기적 스트레스는 계면에 존재하는 hydrogen과 관련된 Si-H, Si-OH 결합이 파괴되면서 silicon dangling bond를 형성하여 계면전하를 증가시키게 됨을 보여 계면 생성은 SiOC(-H)/*p*-Si(100) 계면 및 SiOC(-H) 박막내의 hydrogen과 관련된 결합에 밀접한 관계가 있음을 규명하였다. 반면에 계면상태밀도 분포는 전극 금속 종류에 있어 다소 차이점을 보이지만, stress 시간에 따른 계면상태밀도의 변화는 거의 미미한 수준이다. 전극 금속 Cu 인 경우 Al 보다 많은 전하를 Si 계면에 축적한다. 이는 SiOC(-H)박막 내 전하의 유동성으로 볼 때, 전극 Al 보다 Cu에서 유동성을 증가시키며 쉽게 반응을 일으킬 수 있기 때문이다. 반면에 전극 금속 종류에 따른 포획전하 차이는 전극금속과 SiOC(-H)박막 계면 사이 즉 일함수차이에 의한 포획전하의 차이로 볼 수 있다. 그리고 계속적인 전자주입으로 인해 포획전하의 mid-gap은 점차적으로 Si 기판으로 이동된다.

Cu/SiOC(- H)/*p*-Si(100)/Al MIS 구조에서 전극에 BTS (bias temperature stress)를 시간에 따라 공급한 후, SiOC(-H) 박막내로의 Cu 원자 확산을 조사하였다. SiOC(-H) 박막내로의 Cu 원자의 확산은 C-V 곡선을 통한 flat-band voltage의 이동으로 관찰되었다. 기판온도가 175 °C에서 225 °C로 증가하는 경우 flat-band voltage는 작은 변화를 보이지만, 225 °C에서 275 °C로 증가할 때 flat-band

voltage 변화는 다소 증가하였다. 이것은 BTS 온도와 스트레스 시간이 증가할수록 SiOC(-H) 박막내로의 Cu 원자의 이동이 증가됨을 뜻한다. BTS 조건하에서 활성화 에너지는 열처리 온도가 250 °C, 350 °C, 450 °C일 때 각각 0.58 eV, 0.26 eV, 0.22 eV로, 열처리 온도가 증가할수록 활성화 에너지는 감소하는 경향을 보였다. 또한 SiOC(-H) 박막은 기존의 SiO_2 박막에 비해 외부 스트레스에 의한 저항이 크게 나타났다. 이것은 외부에서 인가된 열, 전계 등의 스트레스에 의한 물질 특성의 변화가 적다는 것을 의미한다. 기판을 가열하면 격자 진동에 의해 유동 전하의 이동에 대한 에너지 장벽이 낮아지고, 이로 인해 전압을 가했을 시 이온의 이동이 원활해진다. 물론 Cu 원자의 확산된 양은 Si와 O에 비해서 매우 작기 때문에 상대적인 원소의 비율을 보여주는 AES 분석의 특성상 금속이온의 양은 매우 적게 나타나고 있지만, BTS 후의 Cu/SiOC(-H) 계면을 HR-TEM을 이용하여 관찰하였을 경우 SiOC(-H) 박막이 전기적으로 불안정해지는 원인이 금속 이온의 확산에 의한 것임을 확인하였다. SiOC(-H) 박막의 누설전류 측정인 경우, 열처리 전 시료의 기판온도가 200 °C 일 때, 초기 전계 인가 시 절연파괴가 발생하였다. 그러나 열처리 온도가 450 °C인 경우, 3.7 MV/cm의 높은 전계를 인가한 경우에도 SiOC(-H) 박막이 절연파괴는 없었다. 열처리 전 시료의 경우, 2 MV/cm 전계(상온)에서 측정된 누설 전류는 1×10^{-9} A/cm^2 이며, 열처리된 시료의 경우, 전계 2 MV/cm(상온)에서 5×10^{-7} A/cm^{2}의 평균 누설 전류를 보였다. 이러한 결과로 볼 때, Cu 원자는 높은 온도에서의 높은 확산도로 인해 SiOC(-H) 박막내로 더 많은 Cu 원자가 확산되는 결과를 초래하였다. 그리고 온도 증가에 따른 들뜬 전자들의 열 여기로 인해 측정 온도에 따른 누설전류는 증가됨을 보였다. 열처리 된 SiOC(-H) 박막은 박막내부의 Si-CH_3, Si-H, Si-OH 그리고 -Si(CH_3)$_3$ 결합들이 높은 열처리로 인해 파괴되어 계면 특성에 영향을 주었으며, 이는 좀 더 많은 양의 Cu 원자의 확산을 유발시켜 누설전류를 증가시켰다.

SiOC(-H) 박막의 전기전도 과정에서의 Schottky barrier height의 값은 열처리 온도가 증가할수록 감소하였다. 그리고 열처리 전 시료의 경우 Poole-Frenkel trap height (0.365 eV)은 Schottky barrier height (0.325 eV)보다 조금 높게 계산되었다. 여기서 열처리된 시료는 Poole-Frenkel 형태를 취하지 않았으므로 계산되어질 수 없었다. 500 °C로 열처리된 SiOC(-H) 박막은 모든 측정온도에서 절연파괴가 일어

났으며, 절연파괴전계는 측정온도 증가와 함께 감소하였다. 이러한 결과 또한 앞에서 설명되어진 바와 같이 SiOC(-H) 박막내로의 Cu 원자의 확산에서 원인을 찾을 수 있다. 즉 인가된 전계에 의한 이온화 또는 Cu 원자의 이동으로 SiOC(-H) 박막 내의 O^- 이온과 결합하여 CuO, Cu_2O를 형성하며, 이는 누설전류 및 전도현상에 악영향을 준다.

상온에서의 주파수변화에 따른 정전용량에 대한 값들은 직렬 저항, 표면상태 밀도 그리고 인가된 DC 전압 하에서 보충된 AC 신호의 주파수에 의존함을 조사하였다. 저 주파수에서의 정전용량의 증가는 계면 전하에 의한 과잉 정전용량 때문이며, C-V 및 G/ω-V 곡선에서 관찰된 주파수 분산은 공급되는 전압과 계면 전하가 원인임을 알 수 있었다. 그리고 주파수가 증가함에 따라 유전상수는 감소하는 경향을 보였다. 이것은 유전상수에 기여하는 한 요소로써 계면 분극인 경우 높은 주파수로 인해 교류장 내에서의 신호를 따라갈 수 없어 결과적으로 유전상수는 감소함을 뜻한다. 또한 주파수 증가에 따른 유전손실의 증가는 전기적 특성에 좋지 않은 영향을 주는 SiOC(-H)/*p*-Si(100) 계면의 트랩전하 증가가 원인인 것으로 밝혀졌다.

이와 같은 결과로부터 [DMDMS/(DMDMS+O_2)] flow rate ratio가 약 80%, rf power가 700 W, 기판온도가 상온인 경우에 가장 양질의 박막을 형성할 수가 있었으며, Al/SiOC(-H)/*p*-Si(100)와 Cu/SiOC-H)/*p*-Si(100) 구조에서 누설전류, 전하수송 모드, Cu 원자 migration 현상 등의 결과부터 계면에 대한 전하의 운동기작이 규명됨으로써 32 nm 급 Cu/Low-k chip 개발에 중요한 기초적 자료로 활용될 수 있음을 보였다.

List of related publications

1. Publications

- International Papers

1) **Chang Young Kim**, Heang Seuk Lee, Jong-Kwan Woo, Chi Kyu Choi, R. Navamathavan, Kwang-Man Lee, Myung Taek Hyun, Frequency-dependent Capacitance-Voltage and Conductance-Voltage Characteristics of Low-dielectric-constant SiOC(-H) Thin Films Deposited by Using Plasma-enhanced Chemical Vapor Deposition, Journal of the Korean Physics Society 57(6), 1976 (2010).
2) **Chang Young Kim**, Heang Seuk Lee, R. Navamathavan, Jong-Kwan Woo, Chi Kyu Choi, Effect of evaporated copper and aluminum on post-annealed SiOC(–H) films deposited using plasma-enhanced chemical vapor deposition, Thin Solid Films, 518, 6469 (2010).
3) Chi Kyu Choi, Heang Seuk Lee, R. Navamathavan, Jong-Kwan Woo, **Chang Young Kim**, Study of Cu diffusion behavior in low dielectric constant SiOC(–H) films deposited by plasma-enhanced chemical vapor deposition, Thin Solid Films, 518, 6474 (2010).
4) R. Navamathavan, Cheul Ro Lee, R. Nirmala, **Chang Young Kim** and Chi Kyu Choi, Preparation and Properties of Low-dielectric-constant SiOC(-H) Thin Films Deposited by Using PECVD, Journal of the Korean Physics Society 56(3), 818 (2010).
5) Heang Seuk Lee, **Chang Young Kim**, Jong-Kwan Woo, Chi Kyu Choi, R. Navamathavan, Kwang-Man Lee, Electrical Conduction in Low-dielectric-constant SiOC(-H) Films with Nano-pore Structures Deposited by Using Plasma-enhanced Chemical Vapor Deposition with Dimethyldimethoxysilane/O_2 Precursors, Journal

of the Korean Physics Society 56(5), 1478 (2010).

6) R. Navamathavan, **Chang Young Kim**, Heang Seuk Lee, Jong-Kwan Woo, Younghun Yu and Chi Kyu Choi, Heon Ju Lee, Investigation of Electrical Conduction in Low-dielectric-constant SiOC(-H) Thin Films Deposited by Using PECVD, Journal of the Korean Physics Society 55(1), 227 (2009).

7) Heang Seuk Lee, **Chang Young Kim**, R. Navamathavan, Jong-Kwan Woo, Younghun Yu and Chi Kyu Choi, Morphological and Compositional Changes at the SiOC(-H)/*p*-Si(100) Interface Region Prepared by Using PECVD, Journal of the Korean Physics Society 55(3), 1087 (2009).

8) Kwang-Man Lee, **Chang Young Kim** and Chi Kyu Choi, Sang-Won Yun, Jong-Bong Ha and Jung-Hee Lee, Jeong Yong Lee, Interface Properties of Nickel-silicide Films Deposited by Using Plasma-assisted Atomic Layer Deposition, Journal of the Korean Physics Society 55(3), 1153 (2009).

9) R. Navamathavan, **Chang Young Kim**, and Chi Kyu Choi, Heon Ju Lee, Interface Characterization and Current Conduction in Low-Dielectric-Constant SiOC(-H) Films with a MIS Structure, Journal of the Korean Physics Society 55(5), 1955 (2009).

10) **Chang Young Kim**, R. Navamathavan, Heang Seuk Lee, Younghun Yu, Jong-Kwan Woo and Chi Kyu Choi, A Study of the Properties of the Cu/SiOC(-H)/*p*-Si(100) and Cu/TaN/SiOC(-H)/*p*-Si(100) Interface, Journal of the Korean Physics Society, 55(5), 1960 (2009).

11) **Chang Young Kim**, An Soo Jung, R. Navamathavan, Chi Kyu Choi, Kwang Man Lee, Structural and Electrical Characterizations of Low-Dielectric-Constant SiOC(-H) Thin Films Deposited by Using Plasma-Enhanced Chemical Vapor Deposition for ULSI Interconnects, Journal of the Korean Physics Society 53(1), 371 (2008).

12) An Soo Jung, **Chang Young Kim**, R. Navamathavan, Chi Kyu Choi, Mechanical Properties of Low-Dielectric SiOC(-H) Thin Films with Different Substrate Temperatures Deposited by Using PECVD, Journal of the Korean Physics Society

53(1), 361 (2008).

13) R. Navamathavan, **Chang Young Kim**, An Soo Jung, Chi Kyu Choi, Heon Ju Lee, Deposition and Characterization of Porous Low-Dielectric-Constant SiOC(-H) SiOC(-H) Thin Films Deposited from TES/O_2 precursors by Using Plasma-Enhanced Chemical Vapor Deposition, Journal of the Korean Physics Society 53(1), 351 (2008).

14) **Chang Young Kim**, R. Navamathavan, Heon Ju Lee, Chi Kyu Choi, Electrical Characterization of Low-k Films with nano-pore structure prepared with DMDMOS/O_2 precursors, Surface & Coating Technology 202, 5688(2008).

15) R. Navamathavan, An Soo Jung, **Chang Young Kim**, Chi Kyu Choi, Plasma Diagnostics during Plasma-Enhanced-Dielectric-Constant SiOC(-H) Films from TES/O_2 Precursors, Journal of the Korean Physics Society 53(3), 1468 (2007).

16) **Chang Young Kim**, An Soo Jung, R. Navamathavan and Chi Kyu Choi, Bonding Configuration and Electrical Properties of Carbon-Incorporated Loe-Dielectric-Constant SiOC(-H) Films with Nano-Pore Structure Deposited by Using PECVD, Journal of the Korean Physics Society 53(5), 2621 (2008).

17) An Soo Jung, **Chang Young Kim**, R. Navamathavan and Chi Kyu Choi, Jong-Kwan Woo, Kwang-Man Lee, Nano-Mechanical Analyses of Low-Dielectric-Constant SiOC(-H) Thin Films Deposited by Using Plasma-Enhanced Chemical-Vapor Deposition, Journal of the Korean Physics Society 53(5), 2512(2008).

18) **Chang Young Kim**, Yong Jun Jang, R. Navamathavan and Chi Kyu Choi, A Study of the Electrical Properties at the Interface in MIS Structure with Low-Dielectric-Constant SiOC(-H) Films Deposited by Using UV-Source-Assisted PECVD, Journal of the Korean Physics Society 50(4), 1125 (2007).

19) **Chang Young Kim**, Seung Hyun Kim, Hyub Seung Kim, R. Navamathavan and Chi Kyu Choi, Formation Mechanism and Structural Characteristics of Low-Dielectric-Constant SiOC(-H) Films Deposited by Using Plasma-Enhanced Chemical-Vapor Deposition with DMDMS and O_2 Precursors, Journal of the

Korean Physics Society 50(4), 1119 (2007).

20) **Chang Young Kim**, Seung Hyung Kim, R. Navamathavan, Chi Kyu Choi, Won Young Jeung, Characteristics of low-k SiOC(-H) films deposited at various substrate temperature by PECVD Using DMDMS/O_2 Precursor, Thin Solid Films 516, 340 (2007).

21) **C. Y. Kim**, H. J. Ko, D. S. Kim and C. K. Choi, Effect of Annealing on the Bonding Structure and Dielectric Properties of a-C: F Thin Films, Journal of Surface Analysis 12(2), 218 (2005).

- Domestic Paper

1) Hyeon-Jin Shin, Hyun-Dam Jeong, Jong-Beak Seon, Jong-Min Kim, Chang Sil Yang, **Chang Young Kim** and Chi Kyu Choi, High-Performance, Low Dielectric Constant Thin Film from a Dual Organo Siloxane Precursor, SAMSUNG Journal of Innovative Technology 1(1), 231 (2005).

2. Conference Activities

- International Presentation

1) Anvar Zakirov, Rangaswamy Navamathavan, Tae Won Kang, **Chang Young Kim**, Chi Kyu Choi, Capacitance-voltage characterization of the defect states and charge transport properites of low-*k* SiOC(-H) dielectric films deposited by UV-assisted PECVD, The 10th Asia pacifac Conference on Plasma Science and Technology and the 23rd Symposium on Plasma Science for Material, Japan Society for the Promotion of Science, Lotte Hotel Jeju, Korea, (2010).

2) **Chang young Kim**, Heang Seuk Lee, Jong-Kwan Woo, Hean Ju Lee, Chi Kyu Choi, Won Young Kim, UV curing effects on the bonding structure and electrical properties of low-k SiOC(-H) films for 45 nm technology node, The 10th Asia

pacifac Conference on Plasma Science and Technology and the 23rd Symposium on Plasma Science for Material, Japan Society for the Promotion of Science, Lotte Hotel Jeju, Korea, (2010).

3) Chi Kyu Choi, **Chang Young Kim**, Heang Seuk Lee, Jong-Kwan Woo, Kwang man Lee, Won Young Jeung, Leakage current and dielectric breakdown properties of low dielectric constant SiOC(-H) films using comb capacitor structure, The 10th Asia pacifac Conference on Plasma Science and Technology and the 23rd Symposium on Plasma Science for Material, Japan Society for the Promotion of Science, Lotte Hotel Jeju, Korea, (2010).

4) **Chang Young Kim**, H. S. Lee, J.-K. Woo, Chi Kyu Choi, DC Electric Field Induced Second Harmonic Generation Studies of Low Dielectric Constant SiOC(-H) Films, The 36th International Conference on Metallugical Coating and Thin Films, American Vacuum Society, Town and Country Hotel, San Diego California, USA, (2010).

5) **Chang Young Kim**, Heang Seuk Lee, Jong-Kwan Woo, Chi Kyu Choi, Improvement of the SiOC(-H)/*p*-Si(100) interface properties by Ar plasma trearment and post-annealing of SiOC(-H) Films, The 2nd International Conference on Microelectronics and Plasma Technology, The Korean Vacuum Society, BEXCO Convention Center, Busan, Korea, (2009).

6) Chi Kyu Choi, Heang Seuk Lee, Jong-Kwan Woo, **Chang Young Kim**, Study of Al and Cu diffusion behavior in low dielectric constant SiOC(-H) films deposited by plasma enhanced chemical vapor deposition, The 2nd International Conference on Microelectronics and Plasma Technology, The Korean Vacuum Society, BEXCO Convention Center, Busan, Korea, (2009).

7) Heang Seuk Lee, **Chang Young Kim**, Jong-Kwan Woo, Chi Kyu Choi, Electrical conduction in low dielectric constant SiOC(-H) films with nano-pore structure using DMDMS/O_2 precursors deposited by plasma enhanced chemical vapor deposition, The 2nd International Conference on Microelectronics and Plasma Technology", The Korean Vacuum Society, BEXCO Convention Center, Busan,

Korea, (2009).

8) **Chang Young Kim**, Jong-Bong Ha, Jung-Hee Lee, Chi Kyu Choi, Kwang-Man Lee, Interface Properties of Nikel Silicide Films Deposited by ALD with Surfactant Assistant, The 2nd International Conference on Microelectronics and Plasma Technology, The Korean Vacuum Society, BEXCO Convention Center, Busan, Korea, (2009).

9) Heang Seuk Lee, R. Navamathavan, **Chang Young Kim**, Jong-Kwan Woo, Kwang-Man Lee, Chi Kyu Choi, Reliability challenges of low-dielectric constant SiOC(-H) thin films in integrated circuit technologies, The 6th International Conference on Advanced Materials and Devices, The Korean Physical Society , Ramada Plaza Jeju Hotel, Korea, (2009).

10) **Chang Young Kim**, R. Navamathavan, Heang Seuk Lee, Jong-Kwan Woo, Kwang-Man Lee, Chi Kyu Choi, Frequency dependent C-V and G/ω-V characteristics of low-dielectric constant SiOC(-H) thin films deposited by using PECVD, The 6th International Conference on Advanced Materials and Devices, The Korean Physical Society , Ramada Plaza Jeju Hotel, Korea, (2009).

11) **Chang Young Kim**, R. Navamathavan, Heang Seuk Kim, Chi Kyu Choi, Reliability challenges for low dielectric constant SiOC(-H) thin films in integrated circuit technologies, The 14th International Symposium on the Physics of Semiconductors and Applications-2008(ISPSA-2008), The Korean Physical Society, Ramada Plaza Jeju Hotel, Jeju, Korea, (2008).

12) **Chang Young Kim**, Sang-Won Yun, Jong-Bong Ha, Jung-Hee Lee, Chi Kyu Choi, Kwang-Man Lee, Interface Properties of Nickel Silicide Film deposited by Plasma Assisted Atomic Layer Deposition (PAALD), The 14th International Symposium on the Physics of Semiconductors and Applications-2008(ISPSA-2008), The Korean Physical Society, Ramada Plaza Jeju Hotel, Jeju, Korea, (2008).

13) Heang Seuk Lee, R. Navamathavan, **Chang Young Kim**, Kwang Man Lee, Chi Kyu Choi, Morphological and compositional changes at the SiOC(-H)/*p*-Si(100) interface region prepared by using PECVD, The 14th International Symposium on

the Physics of Semiconductors and Applications-2008(ISPSA-2008), The Korean Physical Society, Ramada Plaza Jeju Hotel, Jeju, Korea, (2008).

14) R. Navamathavan, **Chang Young Kim**, Heang Seuk Lee, Chi Kyu Choi, Investigation of electrical conduction in low dielectric constant SiOC(-H) thin films deposited by PECVD, The 14th International Symposium on the Physics of Semiconductors and Applications-2008(ISPSA-2008), The Korean Physical Society, Ramada Plaza Jeju Hotel, Jeju, Korea, (2008).

15) **Chang Young Kim**, Sang-Won Yun, Jong-Bong Ha, Jung-Hee Lee, Chi Kyu Choi, Kwang-Man Lee, Formation Mechanism of Nikel Silicide Films with Low Resistivity Deposited by Atomic Layer Deposition, The 1st International Conference on Microelectronics and Plasma Technology, The Korean Vacuum Society, Ramada Plaza Jeju Hotel, Jeju, Korea, (2008).

16) **Chang Young Kim**, Heang Seuk Lee, R. Navamathavan, Young Hun Yu, Kwang Man Lee, Chi Kyu Choi, Characterization of Multiple SiOC(-H)/*p*-Si(100) interfaces in Metal-Insulator-Semiconductor Structure via Second Harmonic Generation, The 1st International Conference on Microelectronics and Plasma Technology, The Korean Vacuum Society, Ramada Plaza Jeju Hotel, Jeju, Korea, (2008).

17) **Chang Young Kim**, Hyung Cho, R. Navamathavan, Chi Kyu Choi, Young Hun Yu, The Study on Copper Ion Drift in Cu/SiOC(-H)/*p*-Si(100) Interface by Transient Photocurrent Spectroscopy, The 1st International Conference on Microelectronics and Plasma Technology", The Korean Vacuum Society, Ramada Plaza Jeju Hotel, Jeju, Korea, (2008).

18) **Chang Young Kim**, Seung Hyun Kim, R. Navamathavan, Chi Kyu Choi, Won Young Jeung, Characteristics of low-*k* SiOC(-H) films deposited at various substrate temperature by PECVD Using DMDMS/O_2 Precursor, The International Conference on Metallugical Coating and Thin Films, American Vacuum Society, Town and Country Hotel, San Diego California, USA, (2007).

19) R. Navamathavan, **Chang Young Kim**, Yong Jun Jang, An Soo Jung, Heon Ju

Lee, Chi Kyu Choi, Deposition and characterization of porous low dielectric constant SiOC(-H) thin films from TES/O_2 precursors by using plasma enhanced chemical vapor deposition, The 13th International Conference on II-VI Compound, The Materials Research Society of Korea., Jeju Shilla Hotel, Jeju, Korea, (2007).

20) An Soo Jung, **Chang Young Kim**, Yong Jun Jang, Kwang Man Lee, R. Navamathavan, Chi Kyu Choi, A Study on the interface properties of low dielectric constant SiOC(-H) thin filmswith MIS structure deposited by using PECVD, The 13th International Conference on II-VI Compound, The Materials Research Society of Korea., Jeju Shilla Hotel, Jeju, Korea, (2007).

21) Yong Jun Jang, **Chang Young Kim**, An Soo Jung, R. Navamathavan, Chi Kyu Choi, GISAXS studies of low dielectric constant SiOC(-H) thin films with nano-pore structure deposited by using PECVD, The 13th International Conference on II-VI Compound, The Materials Research Society of Korea., Jeju Shilla Hotel, Jeju, Korea, (2007).

22) **Chang Young Kim**, R. Navamathavan, Heon Ju Lee, Chi Kyu Choi, Electrical Characterization of Low-*k* Films with Nano-pore Structure Prepared with HMDSO/O_2 Precursors, Sixth Asian-European International Conference on Plasma Surface Engineering (AEPSE2007), Asian Joint Committee on Plasama Surface Engineering and European Joint Committee on Plasma and Ion Surface Engineering. Umi No Mieru Hotel, Nagasaki, Japan, (2007).

23) R. Navamathavan1, An Soo Jung, **Chang Young Kim**, Heon Ju Lee and Chi Kyu Choi, Plasma diagnostics during plasma enhanced chemical vapor deposition of low dielectric constant SiOC(-H) films from TES/O_2 precursors, The 5th International Conference on Advanced Materials and Devices, (ICAMD 2007), The Korea Physical Society, Ramada Plaza Jeju Hotel, Korea, (2007).

24) An Soo Jung, **Chang Young Kim**, R. Navamathavan, Kwang Man Lee and Chi Kyu Choi, Nano-mechanical analyses of low dielectric constant SiOC(-H) thin films deposited by using plasma enhanced chemical vapor deposition, The 5th International Conference on Advanced Materials and Devices, (ICAMD 2007), The

Korea Physical Society, Ramada Plaza Jeju Hotel, Korea, (2007).

25) **Chang Young Kim**, An Soo Jung, R. Navamathavan and Chi Kyu Choi, Bonding configuration and electrical properties of carbon incorporated low dielectric constant SiOC(-H) films with nano-pore structure deposited by using PECVD, The 5th International Conference on Advanced Materials and Devices, (ICAMD 2007), The Korea Physical Society, Ramada Plaza Jeju Hotel, Korea, (2007).

- Domestic Presentation

1) **Chang Young Kim**, Heang Seuk Lee, Jong-Kwan Woo, and Chi Kyu Choi, Interface properties of low dielectric constant SiOC(-H) films deposited by plasma enhanced chemical vapor deposition, 제37회 한국진공학회 하계정기학술대회, 한국진공학회, 디오션 리조트(여구), 여수, (2009).

2) Heang Seuk Lee, **Chang Young Kim**, Jong-Kwan Woo, and Chi Kyu Choi, Leakage current and electrical breakdown in plasma enhanced chemical vapor deposited low dielectric constant SiOC(-H) films, 제37회 한국진공학회 하계정기학술대회, 한국진공학회, 디오션 리조트(여구), 여수, (2009).

3) Chi Kyu Choi, Heang Seuk Lee, Jong-Kwan Woo, and **Chang Young Kim** , Cu diffusion behavior in SiOC(-H) films with annealed Cu/SiOC(-H)/*p*-Si(100)/Al metal-insulator-semiconductor (MIS) structure, 제37회 한국진공학회 하계정기학술대회, 한국진공학회, 디오션 리조트(여구), 여수, (2009).

4) R. Navamathavan, **Chang Young Kim**, An Soo Jung, Heon Ju Lee and Chi Kyu Choi, Evalution of ultra low dielectric constant SiOC(-H) thin films for advanced interconnects, 제34회 한국진공학회 동계정기학술대회, 한국진공학회, 단국대학교, 서울, (2008).

5) **Chang Young Kim**, An Soo Jung, R. Navamathavan, Chi Kyu Choi, Structural and electric properties of low dielectric constant SiOC(-H) films deposited by using PECVD from DMDMS/O_2 precursors, 제34회 한국진공학회 동계정기학술대회, 한국진공학회, 단국대학교, 서울, (2008).

6) An Soo Jung, **Chang Young Kim**, R. Navamathavan, Chi Kyu Choi, "Plasma parameters of the low dielectric constant SiOC(-H) thin films during the PECVD process, 제34회 한국진공학회 동계정기학술대회, The Korean Vacuum Society, 단국대학교, 서울, (2008).

7) **Chang Young Kim**, R. Navamathavan, Heang Seuk Lee, Young Hun Yu, Chi Kyu Choi, Electric field induced second harmonic generation in SiOC(-H) thin films, 제35회 한국진공학회 하계정기학술대회, The Korean Vacuum Society, Ramada Plaza Jeju Hotel, Jeju, (2008).

8) R. Navamathavan, **Chang Young Kim**, Heang Seuk Lee, Heon Ju Lee, Chi Kyu Choi, Interface characterization and current conduction in low-k SiOC(-H) thin films, 제35회 한국진공학회 하계정기학술대회, The Korean Vacuum Society, Ramada Plaza Jeju Hotel, Jeju, (2008).

9) **Chang Young Kim**, R. Navamathavan, Heang Seuk Lee, Chi Kyu Choi, Electrical properties of Cu/Tan/SiOC(-H)/*p*-Si(100) low-*k* dielectric stack, 제35회 한국진공학회 하계정기학술대회, The Korean Vacuum Society, Ramada Plaza Jeju Hotel, Jeju, (2008).

10) **Chang Young Kim**, Sang-Won Yun, Jung Hee, Chi Kyu Choi, Kwang-Man Lee, Silicdation Properties of Atomic Layer Deposited Nicel Film using by Rapid Thermal Process,제35회 한국진공학회 하계정기학술대회, The Korean Vacuum Society, Ramada Plaza Jeju Hotel, Jeju, (2008).

11) Heang Seuk Lee, R. Navamathavan, **Chang Young Kim**, Kwang-Man lee, Chi Kyu Choi, Low-k thin film interface studies by using second harmonic generation, 제35회 한국진공학회 하계정기학술대회, The Korean Vacuum Society, Ramada Plaza Jeju Hotel, Jeju, (2008).

12) **Chang Yong Kim**, Hyun Seung Kim, R. Navamathavan and Chi Kyu Choi, The formation mechanism and the structural characteristics of the low dielectric constant SiOC(-H) films deposited by using plasma enhanced chemical vapor deposition with DMDMS and O_2 precursors, The 14th Korean Conference on Semiconductor, 한국재료학회, 롯데호텔, 제주, (2007).

13) **Chang Yong Kim**, Yong Jun Jang, R. Navamathavan, and Chi Kyu Choi, A study on the surface charge density on the interface in MIS structure with low dielectric constant SiOC(-H) films deposited by using UV-source assisted PECVD, The 14th Korean Conference on Semiconductor, 한국재료학회, 롯데호텔, 제주, (2007).

감사의 글

아무것도 몰랐던 저에게 자상하시면서도 세심한 지도로 이끌어 주시고, 어려울 때 인간적으로 아낌없는 조언과 격려를 해주신 최치규 지도 교수님께 진심으로 깊은 감사를 드립니다. 그리고 바쁘신 와중에도 소중한 시간을 내셔서 제 학위 논문에 대해 세심한 검토와 조언을 해주신 고정대 교수님, 김형준 교수님, 염근영 교수님 그리고 장홍영 교수님께 깊은 감사드립니다. 또한, 마주치실 때 마다 항상 웃는 얼굴로 격려와 응원을 아끼지 않으셨던 현남규 교수님, 김두철 교수님, 김용주 교수님, 유영훈 교수님, 우종관 교수님께도 감사의 말씀을 전합니다. 그리고 박사과정 연구 활동 기간 동안 많은 도움을 준 Rangaswamy Navamathavan에게도 각별히 감사를 드립니다.

본 학위논문을 완성할 수 있도록 저를 일운과학기술재단 장학생으로 선발해주신 (주)주성엔지니어링의 황철주 대표이사님과 재단 이사진들께도 감사의 말씀을 드립니다. 또한 본 논문은 교육과학기술부 기초과학연구사업의 연구 과제 수행 참여에 의한 결과의 일부분으로서, 연구 지원에 감사드립니다.

마지막으로 부족한 것 많은 막내아들이지만 항상 믿어 주시고 든든한 후원자가 되어주신 고생 많으신 아버지, 어머니 그리고 가족들 모두에게 머리 숙여 감사드립니다.

이렇게 많은 분들이 베풀어 주신 커다란 가르침이 헛되지 않게 항상 기억하며 조금이나마 보답하면서 살아갈 것을 약속드립니다.

2010년 12월

김 창 영 드림.